

**BIOMECHANICS OF THE LOWER CERVICAL SPINE DURING  
SHEAR LOADING**

by

Jennifer Dowling-Medley

BEng, University of Guelph, 2015

A THESIS SUBMITTED IN PARTIAL FULFILLMENT OF THE  
REQUIREMENTS FOR THE DEGREE OF

MASTER OF APPLIED SCIENCE

in

The Faculty of Graduate and Postdoctoral Studies

(Biomedical Engineering)

THE UNIVERSITY OF BRITISH COLUMBIA  
(Vancouver)

May 2018

© Jennifer Dowling-Medley, 2018

The following individuals certify that they have read, and recommend to the Faculty of Graduate and Postdoctoral Studies for acceptance, the thesis entitled:

Biomechanics of the lower cervical spine during shear loading

submitted by Jennifer Dowling-Medley in partial fulfillment of the requirements for  
the degree of Master of Applied Science  
in Biomedical Engineering

**Examining Committee:**

Thomas Oxland, Orthopaedics, Mechanical Engineering

Co-Supervisor

Peter Crompton, Mechanical Engineering

Co-Supervisor

David Wilson, Orthopaedics, Mechanical Engineering

Supervisory Committee Member

Gary Schajer, Mechanical Engineering

Additional Examiner

## Abstract

The biomechanics of the cervical spine during shear loading are not well-established as compared to other loading regimes. This deficit may be problematic as there is evidence that shear loading may contribute to fracture-dislocation injuries, which often lead to spinal cord injury. Because of this deficit, existing safety standards, such as those used in the automotive industry, may not provide sufficient protection against spinal cord injuries in the cervical region. The present work aims to address this deficit in two ways: through the characterization of the load-displacement behaviour of the cervical spine during shear loading, and through an analysis of the effect of test apparatus design on specimen artefact loading during shear testing.

In the mechanical testing phase of the project, fresh-frozen human cervical functional spinal units were loaded to 100 N using a materials testing machine and custom-designed test apparatus. Three directions (anterior, posterior, lateral) were tested in each of three specimen conditions (intact, posterior ligamentectomy, disc-only). Significant decreases in stiffness were found in both the anterior ( $\Delta 81$  N/mm) and posterior ( $\Delta 15$  N/mm) directions between the intact and disc-only conditions, respectively.

A computational model was then developed to investigate the effects of test apparatus design on artefact loading and coupled rotations, which had proved problematic during previous attempts to apply axial compression preloads during shear testing. Three axial compression force application methods (point load, rotationally constrained, follower load) were modeled during testing up to 10 mm anterior shear, with axial compressive loads up to 800 N for each method. A subset of the simulations were validated experimentally using porcine functional spinal units. It was found that the follower load provided the best reduction of both artefact moments and coupled flexion-extension rotations.

This work provides additional scope to existing shear biomechanics data, as well as insight into how test apparatus design may influence results during shear testing of the cervical

spine. These results may be used to improve the definition and validation of existing finite element models of the human neck, where such models may reduce the incidence or severity of spinal cord injury through improved automotive safety.

## **Lay Summary**

Conducting biomechanics testing is essential to establishing the behaviour of the human body during injurious events such as motor vehicle accidents. In this thesis, different aspects of biomechanical testing of the neck are investigated in order to have a better understanding of its behaviour when shearing loads occur (forces that act parallel to the ground when sitting upright, as might occur if struck in the face). Investigating this is important, as these loads might contribute to spinal cord injury, which is a devastating and presently incurable condition. It is hoped that findings from this thesis will be used to improve existing physical and computer models of the neck. The aim of these computer models is to allow simulations of how accidents might injure the persons involved. Insights from these simulations might allow for better safety standards to be created, which could potentially reduce the occurrence of spinal cord injuries from motor vehicle incidents and other traumatic events.

## **Preface**

A version of Chapter 2 is in preparation for publication. I was responsible for carrying out the testing, data analysis and writing of the manuscript. Assistance with testing, advice on experimental design and editing was provided by Angela Melnyk. Remco Doodkorte was involved in developing the original testing methodology and in the design of the test apparatus used. Tom Oxland and Peter Cripton provided the conceptual framework for the manuscript, advised on methodology and data analysis, and provided editing for the manuscript.

For the computational work carried out in Chapter 3, I was responsible for the model development, development of the testing matrix and analysis of the simulation results. Tom Oxland and Peter Cripton suggested the use of this method, provided input on the focus of the investigation, and advised on the data analysis process. For the experimental verification work carried out in Chapter 4, I was responsible for carrying out the testing, test apparatus design modifications, experimental design and data analysis. Ali Forghani assisted with the test apparatus design modifications and fabrication, and assisted with testing. Tom Oxland and Peter Cripton guided the experimental design, assisted with data analysis and provided input on the apparatus design modifications.

The experimental work in Chapter 2 was performed with approval from the University of British Columbia Human Ethics Board (H16-00072: Cervical Shear).

# Table of Contents

Abstract .....	iii
Lay Summary .....	v
Preface .....	vi
Table of Contents .....	vii
List of Tables .....	ix
List of Figures .....	x
List of Acronyms .....	xii
Acknowledgements .....	xiii
Dedication .....	xiv
1 Introduction .....	1
1.1 Motivation .....	1
1.2 Literature Review .....	2
1.2.1 Anatomy of the Cervical Spine .....	2
1.2.2 Epidemiology of Spinal Column Injuries in the Cervical Spine .....	7
1.2.3 Prevention of and Risk Assessment for Cervical Spine Injuries .....	12
1.2.4 Biomechanical Testing of the Cervical Spine .....	18
1.2.5 Test Apparatus Design Challenges in Mechanical Testing of the Spine .....	21
1.3 Research Objectives .....	26
2 Load-displacement characteristics of human cervical FSUs during shear loading .....	27
2.1 Purpose .....	27
2.2 Methods .....	27
2.2.1 Specimen Preparation .....	27
2.2.2 Apparatus Design & Load Application .....	29
2.2.3 Data Collection and Analysis .....	32
2.3 Results .....	35
2.3.1 Stiffness .....	35
2.3.2 Kinematics .....	36
2.4 Discussion .....	38
3 Analysis of Shear Test Apparatus Design .....	45
3.1 Purpose .....	45
3.2 General Model Development .....	48
3.3 Question 1: Effect of different axial compression methods .....	51
3.3.1 Specific Model Development .....	51

3.3.2	Simulation Results .....	56
3.3.3	Discussion .....	60
3.4	Question 2: Effect of follower load guide position.....	64
3.4.1	Specific Model Development .....	64
3.4.2	Simulation Results .....	68
3.4.3	Discussion .....	74
3.5	Summary of Simulation Findings.....	79
4	<i>Ex-vivo</i> Validation of Design Analysis .....	80
4.1	Purpose .....	80
4.2	Methods .....	82
4.3	Results.....	88
4.3.1	Overall Loading and Kinematics.....	88
4.3.2	Artefact Flexion-Extension Moments during Different Axial Compression Methods.....	89
4.3.3	Flexion-Extension Rotations .....	93
4.4	Discussion .....	95
4.5	Design Recommendations.....	102
5	Conclusion .....	104
	References .....	108
	Appendices.....	112
	Appendix A: $N_{ij}$ Formula.....	112
	Appendix B: Kinematics algorithm .....	113
	Appendix C: Full Results for Chapter 2 .....	117
	Appendix D: Counterbalance System Error Analysis .....	118
	Appendix E: ADAMS moment computation algorithm .....	119
	Appendix F: AMTI MCA-6-500 Calibration Matrix.....	121
	Appendix G: Full Experimental Results for Each Axial Compression Method & Specimen, Cycle 3.....	122
	Appendix H: Follower Load Guide Drawings .....	124
	Appendix I: Photographs of Chapter 4 Experimental Set-up .....	126

## List of Tables

Table 1-1: Mechanistic Classification of Common Cervical Spine Injuries.....	10
Table 1-2: Comparison of existing shear biomechanics studies according to test apparatus constraint type .....	24
Table 2-1: Specimen and donor information .....	28
Table 3-1: Material Property and Geometry Definitions Used for Rubber Specimen.....	50
Table 3-2: Directional Stiffness Properties Used for Cadaver-based Specimen Simulation .....	51
Table 3-3: Comparison of the Three Simulated Axial Compression Methods.....	52
Table 3-4: Sample simulation outputs for rubber specimen at 10 mm anterior shear with a 300 N compressive force .....	56
Table 3-5: Sample simulation outputs for cadaveric specimen (mean, low stiffness) at 10 mm anterior shear with a 300 N compressive force .....	58
Table 3-6: L1 and L2 dimension cases assessed in multibody dynamics model and mathematical model .....	67
Table 4-1: Sample comparison of low stiffness simulation outputs to experimental results at peak applied anterior shear displacement (3.0 mm) for Pig 1, C7-T1 .....	88
Table 4-2: Regression coefficients, Standard Error and $R^2$ for linear fit of experimental artefact moment measurements.....	92
Table 4-3: Comparison of findings from shear test simulations and experimental results .....	96

## List of Figures

Figure 1-1: Anatomy of the Human Cervical Spine .....	3
Figure 1-2: Bony anatomy of the cervical spine .....	4
Figure 1-3: Physiological Movements (upper) and Types of Loading (lower) in the Cervical Spine .....	5
Figure 1-4: Key ligamentous structures in the cervical spine .....	7
Figure 1-5: Lateral radiograph of a BFD in at C6-C7 .....	11
Figure 1-6: Experimentally-derived logistic regression curves for assessment of neck injury risk at two AIS levels according to Nij Score.....	13
Figure 1-7: Example of an $N_{ij}$ score time trace during a frontal impact test .....	15
Figure 1-8: Three Categories of Existing Shear Test Apparatus Design .....	22
Figure 2-1: Specimen Preparation with Wood Screws and Wire Gauge.....	29
Figure 2-2: Alignment of Specimen in Potting Rig.....	29
Figure 2-3: Shear Test Apparatus - Anterior-Posterior Test Configuration .....	30
Figure 2-4 Shear Test Apparatus - Lateral Shear Test Configuration .....	30
Figure 2-5: Lateral View of the Ligaments Cut Condition (red arrows show location of cut).....	32
Figure 2-6: Posterior View of the Disc-Only Condition (red arrows show removed posterior elements).....	32
Figure 2-7: Anatomical Coordinate System Definition and Alignment Relative to Apparatus-Mounted Rigid Body Markers .....	33
Figure 2-8: Mean stiffness and range of the cervical FSU during shear loading.....	36
Figure 2-9: Anterior-posterior loading cycle for each specimen in the intact condition .....	37
Figure 2-10: Right lateral loading cycle for each specimen in the intact condition.....	37
Figure 2-11: Comparison of shear stiffness results from present work to previous works .....	41
Figure 3-1: Shear test apparatus with point load axial compression.....	46
Figure 3-2: ADAMS Model of the Shear Test Apparatus at $t=0$ (above) and $t>0$ (below) .....	49
Figure 3-3: Visualization of applied forces during the (a) point load, (b) rotational constraint, and (c) follower load before and after anterior shear displacement .....	52
Figure 3-4: Measurement of L1 and L2 in the follower load method at 0mm shear displacement (L1=50 mm, L2=50 mm shown) .....	54
Figure 3-5: Simulated effect of different compressive force application methods on flexion-extension moment at 10 mm anterior shear in a rubber specimen model .....	57
Figure 3-6: Simulated effect of different compressive force application methods on flexion-extension moment at 10 mm anterior shear in a cadaveric specimen .....	59
Figure 3-7: Simulated effect of different compressive force application methods on peak flexion-extension rotation at 10mm anterior shear in a cadaveric specimen .....	60
Figure 3-8: Annotated diagram of artefact loading imparted during use of follower load method in a FSU, after some anterior shear displacement and flexion.....	65
Figure 3-9: Measurement of L1 and L2 in the follower load method at 0mm shear displacement (L1=50 mm, L2=85 mm shown) .....	66
Figure 3-10: Mathematical model predictions of the effect of different follower load guide positions on specimen artefact loading .....	68
Figure 3-11: ADAMS simulation predictions of the effect of different follower load guide positions on specimen artefact moments (blue) and artefact shear loading (orange) in a rubber specimen model.....	70

Figure 3-12: ADAMS simulation predictions of the effect of different follower load guide positions on specimen artefact moments (blue) and artefact shear loading (orange) in a mean stiffness FSU .....	72
Figure 3-13: ADAMS simulation predictions of the effect of different follower load guide positions specimen artefact moments (blue) and artefact shear loading (orange) in a low stiffness FSU	72
Figure 3-14: Simulated effect of follower load guide position on flexion-extension rotation in a low stiffness FSU model .....	73
Figure 3-15: Effect of type of specimen movement and L1, L2 guide positions on artefact shear forces .....	76
Figure 4-1: Test Apparatus set-up for verification tests – point load (top), rotationally constrained (middle), follower load (bottom) .....	84
Figure 4-2: Comparison of experimental data (dots) with linear fit (solid line) and simulation (dashed line) artefact flexion-extension moments during anterior shear testing .....	91
Figure 4-3: Comparison of experimental data (dots) with linear fit (solid line) and simulation (dashed line) flexion-extension rotation during anterior shear testing .....	94
Figure 4-4: Flexion-extension rotation during application of anterior shear load in omitted trial	99

## **List of Acronyms**

AIS – Abbreviated Injury Scale

ASIA – American Spinal Injury Association

ATD – Anthropometric Test Device

BFD – Bilateral Facet Dislocation

FSU – Functional Spinal Unit

LVDT – Linear Variable Differential Transformer

MVA – Motor Vehicle Accident

NHTSA – National Highway Traffic Safety Administration

ODAU – Optotrak Data Acquisition Unit

SCI- Spinal Cord Injury

UFD – Unilateral Facet Dislocation

## **Acknowledgements**

A special thanks to the many who supported and assisted me during the completion of my master's thesis research work.

In particular, I would like to thank my co-supervisors, Drs. Tom Oxland and Peter Crompton for guiding through the research landscape. Your help streamlined my thinking, allowed me to ask the right questions and become a stronger researcher. I would also like to acknowledge the Rick Hansen Institute and the Blusson Integrated Cures Partnership for providing funding for this work.

I would also like to thank the opportunity to thank our OIBG staff and students for providing personnel support, technical advice and moral support during the completion of my project. The expertise and attentiveness of our research engineers, Angela Melnyk and Dr. Ali Forghani was essential during the design and experimental testing phases of my project. I would also like to acknowledge Dr. Robin Coope of the BC Cancer Agency, for all his input and assistance with the design and manufacturing of the shear test apparatus, as well as Remco Doodkorte, Angela Melnyk and Dr. Tom Whyte for their contributions to its design.

Finally, a very special thanks to all those OIBG lab members who assisted me on my experimental test days, no matter how squirrely I became.

## **Dedication**

To my parents, for encouraging me to ask questions and never settle for the status quo. But also, to the lab scrap parts bin, for teaching me that sometimes the quest for hope involves a bit of dumpster diving.

# 1 Introduction

## 1.1 Motivation

While relatively rare in incidence, spinal cord injury (SCI) can have devastating consequences from a personal, social and economic perspective for both the patients affected and society as a whole. Because SCI is currently incurable, and places a high burden on patients and the healthcare system, prevention of SCI is a research priority.

Since motor vehicle accidents (MVAs) present a major source of SCI worldwide, improvements in automotive safety may stand to reduce the incidence and/or severity of SCI. While automotive safety standards that are intended to provide some protection against serious injuries (such as SCIs) are mandated in most countries, there are a number of limitations that exist with current testing methods and standards.

Fundamentally, the main limitation that exists with existing automotive safety standards that aim to protect against SCI is a lack of comprehensive understanding of the biomechanics of the spine. Because safety standards must be informed by evidence, gaps in knowledge may contribute to standards being insufficiently protective in scenarios that have not been studied.

In the cervical spine (neck) region, the biomechanics during shear loading have received little attention as compared to other loading modes. This may be a concern as there exists some evidence that such loads may contribute to, or be largely responsible for certain spinal column injuries (eg. displaced or broken bones in neck) that lead to SCI. As such, an improvement in our understanding of the response of the cervical spine to shearing loads may contribute to more protective automotive safety standards, and thus potentially reduce the incidence or severity of SCI emanating from MVAs.

The aim of the present work was to investigate the biomechanics of the cervical spine during shearing loads, as well as to investigate how testing methodology may influence the behaviour of the spine during shearing loads. It is hoped that this work will contribute to the reduction of SCI incidence through improved safety standards, as well as inform future biomechanical testing of the spine such that results can be more readily translated to injury models.

## **1.2 Literature Review**

### **1.2.1 Anatomy of the Cervical Spine**

The human spine is subdivided into four regions based on anatomy and functional differences. These regions are known as the cervical, thoracic, lumbar and sacral regions. The cervical spine comprises the seven superior-most bony vertebrae of the spinal column, and their surrounding tissues. Physiologically, the cervical spine acts to support the skull, to facilitate movement of the head and to protect the spinal cord and peripheral nervous tissues.

The cervical spine is typically defined as beginning at the junction of the occiput bone of the skull (C0) with the first vertebra (C1) and terminating at the junction between the first vertebra of the thoracic region (C7 and T1) (McElhaney & Myers, 1993). Vertebrae between C0 and C7 are numbered accordingly. The location and overall structure of the cervical spine can be seen in Figure 1-1.

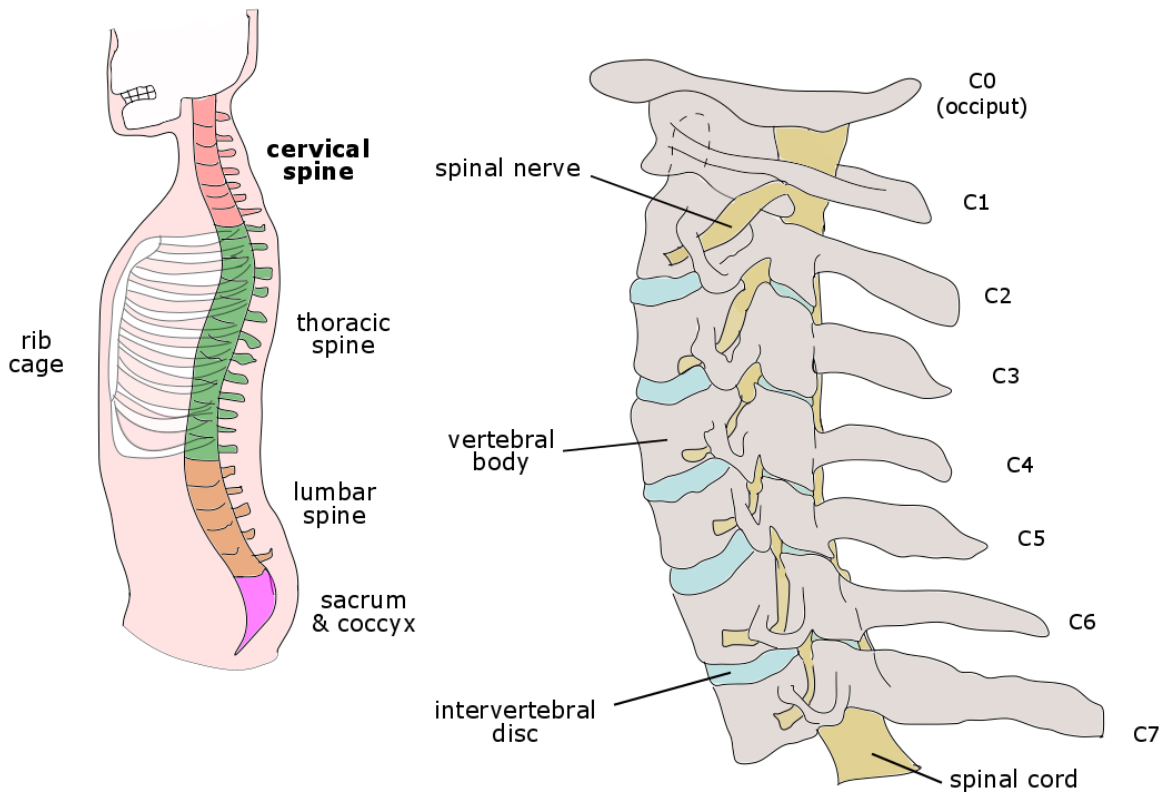
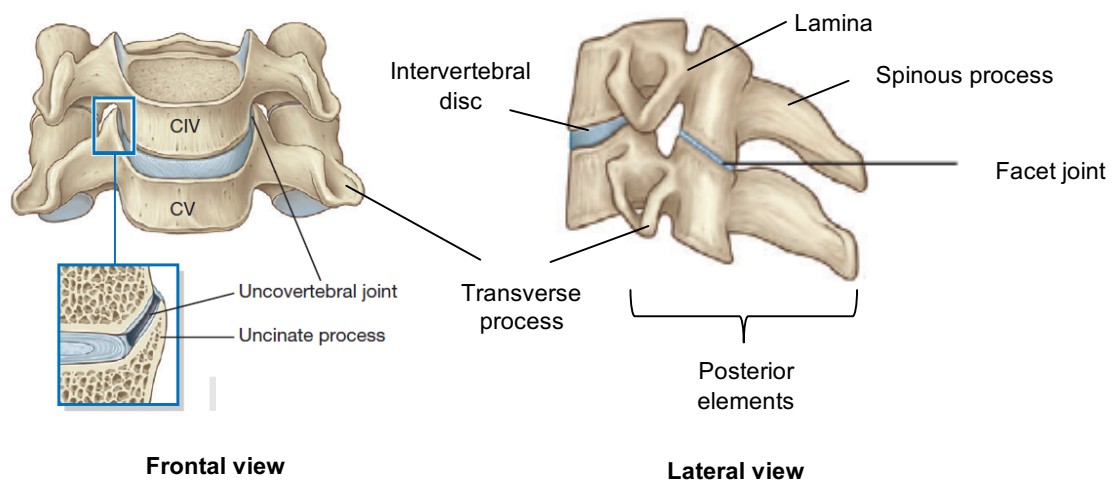


**Figure 1-1: Anatomy of the Human Cervical Spine**

The cervical spine may be further subdivided into the upper cervical spine, consisting of C0-C1 through C1-C2, and the lower cervical spine, consisting of C2-C3 through C7-T1 (McElhane & Myers, 1993). This sub-classification of the cervical spine is in acknowledgement of the anatomical and functional differences in these two sub-regions; the vertebra of the upper cervical spine articulate solely through synovial joints, whereas the vertebra of the lower cervical spine are separated and connected by intervertebral discs that act as symphysis joints, as seen in the rest of the spine (Myers & Winkelstein, 1995).

In the lower cervical spine, each spinal level has a similar morphology. Key bony features of the vertebra in this region include the vertebral body, which acts primarily to transfer

forces through the spinal column, the paired sets of superior and inferior articular processes, which form the facet joints (synovial joints) between adjacent vertebra, the spinous process, the lamina, and the uncinata processes, which form the uncovertebral joints (Myers & Winkelstein, 1995; Middleditch & Oliver, 2005). These structures may be seen in Figure 1-2. Compared to vertebrae in other spinal regions, those of the lower cervical spine are smaller in size, have a more curved vertebral endplate (owing to the uncinata processes, which are not present outside of the cervical spine) and have obliquely oriented facet joints.

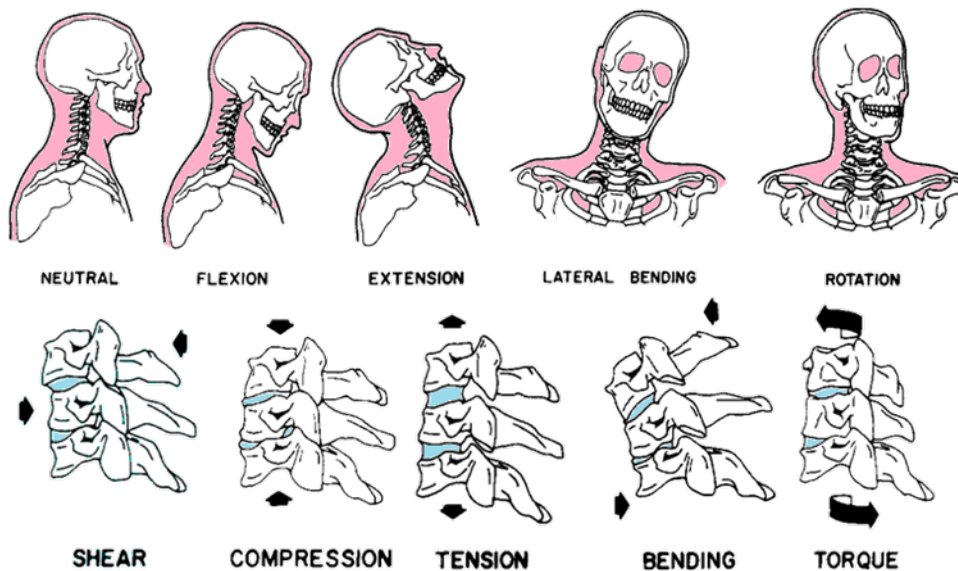


Adapted from Drake *et al*, 2012

**Figure 1-2: Bony anatomy of the cervical spine**

These differences in bony anatomy reflect the cervical spine's dual roles of providing sufficient mobility and structural support for the head while providing protection to the spinal cord. The safety of the spinal cord in this region is of particular importance as signalling for life-sustaining body functions (eg. control of heart, breathing) pass through the cervical region, such that damage to the cord in this region may result in death or significant physical impairment (eg. inability to breathe unassisted, loss of sensory/motor function). Thus, excessive motion is undesirable in the cervical spine.

As described previously, FSU motion is permitted by three joints: the intervertebral disc, the laterally paired facet joints and the laterally paired uncovertebral joints (Figure 1-2). Together, these joints allow some motion in each linear direction (anterior-posterior, inferior-superior, right-left lateral) and each rotational direction (flexion-extension, right-left axial rotation, right-left lateral bending) at each level and in the cervical spine as a whole. These physiological movements are illustrated in Figure 1-3. Each spinal level has a different contribution to overall spine movement. In the lower cervical spine, flexion-extension is possible up to 20 °, while up to 10 ° of both lateral bending and axial rotation are possible, depending on the vertebral level (Panjabi & White, 1980). The upper cervical spine allows for considerable axial rotation (C1-C2) and flexion-extension (C0-C1).



Adapted from McElhaney & Myers, 1993

**Figure 1-3: Physiological Movements (upper) and Types of Loading (lower) in the Cervical Spine**

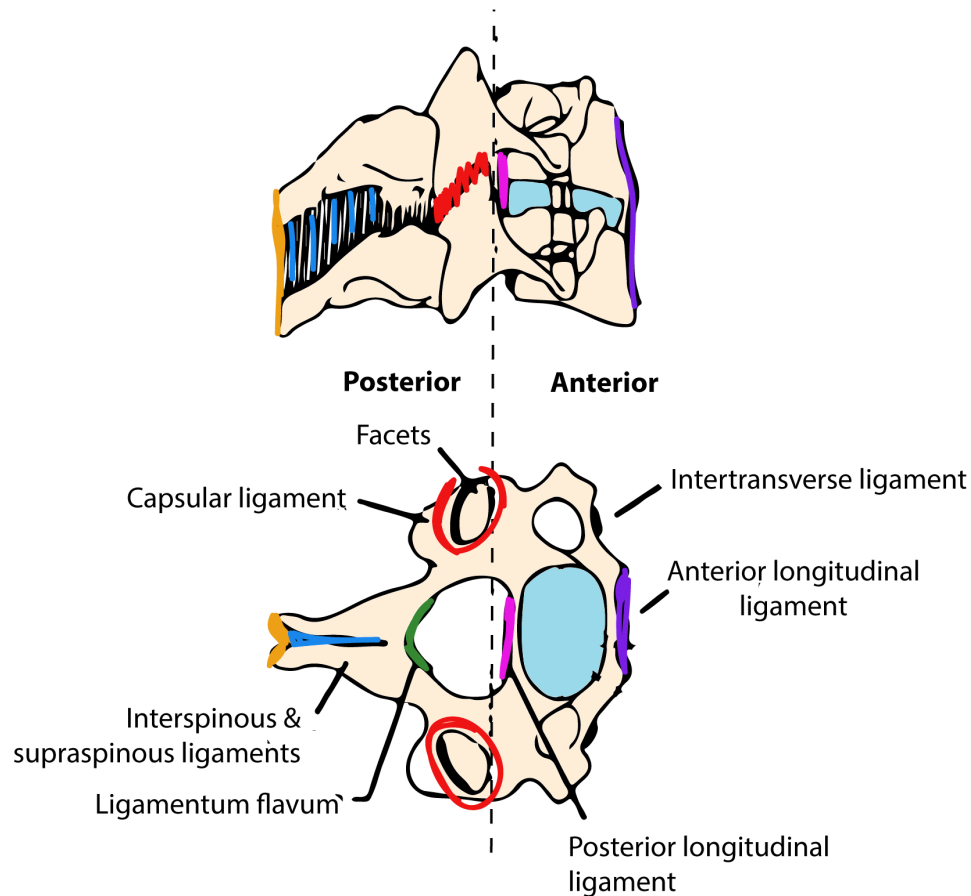
The intervertebral disc is classed as a symphysis joint, where the disc itself consists of the exterior fibrocartilaginous annulus fibrosus, which fuses into the vertebral endplate, and the interior gel-like nucleus pulposus (Drake *et al*, 2012). The disc provides shock absorption and

load-transfer between vertebral levels, but also allows for some motion in each direction (Panjabi & White, 1980). Similar to other biological tissues seen in joints, the disc is viscoelastic and exhibits rate-dependency, anisotropy and creep, enabling it to respond to physiological loading in an optimal manner that prevents tissue damage or pain. With degenerative changes, water content is lost from the nucleus leading to reduced shock absorption and load-transfer capabilities (Buckwalter, 1995). Degeneration may occur as a natural result of aging, or due to abnormal loading resulting from injury (Buckwalter, 1995).

The facet joints are classed as synovial joints, and are enclosed by the capsular ligament. In the cervical spine, the facet joints are oriented obliquely in the sagittal plane, allowing for some motion in all directions, load-transfer between vertebral levels and facilitating flexion-extension (Drake *et al*, 2012).

The lower cervical spine also features uncovertebral joints, which are classed as pseudojoints. The term pseudojoint refers in this case to a joint that has a synovial membrane and synovial fluid, but lacks a joint capsule seen in true synovial joints (Ombregt *et al*, 2013). The uncovertebral joints are lateral to the intervertebral disc (Figure 1-2), and may act to limit lateral translation.

As a whole, the spine includes a large number of ligamentous and muscular tissues and complex patterns of origin and insertion. Some of these structures act longitudinally through multiple spinal levels, while others act locally between individual vertebrae. Key ligamentous structures in the lower cervical spine include the anterior longitudinal ligament and the posterior longitudinal ligament, which run the entire length of the spine, providing support on the anterior and posterior aspects of the vertebral body and intervertebral disc joints (Drake *et al*, 2012). Others include the supraspinous ligaments, interspinous ligaments, ligamentum flavum and the capsular ligament, which act between adjacent spinal levels on the posterior elements of the spinal column (Drake *et al*, 2012). These key ligaments are illustrated in Figure 1-4.



Adapted from McElhaney & Myers, 1993

**Figure 1-4: Key ligamentous structures in the cervical spine**

To simplify the consideration of the spine, the concept of the functional spinal unit (FSU) is often discussed. An FSU is defined as a pair of adjacent vertebra, including all ligamentous tissue connecting the two structures and the intervertebral disc (Panjabi & White, 1980).

### 1.2.2 Epidemiology of Spinal Column Injuries in the Cervical Spine

Acute, traumatic injuries to the cervical spine are of particular concern beyond isolated structural damage to the musculoskeletal tissue of the spine. With spinal column injury, there is some risk of damaging the spinal cord as a result of intrusion or occlusion of the spinal canal. Damage to the spinal cord may occur as direct result of the mechanical deformation (primary

injury), whereby bony or soft tissue elements may impact, pierce, or transect the spinal cord. Following this, secondary injury resulting from biological processes such as the inflammatory response may cause further damage to the spinal cord (Sekhon & Fehlings, 2001). Although SCI affects a relatively small number of persons worldwide (15-40 new cases per million annually), the personal, social and economic consequences of SCI can be devastating for those affected (Sekhon & Fehlings, 2001). In Canada, the lifetime economic burden for an individual with a traumatic SCI is between \$1.5-3.0 million, depending on injury severity (Kruger *et al*, 2013). This figure includes the direct costs (healthcare, medication, adaptive equipment/modifications) and indirect costs (quality-adjusted life year, life years lost).

Common activities or events leading to spinal column and spinal cord injuries in the United States include MVAs (38%), falls (30%), violence (14%), sports (9%) (National Spinal Cord Injury Statistical Centre, 2016). Owing to the nature of these activities, there exists a bimodal distribution for age of onset of SCIs; young persons aged 21-30 years are most commonly affected (25%) but older persons (>60 years) also make up a considerable portion (10%) of SCI patients (Sekhon & Fehlings, 2001), as falls are common in aging populations.

Within the previously described activities, headfirst impacts are considered to be a major source of injury, particularly in the cervical spine, where 25-50% of acute SCI patients are admitted with a related head injury (Sekhon & Fehlings, 2001). In a headfirst impact, the head comes to a sudden stop upon impacting a rigid surface, but there is some lag before the rest of the body stops due to inertia from the mass of the torso. Because the cervical spine connects the head and the body, it may experience large and potentially injurious loads and deformations during the time between the first impact of the head and the time when the entire body comes to a complete stop (Nightingale *et al*, 2000; Saari *et al*, 2011; Ivancic, 2012). The exact nature of the loads experienced by the cervical spine and the resulting injury may be affected by a number of factors including the change in velocity ( $\Delta V$ ) of the head and torso, the

magnitude and direction of impact forces, initial positioning of the body, impact surface geometry, and muscle activation during the event (Nightingale *et al*, 1997; Brault, Siegmund, & Wheeler, 2000; Ono, *et al*, 1997). Because of the complexity of factors affecting injury in the cervical spine and difficulty in accurate quantification of these factors in real-world accidents, mechanistic classification of injuries presents an ongoing challenge.

In the cervical spine, the current paradigm of spinal column injuries is that most are caused by excessive loading or motion in flexion-extension or compression-tension or combinations thereof. This paradigm is based on a variety of landmark cadaveric and *in vivo* studies in humans and animals (Mertz & Patrick, 1971; Prasad & Daniel, 1984; Mertz *et al*, 1978), where many severe types of traumatic spinal column injury were found to be associated with these loading modes. Table 1-1 (Myers & Winkelstein, 1995; McElhaney & Myers, 1993), summarizes the conclusions from previous studies that have investigated the mechanistic classification of various cervical spine injuries. From this table, it can be seen that most of the injury data is populated in the cells describing combinations of compression, tension, flexion and extension. Though one could interpret this as meaning that lateral bending, axial rotation and shear displacement do not contribute to serious injuries in the lower cervical spine, it would be more appropriate to state that the investigation of the effect of these loading modes has not been as thorough.

**Table 1-1: Mechanistic Classification of Common Cervical Spine Injuries**

	<b>Compr.</b>	<b>Tension</b>	<b>Flexion</b>	<b>Ext.</b>	<b>Lateral bending</b>	<b>Axial rotation</b>	<b>Shear</b>
<b>Compr.</b>	Endplate fx Burst fx Teardrop fx		BFD UFD Teardrop fx Wedge fx Burst fx	Hangman's fx (C2) Posterior element fx Disc rupture			
<b>Tension</b>		C1-C2 dislocation	BFD UFD	Hangman's fx (C2) Disc rupture Teardrop fx Whiplash			
<b>Flexion</b>							
<b>Ext.</b>							
<b>Lateral bending</b>					Nerve root avulsion		
<b>Axial rotation</b>						C1-C2 dislocation	
<b>Shear</b>							Odontoid (C1) fx C1-C2 dislocation

*fx=fracture*

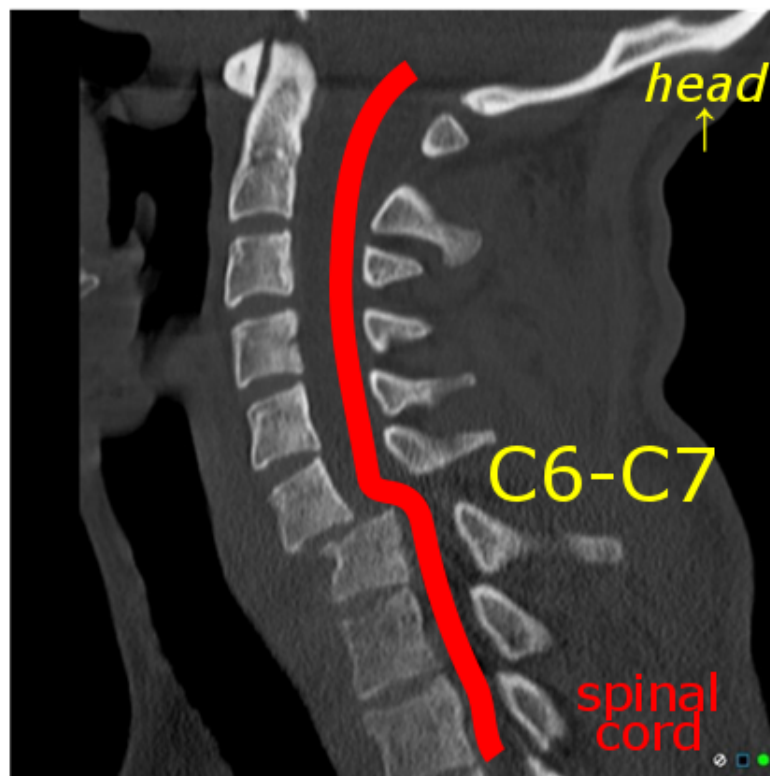
(Myers & Winkelstein, 1995; McElhaney & Myers, 1993)

*BFD= bilateral facet dislocation*

*UFD= unilateral facet dislocation*

In a clinical environment, spinal injuries are mainly classed according to bony morphology observed in post-injury radiographs. Damage to the spinal cord or peripheral nervous system is assessed separately using sensorimotor function tests such as the ASIA (American Spinal Injury Association) Impairment Scale. Thus, a clinician might describe an SCI patient according to the morphological abnormalities apparent in the spinal column, as well as their sensorimotor function capacity. Herein, the focus is on spinal column injuries.

Major clinical categories of spinal column injury include burst fractures of the vertebral body, fracture-dislocations such as the bilateral facet dislocation and unilateral facet dislocation (BFD, UFD respectively), and minor fractures such as compression fractures. Of these major injury types, fracture-dislocations are the most common vertebral column injury leading to SCI, accounting for 40% of adult SCI cases (Sekhon & Fehlings, 2001). In particular, the BFD injury (Figure 1-5) is considered one of the most severe spinal column injuries, resulting in neurological damage in 90% of cases (Wilson *et al*, 2013). In this injury, one or more vertebrae dislocate anteriorly relative to their normal position, disrupting both paired facet joints at the affected level(s). During this process, bony fractures in the posterior elements often occur.



Case courtesy of Dr Chris O'Donnell, Radiopedia.org, rID: 21424 (image adapted from original)

**Figure 1-5: Lateral radiograph of a BFD in at C6-C7**

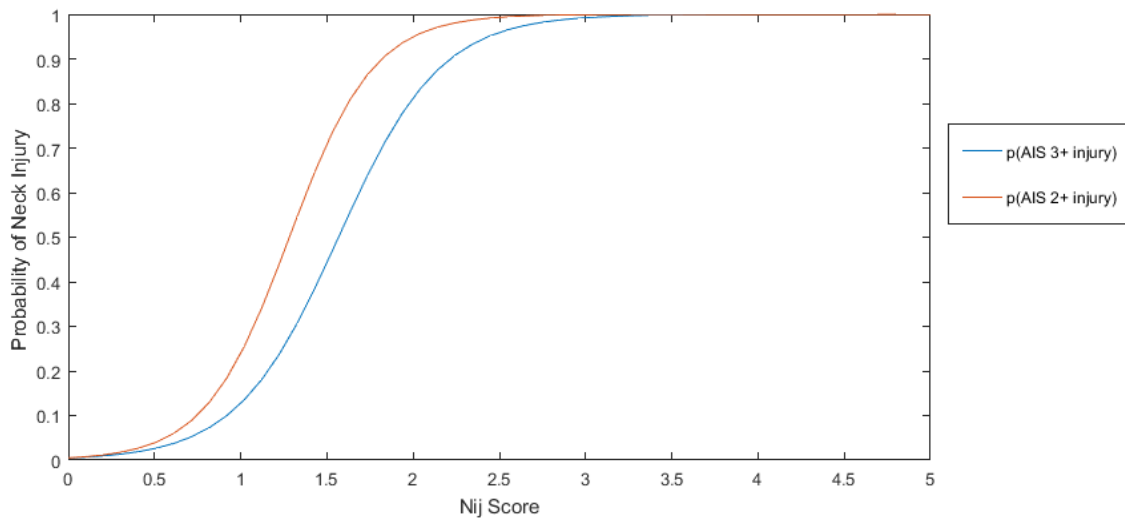
As seen in Table 1-1, the consensus from previous experimental work is that BFD is caused primarily by flexion moments and rotation, combined with either a compressive or tensile load. There is however, some indication that other loading modes such as anterior shearing forces might also contribute to this injury. In a 2008 study by Ivancic *et al*, in which BFDs were consistently simulated in a cadaveric FSU model with an acceleration sled, anterior shearing forces were found to be a key component during injury initiation. While the precise mechanistic cause of any particular injury may not necessarily be as critical in a clinical setting where treatment is needed, understanding how injuries like BFD occur is essential to the development of injury prevention technologies and development of adequate risk assessment metric. In this light, if the risk associated with shearing loads is not fully understood, appropriate consideration of these loads in risk assessment and injury prevention designs may not occur.

### **1.2.3 Prevention of and Risk Assessment for Cervical Spine Injuries**

Because SCI in the cervical spine typically represents a life-altering or life-threatening injury, prevention of traumatic cervical spine injuries that can cause SCI is a priority. Much of the focus in prevention and risk assessment for SCI is directed towards MVAs. This is because MVAs represent the largest cause of SCI (Sekhon & Fehlings, 2001), and because driving is an activity of daily life that is largely unavoidable in developed nations. Because sport is also a major cause of traumatic SCI (Sekhon & Fehlings, 2001), there is also much interest in various sporting industries/organizations (such as football, hockey, alpine sports, cycling, equestrian, diving) to reduce the incidence and severity of SCI (McIntosh & McCrory, 2005).

For many traumatic injuries (including cervical spine injury), injury tolerance is established from logistical regression of experimental injury data for different injury severity levels. Injury severity is often defined using the AIS (Abbreviated Injury Scale), which classifies common injuries on a scale of 1 to 6, where 6 is a currently untreatable injury (Greenspan *et al*, 1985). From the logistical regression of experimental data for a particular AIS level, it is possible to

determine the probability of sustaining that injury severity from some input metric (ie. force, displacement, energy etc.). From this, injury criteria can be created based on what is considered to be a “reasonably” low risk for certain AIS injury levels. Figure 1-6 shows the logistic regression curves drawn for the risk of AIS 2+ and AIS 3+ neck injuries using the  $N_{ij}$  score as a metric (described in further detail shortly).



(Kleinberger *et al*, 1998)

**Figure 1-6: Experimentally-derived logistic regression curves for assessment of neck injury risk at two AIS levels according to  $N_{ij}$  Score**

In the United States and Canada, all consumer vehicles must adhere to various standards established by the US-based National Highway Traffic Safety Administration (NHTSA). NHTSA defines numerous injury tolerance criteria and minimum performance standards that are intended to protect vehicle occupants and pedestrians from severe injury during survivable accidents. These standards manifest in physical testing of vehicles in accident scenarios, where Anthropometric Test Devices (ATDs) or “crash test dummies” act as surrogate humans. The ATDs are instrumented with various sensors in different body regions, and are designed to respond physically in a way that is similar to a human body so that injury risk may be assessed in a simulated accident. Key force and kinematic data from the ATDs during simulated crashes

are used to provide some indication of how a living human might fare in a similar scenario, and are compared against specific injury criteria. Performance relative to these injury criteria are used to decide if a vehicle may be sold on the market.

For the cervical spine, the main injury criterion used to assess the risk of a severe injury is the Neck Injury Criterion ( $N_{ij}$ ), which is detailed in the FMVSS (Federal Motor Vehicle Safety Standards) 208 Occupant Safety Standard (Kleinberger *et al*, 1998; Eppinger *et al*, 2000). The  $N_{ij}$  is assessed during frontal crash tests, where data from a 6-axis load cell located at the head-neck junction of the Hybrid III ATD neck (equivalent to C0-C1 in a human) is analyzed throughout the crash. Although 6-axis data is collected, only compressive-tensile forces and flexion-extension moments are considered during analysis. This is largely because there is not sufficient data on the tolerance of the cervical spine to other loading modes to create an injury criterion that includes them.

In the  $N_{ij}$  the combination of normalized compressive-tensile force and normalized flexion-extension moment are plotted for each time instant (Figure 1-7). Forces and moments are normalized according to injury thresholds in each direction for the particular mass and sex of the ATD being analyzed. If any data point during the crash falls outside the green diamond, representing an  $N_{ij} \geq 1.0$ , then it is said that there is an excessive risk of neck injury. For the  $N_{ij}$ , a failing score of  $>1.0$  confers a  $>15\%$  risk of an AIS 3+ injury (Kleinberger *et al*, 1998), which corresponds to a “serious” injury. Thus, if Figure 1-7 represented results from a crash test, this vehicle would fail the  $N_{ij}$  as numerous data points throughout the test fall outside of the green diamond.

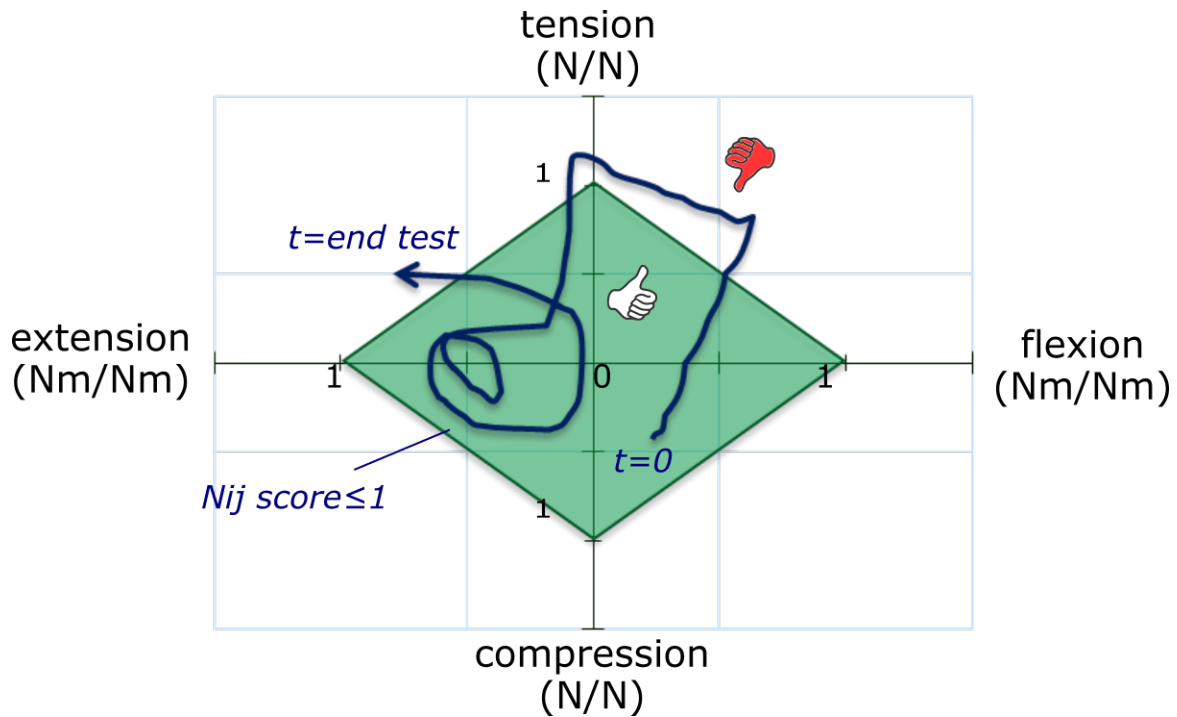


**Figure 1-7: Example of an  $N_{ij}$  score time trace during a frontal impact test**

The  $N_{ij}$  is calculated as follows, where the critical loads for specific ATDs may be found in Appendix A:

$$N_{ij} = \frac{F_{compression-tension}}{F_{critical}} + \frac{M_{flexion-extension}}{M_{critical}} \quad (\text{Kleinberger } et \text{ al, 1998})$$

There exist a few other injury criteria pertaining to the cervical spine, such as the Neck Protection Criterion ( $N_{km}$ ), Neck Injury Criterion (NIC) and Lower Neck Load (LNL) (Schmitt *et al*, 2014). Both the  $N_{km}$  and LNL include anterior-posterior shear neck loads in their formulations, while the NIC includes the anterior-posterior acceleration and velocity of the ATD head relative to the torso. However, these injury criteria were developed for use in low speed, rear-end collisions (Schmitt *et al*, 2014) and are not used in any current NHTSA standard.

While NHTSA standards such as the FMVSS 208, first introduced in 1967, and most recently amended in 2000, have made inroads into improving vehicle safety (NHTSA, 2013), there exist many limitations with crash testing using ATDs. Because crash testing is costly and ATDs must be designed to behave biofidelically for each specific accident scenario, only a limited number of accident scenarios are recreated in standard testing. This may mean that some deficiencies in safety design may not be apparent in the current testing regime, as real-world MVAs involve many variables that are not currently featured in crash testing.

There also exist many limitations with the use of ATDs themselves. Although adult female, adult male, child and infant ATDs of varying body sizes exist to capture the effect of variations in occupants, other subject-specific variables are known to affect injury risk and are not fully accounted for (Crandall *et al*, 2011). Muscle forces are also neglected in ATDs, where muscle activation as a result of bracing or anticipation of events may occur in real-world accidents such that injury risk is altered (Crandall *et al*, 2011).

With regard to the neck design of the Hybrid III ATD, which is used to assess the  $N_{ij}$ , there also exist some limitations. As load cells do not span the length of the cervical spine, loads at other spinal levels cannot be evaluated. This may be problematic if injurious loads in real-world accidents are occurring in these locations. The Hybrid III neck and spine is also known to be more rigid than comparably-sized whole human cadaveric specimens in flexion-extension, due to simplifications inherent in its construction (Crandall *et al*, 2011).

One potential solution to some of the issues and limitations presented by the use of vehicle testing and ATDs to assess occupant injury risk is the use of Finite Element Analysis (FEA) to model the tissue response in the human body (DeWit & Cronin, 2012). FEA is already used heavily in the automotive industry to assess the mechanical components of vehicles, and with the development of a biofidelic model of a human, it would be possible to augment existing ATD testing with FEA simulations. This would complement other modeling methods that are

already used, such as MADYMO (a proprietary multibody dynamics software, developed specifically for transportation applications) and experimental models (*ex vivo* specimens, mechanical surrogates). Using FEA would allow for expanded accident variables (eg. multiple vehicles, different road surfaces) and tailored occupant characteristics (eg. modeling more vulnerable populations, modeling out-of-position sitting postures) at a relatively low cost. Such testing may become especially important with the introduction of autonomous vehicles, where the types of real-world accidents seen may become more variable as occupant behaviour changes (particularly their positioning).

Although using FEA to augment existing testing required by government safety standards is a compelling proposal, it has not yet been fully realized. Currently, a whole-body human FEA model is being developed by the Global Human Body Models Consortium (GHBMC), which is a collaboration between various automotive industry partners and biomechanics researchers at various institutions (Gayzik *et al*, 2011; Barker *et al*, 2017). The aim of the GHBMC project human FEA model is that it be used primarily in the automotive industry for injury risk assessment and for injury criterion development, but it would also have useful applications in injury research, sports equipment design, and in military personnel protection.

One of the biggest challenges with developing such a model is defining the properties of the various biological structures and in validating the model. Because biological materials typically have more complex response behaviours (anisotropy, rate dependency, creep etc.) as compared to traditional engineering materials and a great deal of variability between individuals, defining such properties relies heavily on the existence of extensive *ex-vivo* and *in-vivo* subject tissue testing. Similarly, model validation relies heavily on the existence of biomechanics testing under controlled circumstances against which to compare the FE model response. This is

especially challenging in the spine, owing to the complexity of the structure as compared to other joint systems.

As with the  $N_{ij}$ , the neck portion of the GHBM model might be improved by having a more complete understanding of the behaviour of the human cervical spine, as limitations in existing biomechanics research preclude increased complexity beyond what has already been implemented (Shateri & Cronin, 2015; Barker *et al*, 2017).

Though this lack of complexity in current models may not be problematic for many accident scenarios, it is possible that factors that are not currently considered may give the result that existing safety standards and the vehicle design features that are based on these standards are not sufficiently protective in some situations. Thus, having a more complete understanding of the biomechanics of the cervical spine may contribute positively to the reduction of SCI emanating from MVAs, one of the most common sources of SCI.

#### **1.2.4 Biomechanical Testing of the Cervical Spine**

Biomechanical testing is essential to the process of establishing injury tolerance thresholds, which may be used to develop injury criteria and consumer safety standards. In the spine, the structural properties of skeletal and ligamentous components are often evaluated in *ex-vivo* specimens, as obtaining accurate data may require testing methods that are too invasive to be done *in vivo*. *In-vivo* testing is more commonly used to investigate features such as muscle response, nervous system function, or kinematics which can only be evaluated in a living organism.

Although some tissues do experience post-mortem changes in material properties, fresh-frozen intervertebral discs, and bony, cartilaginous, and ligamentous tissues exhibit minimal material property changes, and respond in a repeatable manner to loading (Johannessen *et al*, 2004; Panjabi *et al*, 1985). Thus, *ex-vivo* biomechanical properties obtained from these tissues

are considered to be a reasonable representation of those in living persons. Because *ex-vivo* specimens lack active musculature it is common to use boundary conditions or actuators attached to tendinous insertion points (Giles *et al*, 2014) to mimic physiological loading from active musculature, and/or external loading and internal loading from other body structures.

In the cervical spine, much of the previous biomechanics research has focused on its response to flexion-extension moments and compressive-tensile loads, or these motions (Schmitt *et al*, 2014; McElhaney & Myers, 1993; Myers & Winkelstein, 1995; Panjabi *et al*, 1986). The basic biomechanical behaviour and injury tolerance of the cervical spine in other loading modes, such as anterior-posterior shear, right-left lateral shear, lateral bending and axial rotation have been studied less often. There do exist some experimental studies that have focused on the shear biomechanics in the human lumbar spine (Skrzypiec *et al*, 2012; Melnyk *et al*, 2015; Berkson *et al*, 1979) and in porcine cervical spines (Yingling & McGill, 1999). However, because of morphological differences between the human lumbar and cervical regions and between the cervical spine in humans and cervical spine in pigs, the results from these studies are not directly translatable to the human cervical spine.

To date, only three experimental studies have focused on the shear biomechanics in the human cervical spine. While these studies do provide some insight into the shear biomechanics of the cervical spine, there exist some limitations with these studies as a whole that preclude their being included in existing models of the cervical spine and/or injury tolerance criteria. The first study on this topic is Panjabi *et al* (1986), which investigated the coupled rotations and translations of cervical FSUs with small displacements and rotations in each of the six anatomical directions. This study established that some small coupled rotations and translations occur in the cervical spine during the application of small shearing loads. This study also established that unlike in other loading directions, the response to shearing loads in the cervical FSU is approximately linear. In other loading directions, such as flexion-extension, a

characteristic “s-shaped” load-displacement curve is typically observed, where there exists a small region of extremely low stiffness (termed the “neutral zone”) about the neutral, 0 mm displacement position (Panjabi, 1992).

The second study on this topic was Moroney *et al* (1988). In this study, the load-displacement characteristics of cervical FSUs were investigated in each rotational and translational direction. Specimens of various spinal levels were tested in two conditions: in the intact state and in the “disc only” state, wherein the posterior ligamentous and bony elements were removed. In this case, testing in two specimen states allowed for insight into how structures such as the posterior elements contribute to the biomechanics of the cervical spine. While this study established some basic shear biomechanical properties of the cervical spine, the applied shear loads and displacements were very small – up to ~1 mm or 10-40 N in the intact state and up to ~1 mm or 4-16 N in the disc only state.

The third study on this topic was Shea *et al* (1991). In this study, the load-displacement characteristics of 3-vertebra cervical spine segments were investigated in anterior-posterior shear. In this study, specimens were loaded up to 150 N in the anterior and posterior directions, however results from this study were difficult to compare with other existing works such as Moroney *et al* (1988) due to the use of 3 vertebra segments. In using 3 vertebra segments the resulting anterior-posterior shear load-displacement curve became less linear (more flexion-extension rotation) at higher displacements due to the existence of two intervertebral disc joints. This study also did not investigate right-left lateral shear.

A final, collective limitation of each of these three studies is the lack of inclusion of realistic magnitudes of axial compression. In Moroney *et al* (1988) for example, 49 N of axial compression was applied to FSUs. This load magnitude corresponds to the mass of head that would be supported by the cervical spine (Moroney *et al*, 1988). In an *in vivo* situation, the true amount of axial compression experienced in the cervical spine is likely much greater due to the

existence of both passive and active muscle activation. In the case of trauma, large compressive forces might also exist resulting from headfirst impacts. Because the existence and magnitude of axial compressive loads might affect the behaviour of the cervical spine in shear, some exploration of this variable is needed.

### **1.2.5 Test Apparatus Design Challenges in Mechanical Testing of the Spine**

One of the most important considerations in performing mechanical testing in the spine is the design of any apparatus used to load cadaveric specimens. Because each spinal level has 6 degrees of freedom, and motions are typically coupled (ie. co-occurring) to some extent (Panjabi *et al*, 1986), test apparatus design may have a considerable influence on variables of interest such as kinematics, stiffness, ultimate failure loads and injury modes. Thus, careful consideration of alignment of applied loads, boundary conditions and existence of unintended (artefact) loading are essential in designing a testing apparatus. For example, it is common to use a counterbalance system to off-load the mass of non-anatomical components that would otherwise apply an artefact load to the spine (Nightingale *et al*, 2002; Goertzen *et al*, 2004).

The influence of design features is especially important when attempting to apply more complex loading, such as the addition of axial compression during shear (or other directional) loading. In the case of shear testing of the cervical spine, it is desirable to be able to apply a compressive load to a specimen as this mimics the *in vivo* loading that would typically be present in the cervical spine. Doing so presents a challenge as during increasing shear displacement, any axial load applied will begin to also apply some bending moment on the spine. This bending moment is somewhat inevitable, as even if the axial compressive force is perfectly aligned to the balance point in the initial stages of a test, this force will become increasingly eccentric relative to the shear centre as shear displacement occurs. If either the shear displacement (and resulting axial load eccentricity) or the magnitude of the axial load is

large enough, this bending moment may become the dominant feature of the test. This may be undesirable if the primary interest is to assess the shear properties of the spine.

In response to the potential issue of large bending rotations during shear testing, exacerbated by the inclusion of axial compression loads in the test methodology, different test apparatus design solutions have emerged. A number of studies investigating the shear biomechanics of the human lumbar and porcine cervical spine exist. Considering these studies, three primary shear test apparatus design categories (illustrated in Figure 1-8, studies described in Table 1-2) can be found:

- a) Point load method (rotationally unconstrained)
- b) Uniform displacement method (rotationally constrained)
- c) Follower load method (rotationally unconstrained)

Cripton *et al*, 2000

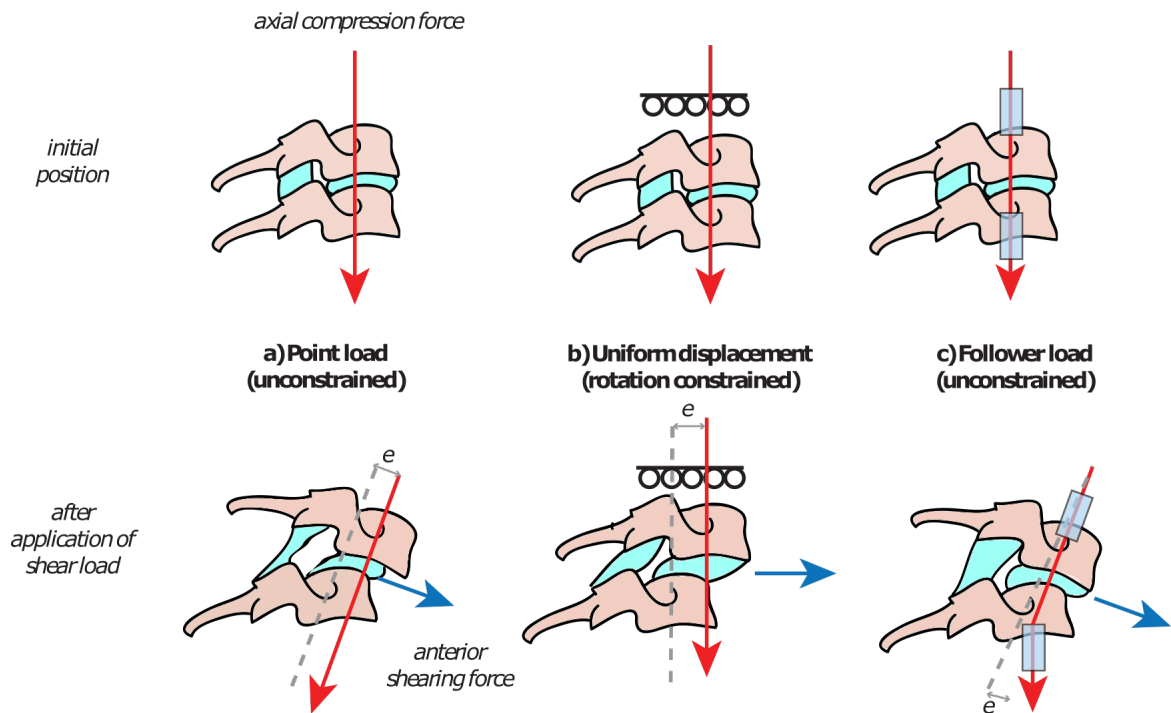


**Figure 1-8: Three Categories of Existing Shear Test Apparatus Design**

The point load method involves applying a compressive force at the kinematic centre (or “balance point”) of the specimen, without restriction of any degrees of freedom. During applied displacements, such as anterior shearing, the compressive force is body-fixed to the loading vertebra. While this design may be advantageous due to its relative simplicity, it may create large artefact bending moments if large displacements of the loading vertebra occur (Panjabi *et al*, 1977). Because rotation is not restricted, large rotations may occur with this method when large bending moments are present, which is undesirable.

The uniform displacement method involves restricting all rotational degrees of freedom, such that when a compressive force is applied, it is effectively a uniform superior-inferior displacement of the loading vertebra. Although this method would appear to reduce bending rotations that might be undesirable during shear testing, large bending moments must necessarily exist to enforce the no-rotation boundary condition on the specimen.

The follower load method involves the use of guides (eg. eyelet hooks, tubing) anchored near the intervertebral disc(s) to direct the line of action of the compressive force when a wire is used (Patwardhan *et al*, 2000 ; Miura *et al* 2002). In an FSU, this would involve two sets of paired guides anchored rigidly to the inferior and superior vertebra (or potting plates that these are secured to). This method may reduce artefact bending moments by keeping the line of action closer to the kinematic centre of the specimen (thereby reducing the eccentricity of the axial compression force). However, because in this method the compressive load is no longer body-fixed to the loading vertebra, an artefact shearing force will be created, where decreasing artefact moments comes at the cost of increased artefact shearing forces (Cripton *et al*, 2000). The balance between the two types of artefact loads is influenced primarily by the locations of the guides inferior to and superior to the intervertebral disc (Cripton *et al*, 2000).

Of these three methods, the point load and uniform displacement methods are the most commonly used in existing literature involving mechanical testing of the spine. While to the

author's knowledge no current studies have examined the shear biomechanics of the cervical spine with large (greater than 300 N) axial compressive loads, a number of studies of a similar nature have been performed using the human lumbar spine and porcine cervical spines at both the FSU and whole spine level. A summary of some relevant studies can be found in Table 1-2. Upon examining the results from these studies, it becomes apparent that the kinematics, load-displacement characteristics such as failure load and eventual failure mode diverge based on the axial compression method employed; point loads result in lower failure loads, large flexion rotations and, soft tissue failures, while the uniform displacement method results in increased failure loads and bony failures. This suggests that there are significant differences in applied loads between these two test apparatus design methods.

**Table 1-2: Comparison of some existing shear biomechanics studies according to test apparatus constraint type**

Apparatus Constraint	Axial load	Specimen type	Failure load & mode	Kinematics
<b>No constraint</b>				
• Begeman <i>et al</i> , 1994	0 N	Lumbar FSUs	1291 N, dislocations & ligament rupture	14.5 ° flexion, 8.5 mm ant shear
• Berkson <i>et al</i> , 1979	400 N	Lumbar FSUs	Non-destructive (145 N)	2 ° flexion
• Melnyk <i>et al</i> , 2015	300 N	Lumbar FSUs	Non-destructive (250 N)	<1 ° flexion, 0.4-1.6 mm ant shear
<b>FE rotation constrained</b>				
• Begeman <i>et al</i> , 1994	0 N	Lumbar FSUs	2776 N, facet fx	12.1 mm ant shear
• Skrzypiec <i>et al</i> , 2012	500 N	Lumbar FSUs	3290 N, disc failure, fx	13.1 mm ant shear
• Gallagher <i>et al</i> , 2010	1600 N	Porcine cervical FSUs	2310-2767 N, pars interarticularis, endplate fx	Not reported
• Yingling & McGill, 1999	300 N	Porcine cervical FSUs	1980 N, pars interarticularis fx	9.7 mm ant shear

To date, only one study exists in which the effect of how different means of application of axial compression exists. In study by Cripton *et al* (2000), a mathematical model based on a free body diagram of different variations of the point load and the follower load was established, and verified against an experimental study involving human lumbar FSUs. While this study provides some indication of how each method may affect artefact loading in the specimen, the mathematical model and subsequent verification study were based on artefact loading resulting from flexion-extension rotations. In shear testing, where some amount of shear translation and/or some amount of flexion-extension rotation may occur, the specific predictions from the mathematical model may no longer be valid. As well, in this study, the uniform displacement compression method was also not considered in the analysis. Thus, there is some need for investigation of how all of the outlined axial compression methods affect artefact loading of the spine during the specific case of the application of shearing loads.

Because of these differences in mechanical testing results and incomplete understanding of why these different results might be occurring, it is unclear how these results should be interpreted or applied in areas such as FE modeling. Ideally, one would aim to select the axial compression method that is most clinically relevant from an injury mechanism perspective, however due to limitations in our understanding of the loading and boundary conditions involved at the vertebral level in injuries such as the BFD, it is not possible to say with certainty which (if any) method is most clinically relevant. It would however, be useful to understand how different apparatus design features influence specimen loading during mechanical testing in order to facilitate more informed experimental design, so that mechanical testing results can be more readily translated to injury models for future injury mechanism elucidation.

### 1.3 Research Objectives

Based on the deficits that exist within the current body of literature and the industry standards based upon them, the following research objectives were developed:

1. Determine the load-displacement behaviour of the human cervical FSU during non-destructive shear loading
  - a. Shear stiffness and 3D kinematics in the anterior, posterior and lateral shear directions
  - b. Effect of progressive removal of the posterior ligaments and bony elements on the shear stiffness and 3D kinematics
2. Determine the effect of three axial compression methods on specimen artefact loading (forces and moments) during shear testing
  - a. Artefact moments and coupled rotations in an FSU with different axial compression methods
  - b. Determine effect of placement of follower load guides on FSU artefact loading and coupled rotations

Chapter 2 will address the first research objective, while Chapters 3 and 4 will address the second research objective. Chapter 3 will detail the results from the multibody dynamics simulations, Chapter 4 will detail the experimental verification results.

## **2 Load-displacement characteristics of human cervical FSUs during shear loading<sup>1</sup>**

### **2.1 Purpose**

As compared to other loading modes, the biomechanical properties during shear loading are not well-established in the cervical spine. To date, only three studies (detailed in Section 1.2.4) exist that have investigated these properties. Limitations with the existing studies include low magnitude of shear loading (Panjabi *et al*, 1986; Moroney *et al*, 1988), limited variety of directional testing (Shea *et al*, 1991), as well as difficulty in direct comparison between studies due to experimental differences such as specimen preparation. Because of these limitations and the small number of existing studies, the biomechanics of the cervical spine during shear loads and displacements are not considered in current safety standards, despite evidence that severe injuries such as BFD may occur as a result of these modes (Ivancic *et al*, 2008).

The aim of the present study was to investigate the load-displacement characteristics of the human cervical FSU during the application of non-destructive shear loads. Parameters of interest included the FSU shear stiffness and 3D kinematics during anterior, posterior and lateral shear loading. These parameters will be evaluated in three specimen conditions involving progressive damage to the posterior elements, in order to determine how these structures influence the biomechanics during shear loading in each direction.

### **2.2 Methods**

#### **2.2.1 Specimen Preparation**

Eight human cadaveric FSUs were subjected to the shear testing protocol. Individual FSUs were dissected from fresh-frozen whole cervical spines. Prior to dissection, donors' medical records were screened for histories of spine surgery, spine trauma, head/neck cancer and other

---

<sup>1</sup> A version of this chapter will be submitted for publication. "Shear Stiffness and Kinematics in the Lower Cervical Spine" Dowling-Medley JJ, Doodkorte RJ, Melnyk AD, Cripton PA, Oxland TR

pathologies affecting the mechanics of the spine. Lateral and frontal radiographs of the donor cervical spines were also examined for the presence of major bony abnormalities.

Seven C6-C7 FSUs and one C2-C3 FSU were selected for testing from seven donors (Table 2-1). The median age of the donors was 53 years. Following dissection, specimens were frozen at -20 °C until use.

**Table 2-1: Specimen and donor information**

<b>Donor ID</b>	<b>Level</b>	<b>Sex</b>	<b>Age</b>	<b>Notes</b>
<b>H1412</b>	C6-C7	M	55	
<b>H1418</b>	C6-C7	M	53	
<b>H1410</b>	C2-C3	M	54	omitted: potting error
<b>H1421</b>	C6-C7	F	29	omitted: soft tissue failure
<b>H1419</b>	C6-C7	F	50	
<b>H1410</b>	C6-C7	M	54	
<b>H1415</b>	C6-C7	F	64	partially omitted: missing data
<b>H1423</b>	C6-C7	M	50	omitted: suspected fusion

Specimens were fixed rigidly in cylindrical polymethylmethacrylate (PMMA) (Keystone Industries, Gibbstown, NJ, USA) potting cups. Four wood screws were inserted into each endplate and paired facet and wire gauge was wrapped around the screws prior to fixation to prevent pullout during testing (Figure 2-1). Specimens were fixed such that the intervertebral disc was aligned parallel to the flat surface of the potting cups in the transverse plane. This was achieved by visual inspection of the superior-most endplate with a laser level (Figure 2-2). Sagittal plane radiographs of the potted specimen were taken to assess the suitability of the alignment of the intervertebral disc. One specimen (H1410, C2-C3) was omitted due to poor alignment of the intervertebral disc.

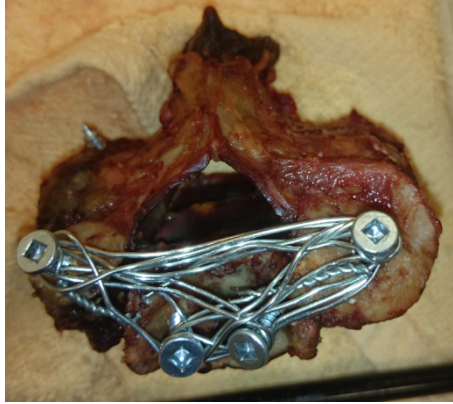


**Figure 2-1: Specimen Preparation with Wood Screws and Wire Gauge**

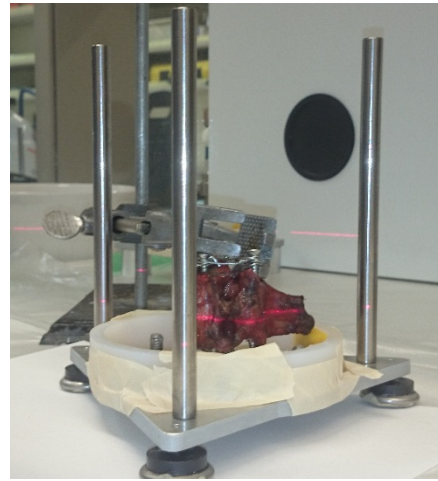


**Figure 2-2: Alignment of Specimen in Potting Rig**

Of the eight specimens tested, three were excluded from the results due to experimental errors, as described in Table 2-1. Specimen H1421 was noted to be very unstable and experienced a soft tissue failure during testing. While unequivocal bony abnormalities were not noted on specimen H1423's pre-testing radiographic images, it is suspected that this specimen had some degree of bony fusion due to near-zero displacements observed during the application of shear loads.

Specimen H1415 followed a modified experimental protocol in which it did not undergo all testing runs, and was thus excluded from certain analyses. This will be explained in further detail in the following section, as well as in the discussion (Section 2.4).

## **2.2.2 Apparatus Design & Load Application**

Shear loads were applied to each FSU via a custom-designed apparatus (Figure 2-3, Figure 2-4) interfaced with an ElectroPuls E1000 Instron materials testing machine (Instron, Norwood, MA). The inferior vertebra of the FSU was fixed while the shear load was applied through the superior vertebra, where the location of force application was aligned to the centre of

the disc. The sensitivity of this alignment to small (~0.5mm) deviations was assessed post-test. A counterbalance system off-loaded the mass of all hanging components that would otherwise impart artefact loads or moments on the specimen (loading plate, superior PMMA potting, fasteners, superior half of the mass of the cadaveric specimen). This ensured that at 0 mm or 0 N shear, that the specimen was unloaded, and resting in a neutral posture (~0 ° flexion-extension).

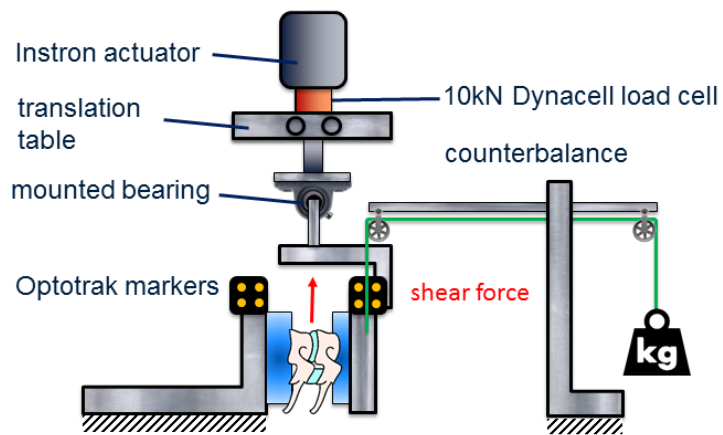


**Figure 2-3: Shear Test Apparatus - Anterior-Posterior Test Configuration**

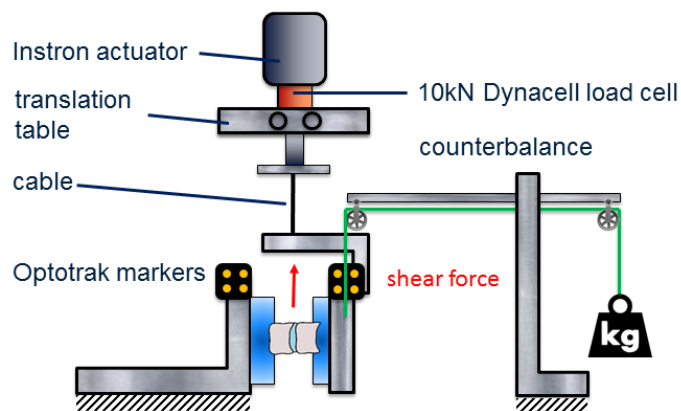


**Figure 2-4 Shear Test Apparatus - Lateral Shear Test Configuration**

Specimens were tested in two cyclic loading regimes. A quasi-static load rate of 15 N/s was used for all tests. During anterior-posterior loading, the specimen was loaded to 100 N in each direction during one continuous loading cycle. For these tests the loading plate of the specimen was connected rigidly to the Instron actuator through a planar translation table and a mounted bearing, allowing for testing in both shearing directions in a single cycle (Figure 2-3). In this configuration, the superior (loading) vertebra was constrained in axial rotation and lateral bending, but allowed all other degrees of freedom.

During right lateral loading, the specimen was rotated in the apparatus and loaded between 20 N and 100 N in the right direction only (Figure 2-4). For these tests, the mounted bearing was replaced by a cable, giving the superior (loading) vertebra 5 degrees of freedom, with the lateral translation prescribed. The different loading regimes were established through pilot testing, where it was found that additional constraints in the lateral direction imposed restrictions on the specimens' motion, but that such effects were minimal during anterior-posterior loading, and that allowing only flexion-extension was appropriate.

The advantage to using a solid beam element such as a mounted bearing is that the specimen may be both "pulled" and "pushed," thus allowing for both anterior and posterior displacement during a single loading cycle. This in turn allows for characteristics near 0 N anterior and posterior displacement to be assessed, which is not possible when a cable is used to apply the shearing force, as some tension must exist in the cable to ensure repeatable loading cycles.

Specimens were tested in the anterior-posterior and lateral loading cycles first in the intact state, then with the posterior ligaments (supraspinous, interspinous, ligamentum flavum, intertransverse) and facet capsule severed using a scalpel, then with the bony posterior elements (spinous processes, laminae, articular processes, transverse processes, pedicles) removed with surgical rongeurs. These are described as the intact, ligaments cut (Figure 2-5) and disc-only conditions (Figure 2-6).

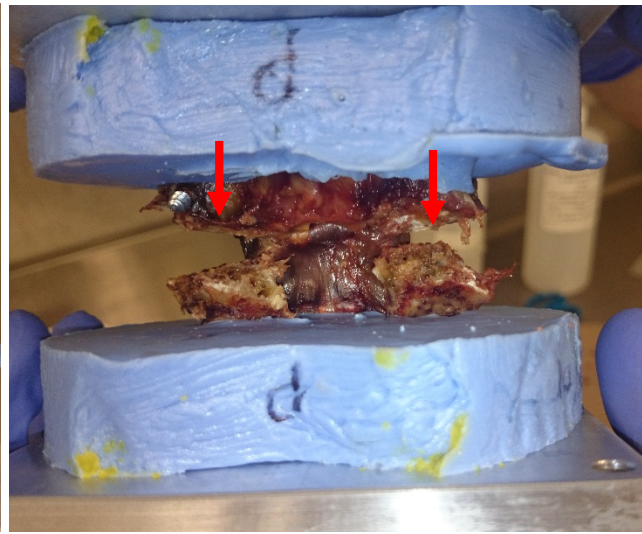
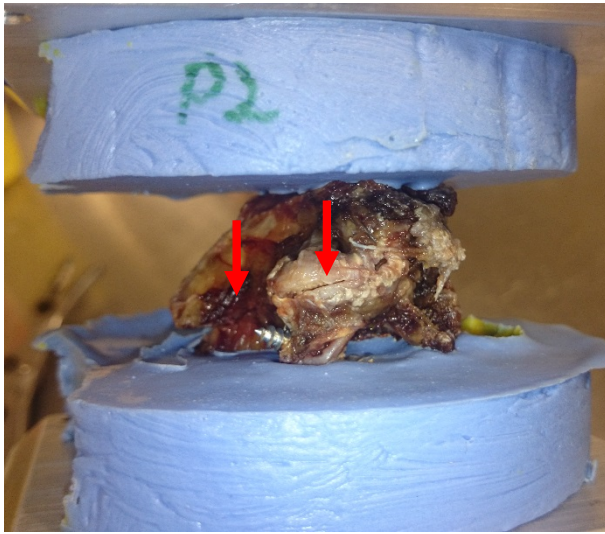


**Figure 2-5: Lateral View of the Ligaments Cut Condition (red arrows show location of cut)**      **Figure 2-6: Posterior View of the Disc-Only Condition (red arrows show removed posterior elements)**

In the case of specimen H1415, the cable was used for anterior-posterior tests in the ligaments severed and disc-only conditions. This meant that load-displacement characteristics could only be assessed between 20-100 N for these test runs. This modification was made during testing due to observed instability in this specimen after the severing of the posterior ligaments.

### 2.2.3 Data Collection and Analysis

Load was captured using an inline 10 kN DynaCell load cell (Instron) and data was collected via the Optotrak ODAU (Northern Digital Inc., Waterloo, ON, Canada) analogue input, which allowed the load data to be synchronized with the kinematics data. The maximum error for the loading cycle was less than  $\pm 3.0$  N. The load cell and motion capture data were synchronized and collected at 50 Hz. A zero-lag low-pass 4<sup>th</sup> order Butterworth filter with a cut-off frequency of 1 Hz was applied to both the kinematic and load data.

Three-dimensional kinematics were collected using a motion capture system (Optotrak Certus, Northern Digital Inc.). Four-marker rigid body plates were fixed to the inferior and superior

potting plates to measure relative motion between the two vertebral bodies on either side of the intervertebral disc (Figure 2-7).

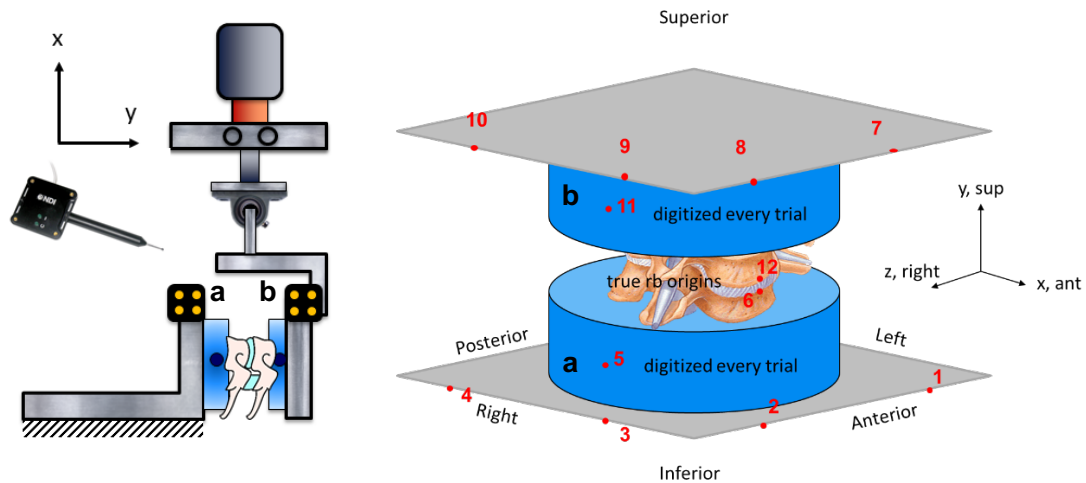


**Figure 2-7: Anatomical Coordinate System Definition and Alignment Relative to Apparatus-Mounted Rigid Body Markers**

Kinematics were transformed from the Optotrak global coordinate system to the anatomical coordinate system. The anatomical coordinate system and rigid body origins were defined with digitized landmarks on the specimen (Figure 2-7). The anatomical coordinate system was defined as follows:  $x$  – positive anterior,  $y$  – positive superior and  $z$  – positive to the right. The origins for the inferior and superior rigid bodies were located at the mediolateral centre of the anterior aspect of the FSU on the inferior to and superior to the intervertebral disc (points 6 and 12 in Figure 2-7). The 12-point digitization of the potted specimen (Figure 2-7, right) was done at the start of the test day to define the coordinate systems for the superior vertebra and inferior vertebra (both the anatomical axes and the origins) relative to two easily accessed digitization landmarks on the superior and inferior PMMA potting (points a & b in Figure 2-7). Prior to the initiation of each test, a 2-point digitization (points a & b) and a 5 second static shot of the Optotrak

markers was performed. This, along with a 4-point digitization of two perpendicular test apparatus frame components aligned to the anatomical coordinate system, enabled for a transformation of the Optotrak marker position data for each vertebra into the anatomical coordinate system. A complete description of the kinematics algorithm used may be found in Appendix B.

Displacements were expressed according to the anatomical axes of the specimen while flexion-extension, axial rotation and lateral bending rotations were expressed as Euler angles about the anatomical axes of the specimen in order z, y, x. Displacements were considered as the difference between the position of the specimen at 100 N of applied shear load and the position at 0 N (anterior and posterior shear) or 20 N (lateral shear) during the third cycle, while rotations were considered in absolute terms.

Stiffness was determined from the load-displacement curve of the third loading cycle for each respective direction. Stiffness was calculated as the slope of the line of best fit between two load ranges: 0-20 N and 20-100 N. Thus, in the anterior and posterior directions two stiffness values are reported, while in the lateral direction only one is reported (specimen not loaded between 0-20 N laterally). This method was established from the assessment all load-displacement curves, where the two-segment stiffness method provided the best representation of the behaviour through all specimen conditions and directions. Load-displacement curves for all specimens in each direction and all load and displacement data were analyzed in Matlab (MathWorks, Natick, MA, USA).

A Friedman's test with a one-tailed Wilcoxon post-hoc ( $\alpha=0.05$ ) was used to assess the significance of any decreases in stiffness between progressive specimen conditions. Statistical analyses were performed in R (R Foundation, Vienna, Austria). As a result of specimen H1415's partial omission from some tests, statistical significance could not be assessed for certain pairwise comparisons as a minimum of 5 paired samples is required for this statistical test.

## 2.3 Results

### 2.3.1 Stiffness

#### *Anterior stiffness*

A significant decrease in stiffness [range] was found in the anterior direction from 186 N/mm [98-327 N/mm] in the intact condition and 105 N/mm [78-142 N/mm] in the disc-only condition in the 20-100 N range ( $p=0.03$ ). While no other significant differences were found between the two stiffness ranges, specimens tended to exhibit lower stiffness in the 0-20 N range, ranging from 100 N/mm [32-205 N/mm CI] to 49 N/mm [30-120 N/mm CI] between in intact and disc-only conditions. However, all four pairs where a comparison was possible exhibited a decrease in stiffness from the intact to disc-only state. The decreasing trend in the 0-20 N stiffness between progressive injury conditions could not be assessed as only four paired results existed for this range. Mean stiffness values and ranges for each specimen condition in each direction may be found in Figure 2-8.

#### *Posterior stiffness*

A significant decrease in stiffness was found in the posterior direction from 134 N/mm [92-182 N/mm] in the intact condition to 119 N/mm [83-181 N/mm] ( $p=0.03$ ) in the disc-only condition. Again, no significant differences were found between the two stiffness ranges, but specimens tended to be less stiff in the lower 0-20 N range across all condition ranging from 61 N/mm [21-137 N/mm] to 54N/mm [12-101 N/mm]. The effect of injury condition on the initial stiffness was less pronounced, where three specimens saw small decreases in stiffness and one saw a slight increase in stiffness.

## Lateral stiffness

No significant decrease in stiffness was found in the lateral direction between injury conditions. While there was a slight decrease in the mean stiffness from the intact condition to the disc-only condition from 233 N/mm [124-408 N/mm] to 208 N/mm [115-296 N/mm], three specimens saw some decrease in stiffness, while two saw slight increases in stiffness. Pooling all lateral stiffness values gives a mean stiffness of 214 N/mm [137-291 N/mm] for all injury conditions.

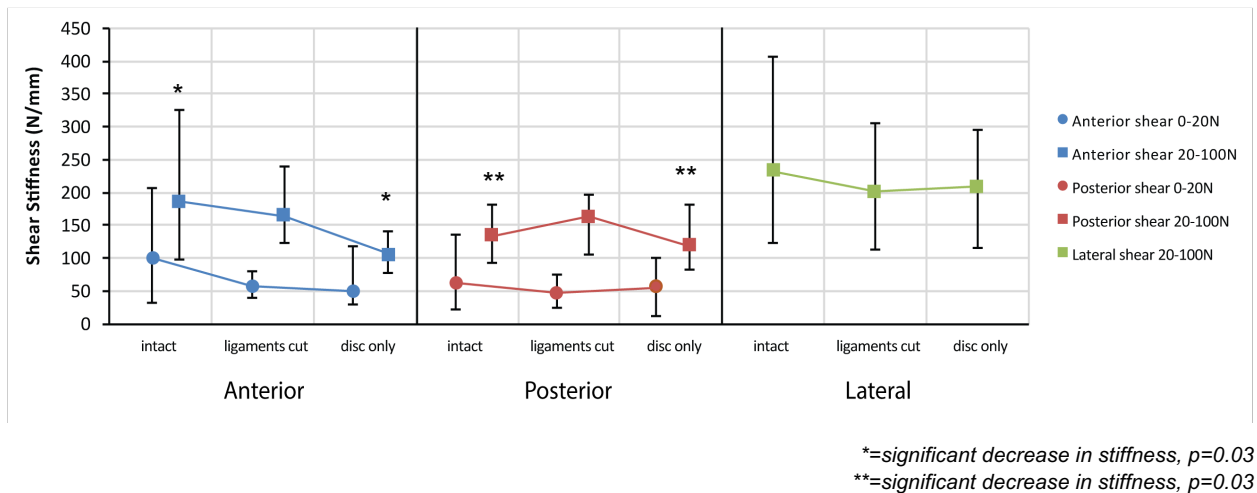


**Figure 2-8: Mean stiffness and range of the cervical FSU during shear loading**

## 2.3.2 Kinematics

### Displacements

No significant increase in displacement was found between injury conditions for each respective shearing direction. In the anterior and posterior directions, there was a trend towards increasing displacements from the intact to disc-only conditions, but the significance of this result could not be assessed due to an insufficient number of comparable results. In the anterior direction, displacements ranged from 0.84 mm [0.34-1.37 mm] for the intact condition to 1.40 mm [0.78-1.87 mm] for the disc-only condition. In the posterior direction, displacements ranged from 1.07 mm [0.58-1.61 mm] to 1.37 mm [0.75-2.52 mm] between the intact and disc-only conditions.

In the lateral direction there was no clear trend in displacement with injury condition. The mean displacement for all injury conditions was found to be 0.43 mm [0.32-0.52 mm]. Coupled displacements in the non-shearing directions were less than 1 mm in all tests. Time traces for each individual specimen in the intact condition may be shown in Figure 2-9 (anterior-posterior) and Figure 2-10 (lateral).

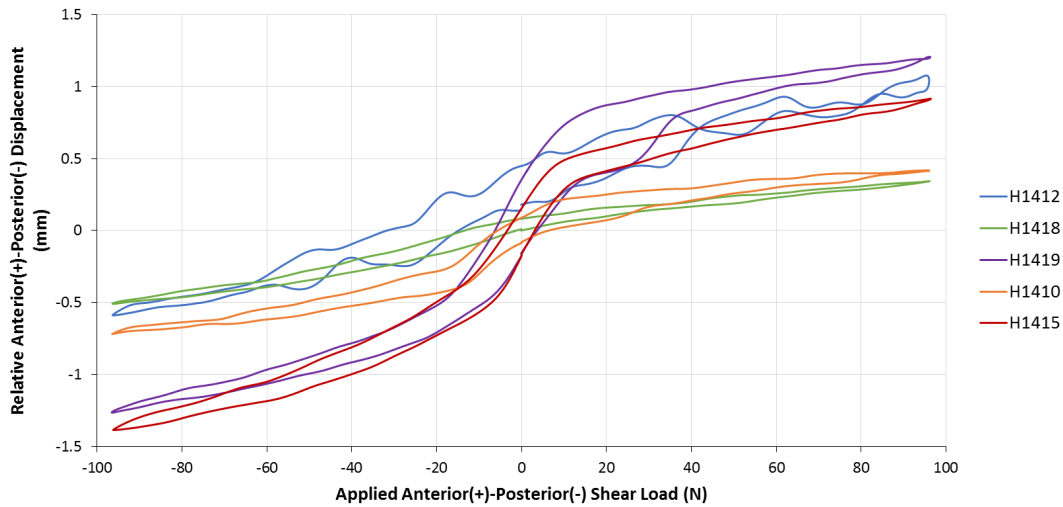


**Figure 2-9: Anterior-posterior loading cycle for each specimen in the intact condition**

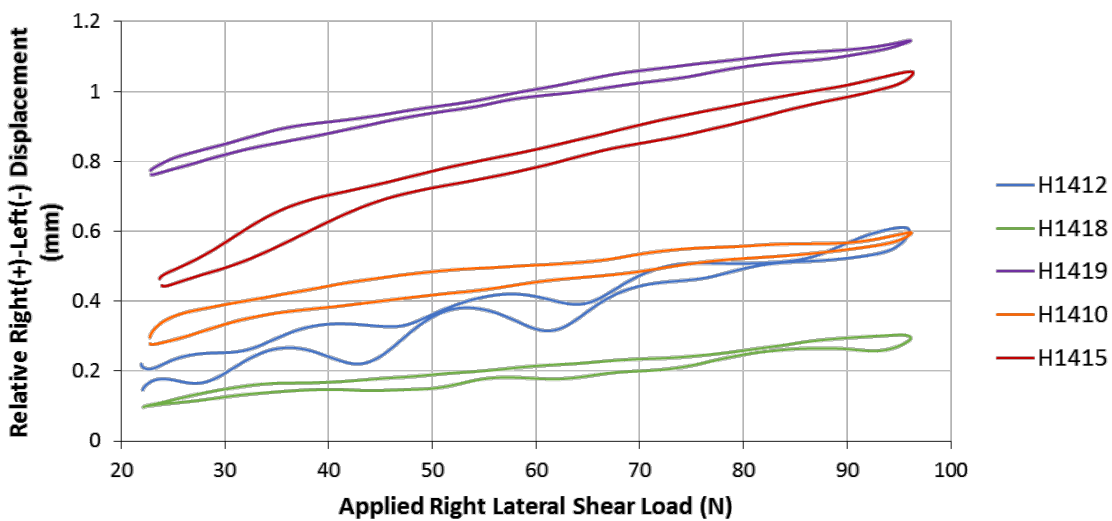


**Figure 2-10: Right lateral loading cycle for each specimen in the intact condition**

### *Rotations*

Coupled rotations were minimal up to 100 N except in specimen H1419 during posterior shear in the disc-only state. During anterior-posterior tests, axial rotation and lateral bending were constrained by the test apparatus, while during lateral tests, no rotational constraints existed.

Considering all anterior and posterior tests performed (n=14), the majority (n=11) fell between 1.1° flexion and 0.5° extension corridor through a continuous anterior-posterior cycle, with no clear trend with regard to flexion or extension being associated with either anterior or posterior shear. Three specimens experienced larger ranges of motion in flexion-extension, all with extension angles during posterior shear in their disc-only and ligaments severed conditions (between 0.9-2.1°). Specimen H1419 experienced considerable flexion during posterior shear in the disc-only condition, reaching a maximum of 11° flexion at 48.5 N of posterior shear.

In the lateral direction, all coupled rotations existed were less than 1.5°, excepting specimen H1415 in the disc-only state. This specimen experienced a maximum of 2.9° flexion during this test.

## **2.4 Discussion**

In the present study, the load-displacement behaviour of cervical FSUs was assessed in each shearing direction, at higher loads that had not previously been assessed. It was expected that shear stiffness would decrease with increasing damage to the posterior elements, particularly in the anterior direction. This result was expected as the posterior elements and ligaments, namely the facet joints, tend to be oriented such that they could restrict translation, or impart a coupled flexion rotation, during the application of anterior shear loads. A significant decrease in shear stiffness between the intact and disc-only conditions in the posterior direction was also found, but this difference was less pronounced (81 N/mm mean decrease anteriorly between the intact and disc-only conditions vs. 15 N/mm decrease posteriorly between the intact and disc-only

conditions). It is speculated that this might be explained by the approximately 45 ° orientation of the facet joints in the cervical spine, which would tend to restrict anterior translation more substantially than posterior translation in an intact specimen. This would indicate that in the anterior direction, the posterior elements contribute to ~50% of the shear stiffness in the anterior direction, but have a more modest effect in the posterior direction. This insight suggests that more detailed, direction-specific modeling of the cervical FSU may be necessary to capture its intact response.

This effect is further demonstrated by comparing the anterior stiffness values to the posterior stiffness values in each specimen condition in the 20-100 N range. In the intact state, the mean stiffness was greater in the anterior direction than in the posterior direction by 52 N/mm (non-significant result), but the stiffness values begin to converge with progressive injury to the posterior elements, where the stiffness values are similar in the disc-only state. This suggests that the load-response behaviour of the disc itself may be similar in the anterior-posterior direction up to 100 N. Anatomically, the cervical disc is not symmetrical in the anterior-posterior axis (Mercer & Bogduk, 1999), and one might expect that this would be reflected in its biomechanical properties. However, it is possible that such differences may not be apparent at the loads used in the present study.

While differences between the intact to ligaments severed and ligaments severed to disc-only conditions did not reach significance for any pairwise comparison over any load range, the stiffness values for the ligaments severed condition tended to be closer to the intact state in the 20-100N range. In the 0-20N range, differences were less pronounced between all injury states, but the ligaments severed 0-20N stiffness tended to more similar to the disc-only state. This might indicate that the bony posterior elements have a greater contribution to the mechanics of the cervical FSU at more extreme anterior and posterior shear loads (possibly due to bony contact at these loads), whereas the posterior ligaments contribute more to the mechanics during very small

shear loads and displacements. Interestingly, the effect of severing the posterior ligaments was somewhat varied on an individual specimen basis. In the 20-100 N load range, some specimens experienced an increase in stiffness (n=2, 40%) in the anterior direction. In the posterior direction over the same range, some specimens also experienced an increase in stiffness from the intact to ligaments cut condition (n=3, 75%). It is possible that this unexpected result occurred due to changes in the facet joint space post-ligamectomy, where increased bony contacts might have occurred in some specimens. That this did not occur in all specimens may speak to the variability between subjects, specifically in the geometry of the ligamentous and bony posterior elements (where variability in stiffness was reduced in the disc-only state).

Based on the work of Panjabi *et al* (1986), where approximately linear load-displacement behaviour was noted in shear up to 50 N, it was presumed that the present investigation would yield a single stiffness value. However, it was found that in some specimens, a neutral zone typically seen in flexion-extension loading existed between approximately 0-20 N, regardless of injury condition (Figure 2-9). Thus, two stiffness values were computed for all specimen in order to represent the load-displacement behavior appropriately. This result (existence of a neutral zone during application of shearing loads) may reflect the non-linear load response that would be expected of the isolated ligamentous tissue in the FSU.

In the lateral direction, there were no significant differences in stiffness with progressive damage to the posterior elements. In this direction, the mean stiffness was greater than both the anterior and posterior directions in all injury conditions. This result was also true within each specimen, where stiffness was always greatest in the lateral direction. These results are reasonable as the geometry of the posterior elements does not provide much constraint against lateral translation, so their removal could be expected to have a less pronounced effect. It is speculated that in the lateral direction, the paired curved uncovertebral joints, which lie lateral to

the disc centre would tend to impede lateral translation. In the present experiment, these structures were left intact.

The reported stiffness values were within the scatter of those found in other similar investigations, as shown in Figure 2-11. In Panjabi *et al* (1986), intact cervical FSUs were loaded in the anterior, posterior and lateral shear directions up to 50 N, with the linear stiffness evaluated at 25 N. In this study, the mean stiffness was determined to be 33.8 N/mm, 52.6 N/mm and 52.6 N/mm for the anterior, posterior and lateral shear directions respectively. These values reported by Panjabi *et al* are somewhat lower than the mean values determined in the present study for the 0-20 N range, but are still within the ranges determined in the present study.

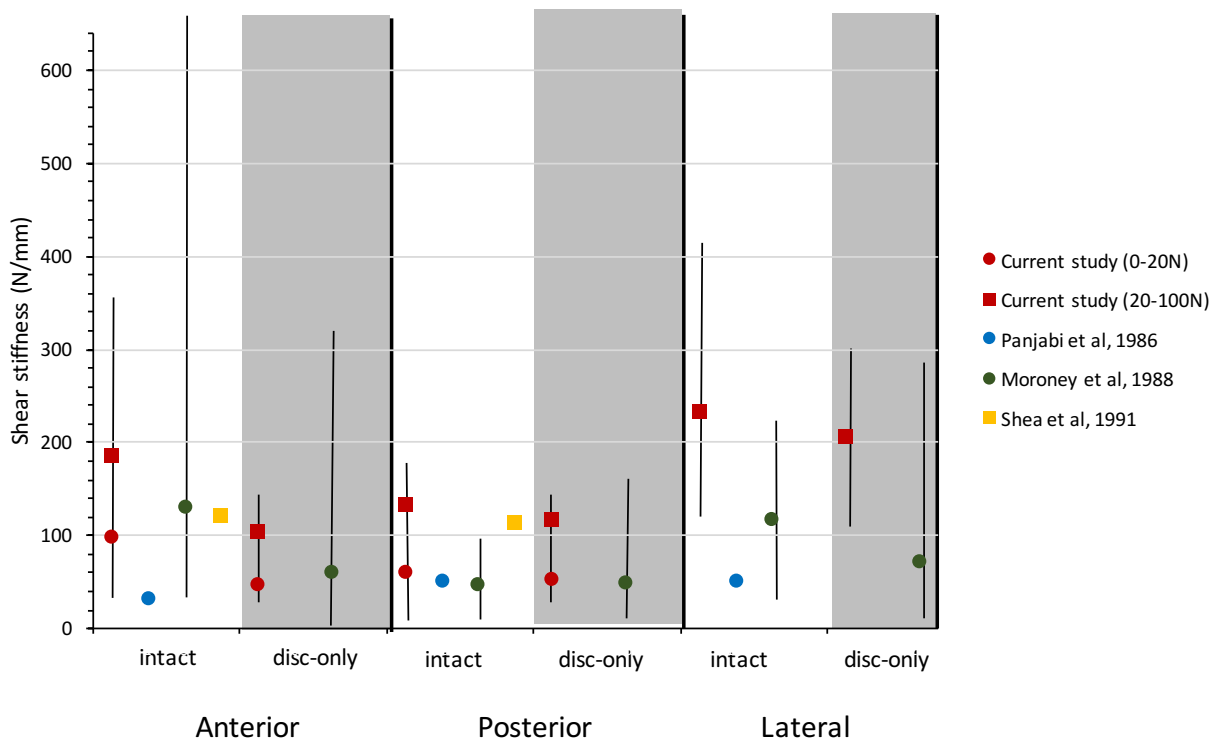


**Figure 2-11: Comparison of shear stiffness results from present work to previous works**

In Moroney *et al* (1988), cervical FSUs were tested in the intact and disc-only state in anterior, posterior and lateral shear to ~1mm displacement (10-39N for intact specimens, 4-16N

for disc-only specimens). Considering the lower loading regime protocol used in the Moroney study, which is more comparable with the 0-20N stiffness in the present study, good agreement can be observed. Greater variability is seen in the Moroney study, as demonstrated by the ranges plotted in Figure 2-11. This is likely because in the present study all specimens included in the final results were C6-C7 FSUs, where Moroney's results include all lower cervical spine FSU levels.

In Shea *et al* (1991), a similar study was undertaken, where intact 3-vertebra cervical spine segments were loaded to 150 N in the anterior and posterior directions. The anterior stiffness was found to be 123 N/mm ( $\pm 0.35$  SD) and the posterior stiffness was found to be 114 N/mm ( $\pm 0.69$  SD) at 100 N. The mean values also correspond well with the intact stiffness values reported in this study in the 20-100 N range.

The primary limitation of the present study was the small sample size. Having a greater sample size would have allowed subject-specific intrinsic factors to be accounted for in the data analysis. In accounting for factors such as disc and facet degeneration, gender, age, and bone mineral density, the apparent variability between specimens might have been reduced and further insight into factors affecting the shear biomechanics might have been gained. Accounting for such factors would also be useful for those developing FE models, who might use subject-specific characteristics to tailor their models to better capture at-risk populations.

A second limitation was the design of the test apparatus. Originally, two levels of axial compression were to be applied to the specimens to recreate a more physiological loading scenario in which to assess the shear biomechanics. *In vivo*, the mass of the head and muscles activation result in some varying amount of compressive force along the cervical spine. This aspect of the experimental protocol proved to be problematic, resulting in many unanticipated catastrophic and sub-catastrophic failures in flexion-extension, especially in the ligaments cut and disc-only conditions. As a result, the variable of axial compression was removed from the present

protocol. Even with removal of axial compression, there still remained some issues during testing in which large flexion-extension angles were observed. These specimens and trials were removed from the present analysis.

It is suspected that this issue arises from the size of the balance point in the cervical spine, where this sensitivity to alignment is more critical in some specimens. Based on challenges experienced with the cervical spine, it is speculated that the balance point is smaller (owing perhaps to the smaller overall size of the cervical spine) as compared to the other spine regions, such as the lumbar spine. A similar apparatus was used previously in our lab to load lumbar FSUs in anterior shear with varying levels of axial compression and instability (large coupled rotation) was not observed in male or female specimens until the nucleus of the disc was removed (Melnik *et al*, 2015). This might suggest that further analysis of apparatus design and its effect on specimen loading is necessary if smaller, more unstable specimens are to be tested in a repeatable manner.

It is also possible that the bearing used during the anterior-posterior cyclic testing may have been a limitation of the apparatus design, where the constraints it imposed (no lateral bending, no axial rotation) may have affected some specimens. Though in pilot testing it was found that the effects of these constraints were minimal, some of the more flexible specimens (eg. H1415) tested during the present study may have been more sensitive to this.

In conclusion, this study determined the load-displacement characteristics of five C6-C7 cervical spine FSUs during non-destructive shear loading. It was found that the removal of the posterior elements resulted in a significant decrease in the anterior-posterior shear stiffness, but caused no significant decrease in the lateral shear stiffness nor in the initial (0-20N) stiffness in any direction.

The primary application of these findings is for implementation in mechanical and computational modeling of the cervical spine. By implementing direction-specific load-

displacement behaviour of the cervical FSU, biofidelity of existing models might be improved. Though the loads and displacements evaluated herein were non-injurious, information about the behaviour of the cervical spine during the initial stages of shear loading may be important for ensuring that the kinematics leading up to more injurious loads are biofidelic. Thus, establishing the shear behaviour at lower loads may be important for improving injury models. Similarly, the determination of the effect of the posterior structures may be of use for ensuring that the contribution of these FSU structures to the overall behaviour in the intact state is biofidelic.

## 3 Analysis of Shear Test Apparatus Design

### 3.1 Purpose

Axial compression during *ex vivo* mechanical testing of the spine is a desirable experimental feature as it improves the biofidelity of such testing. *In vivo*, the cervical spine experiences some amount of axial compression from the mass of the head, and some additional compressive forces from muscle activation. During anterior shear loading in particular, the inclusion of axial compressive forces may affect the load-displacement characteristics of the cervical spine. This consideration is especially pertinent for the application of injury tolerance in the automotive industry, as axial compressive forces from bracing or head impacts with the roof during a MVA could be substantial (hundreds-thousands of N).

As per the mathematical model developed by Cripton *et al* (2000), one of the challenges associated with applying axial compressive loads to the spine is the creation of artefact loads. Artefact loading is undesirable as these loads may result in altered kinematic behaviour, and/or add complexity to data analysis.

If displacements or rotations occur during testing, some eccentricity will be introduced, resulting in the creation of an artefact moment. Using more sophisticated designs such as follower load method (use of guides that direct the compression force line of action closer to the balance point) can reduce artefact moments, but at the cost of creating artefact shearing loads (Cripton *et al*, 2000). These effects are predicted by the model to increase proportionally with increasing axial compressive loads. Thus, applying realistically large axial compressive loads to cervical FSUs during anterior shear testing with minimal artefact loading represents a design challenge.

In previous work by Doodkorte *et al* (2016), a point load axial compressive method was used to apply compressive loads up to 325N during non-destructive anterior shear testing (Figure 3-1). Catastrophic soft tissue failures in flexion-extension occurred in a number of

specimens during tests involving the application of 325N of axial compression. The work presented in Chapter 2 of this thesis utilized a similar experimental set-up, but eliminated the variable of axial compression from the methods.

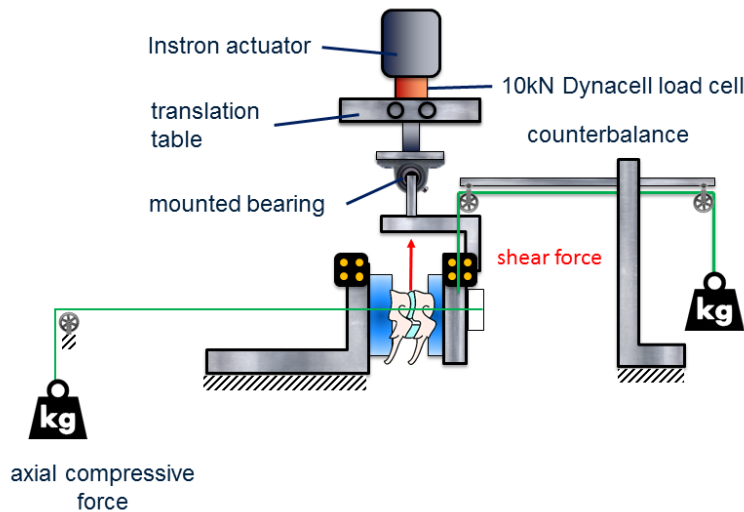


**Figure 3-1: Shear test apparatus with point load axial compression**

Despite elimination of the variable of axial compression from the study design, unintended specimen failures in flexion-extension still occurred in some of the more flexible or smaller specimens during shear testing (as described in Chapter 2). Following this, a number of experimental features were identified that might potentially be contributing to this undesirable flexion-extension behaviour in some specimens. The following were identified as potential sources of flexion-extension during the application of what was intended to be a pure shear load:

- a) Artefact flexion-extension moment from axial compressive force
- b) Misalignment of Instron actuator relative to the specimen shear centre
- c) Misalignment of specimen in potting
- d) Variability in ideal counterbalance mass and ideal position of application point
- e) Irregular specimen endplate and facet geometry

Of these features, items b) and c) were addressed through more thorough experimental methods; post-test sensitivity to small (~0.5mm) deviations in Instron alignment were assessed, while use of a laser level, external marking of landmarks with paint and post-potting radiographs were used to improve potting alignment.

In the case of issues with the counterbalance accuracy (item d) there is some variability in the true mass and centre of mass of the components that must be off-loaded by the counterbalance during testing. While the mechanical components have a constant mass and centre of mass, each specimen and the PMMA pots into which it is embedded introduce some variability into the determination of the mass and centre of mass of that which must be offloaded. If the true mass or centre of mass of these components is different from the estimated mass or centre of mass, some artefact loading will occur. It was found however, that the magnitude of error required to cause substantial artefact loading was unlikely to occur outside of substantial methodological error (Appendix D).

Item a) was identified as being a problem that might be addressed through improved test apparatus design. In the case of artefact loading from axial compression, a literature review (Chapter 1.2.5) was conducted to identify existing methods used to apply compression loads to cadaveric spine specimens. Three methods were identified: the point load with free flexion-extension rotation, the point load with constrained flexion-extension rotation and the follower load method. Because there is no consensus in the literature as to which method is standard, and the method selected could have a substantial effect on the kinematics, failure load and failure mode of the specimen, quantification of each method is desired to facilitate design decision-making.

From these considerations, two research questions were identified:

1. What artefact moments and coupled rotations occur in an FSU with different axial compression methods (point load, rotationally constrained, follower load)?
2. What is the effect of placement of follower load guides on FSU artefact loading (both moments and forces) and coupled rotations?

Because these questions involved more complex interactions between variables of interest, a multibody dynamics software (ADAMS, MSC Software Corp., Newport Beach, CA, USA) model was used to examine these questions. A multibody dynamics model of the test apparatus allowed for a large number of scenarios to be analyzed quickly, and eliminated the variability introduced by cadaveric specimens. A mathematical model (Crompton *et al*, 2000) was also used as a point of comparison for these questions.

### **3.2 General Model Development**

Select 3D-CAD geometry created in SolidWorks (Dassault Systèmes, Vélizy-Villacoublay, France) were imported in ADAMS and assigned mass properties based on their real-world composition. The imported CAD parts were those which were used to machine the existing shear test apparatus. Figure 3-2 shows the general model configuration used for the simulations.

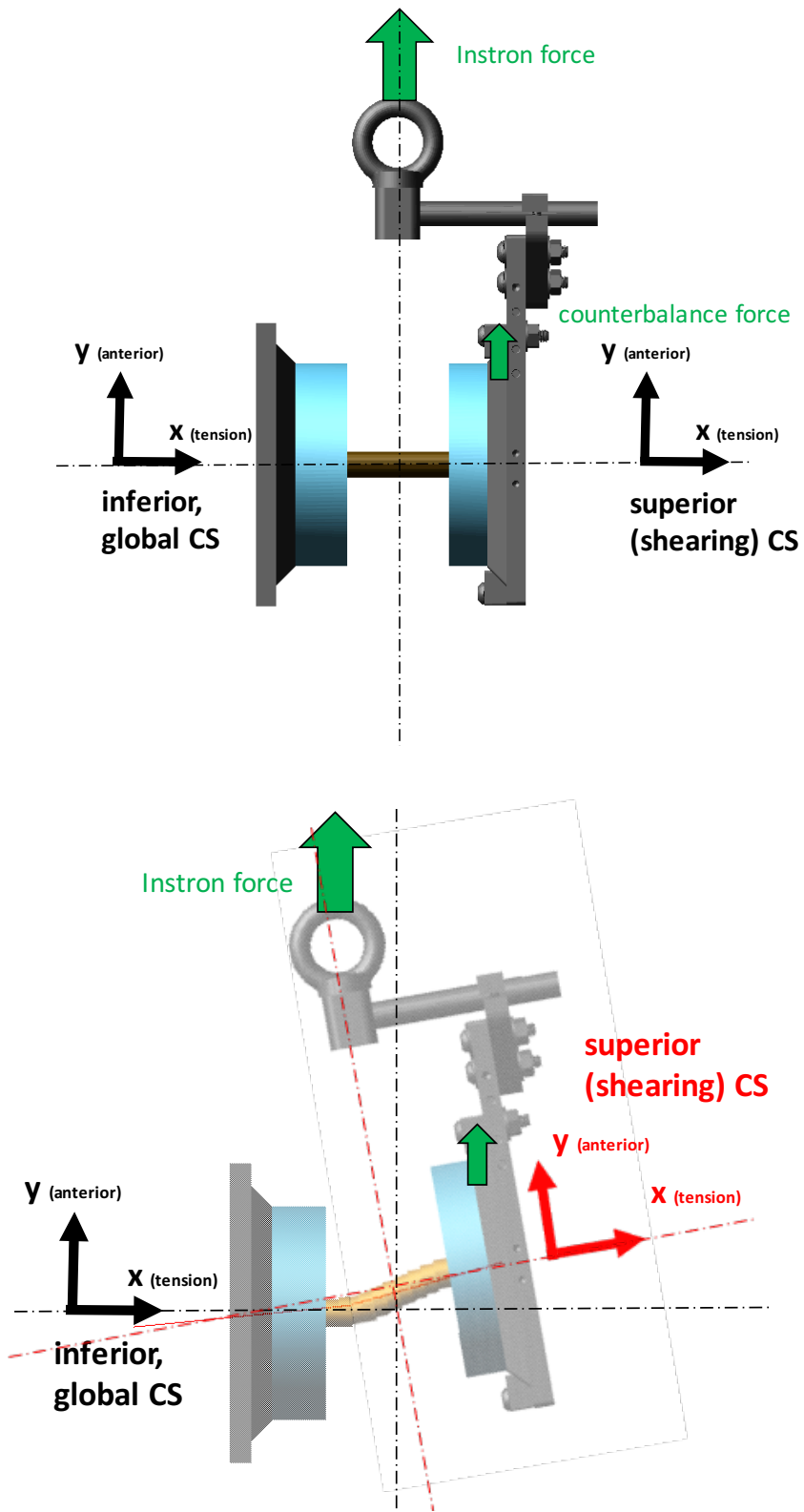


Figure 3-2: ADAMS Model of the Shear Test Apparatus at t=0 (above) and t>0 (below)

The inferior and superior PMMA potting cups were modeled as perfect cylinders, and were assigned a uniform density based on the measured mass of a representative PMMA cup. Two specimen models were used in simulations; a rubber-based specimen and a cadaver-based specimen. The former was modeled after a 12.7 mm (0.5”) diameter, 50 mm long rubber cylinder (McMaster-Carr, Elmhurst, IL, USA), and was represented by an 8-element cylindrical flex-part rigidly fixed to the centre face nodes of the opposing PMMA cups. Material properties (Table 3-1) were taken from the manufacturer’s specification sheet.

**Table 3-1: Material Property and Geometry Definitions Used for Rubber Specimen**

	<b>Density <i>kg/m<sup>3</sup></i></b>	<b>Young’s Modulus <i>MPa</i></b>	<b>Poisson’s Ratio</b>	<b>Number of elements</b>
<b>Rubber specimen</b>	1100	13.8	0.48	8

The cadaver-based specimen was modeled after a 50 mm long human cervical FSU, and was represented by a bushing-like joint between the centre face nodes of the opposing PMMA cups. Stiffness values (Table 3-2) for the bushing-like joint were taken from Moroney *et al*, 1988. Two versions of the cadaver-based specimen were modeled: a mean stiffness FSU, representing the mean reported shear and flexion-extension stiffness and a low stiffness FSU, representing the lowest reported compressive, shear and flexion-extension stiffness from the Moroney *et al*. Mean directional stiffness values were used in both specimen definitions for axial compression, lateral shear, lateral bending and torsion. The two cadaver specimen models were tested as problems with large flexion-extension rotations were observed mostly in specimens that were more flexible (ie. low stiffness), and so incorporating some aspect of the variability of cadaveric specimens was desired.

**Table 3-2: Directional Stiffness Properties Used for Cadaver-based Specimen Simulation**

	<b>Compression <i>N/mm</i></b>	<b>Anterior Shear <i>N/mm</i></b>	<b>Lateral Shear <i>N/mm</i></b>	<b>Torsion <i>Nmm/°</i></b>	<b>Lateral bending <i>Nmm/°</i></b>	<b>Flexion <i>Nmm/°</i></b>
<b>Mean Stiffness</b>	1318	131	119	1160	680	430
<b>Low Stiffness</b>	1318	29	119	1160	680	100

For all tests, the inferior potting plate and inferior PMMA cup were fixed (0 dof). A constant force in the global y-direction (against gravity) equal in magnitude to the mass of the loading plate, superior PMMA and half of the specimen was applied at the centre of mass of these parts. This force represented the counterbalance system used in the physical test apparatus.

The Instron actuator force was modeled as the result of a 0.5 mm/s displacement in the global +y-direction at the location where the cable connecting the loading plate to the actuator would be attached (top-centre of ring seen in Figure 3-2). Simulations were run to a peak shear displacement of 10 mm, measured in the global coordinate system. Experimentally, this would be equivalent to the LVDT (linear variable differential transformer) displacement measured by the Instron. A one-second hold was implemented at the beginning and end of the 10 mm to ensure static equilibrium. The number of degrees of freedom assigned to the loading plate varied depending on which axial compression was used, and will be discussed more specifically in the following sections. A step size of 0.1 s was used for all simulations.

### **3.3 Question 1: Effect of different axial compression methods**

#### **3.3.1 Specific Model Development**

For all axial compression methods, compressive loads were modeled as a single force acting in the x-y (sagittal) plane. The magnitude of the axial compressive force was kept

constant throughout a single simulation trial. Each compression method is illustrated in Figure 3-3, and compared to each other in Table 3-3.

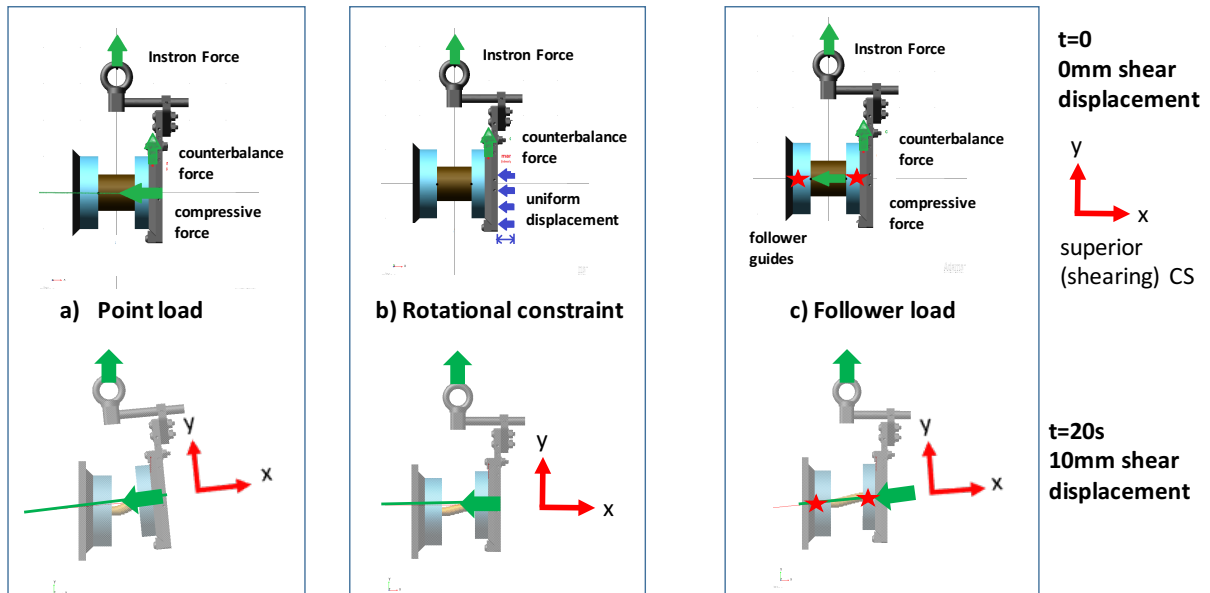


**Figure 3-3: Visualization of applied forces during the (a) point load, (b) rotational constraint, and (c) follower load before and after anterior shear displacement<sup>2</sup>**

**Table 3-3: Comparison of the Three Simulated Axial Compression Methods**

	a) Point load	b) Rotational Constraint	c) Follower load
Specimen dof	6 dof 	1 dof (A-P shear translation) 	6 dof 
Specimen artefact moment	Flexion moment 	Extension moment 	Flexion moment 
Line of action	Body-fixed to loading vertebra	Body-fixed to loading vertebra	Line-of-sight between vertebrae
Specimen artefact shear force	None (superior CS)	None (superior CS)	y-component (superior CS) of compressive force

Point load forces (a) were body-fixed to the loading plate coordinate system and acted only in the loading plate's x-direction (superior-inferior axis). The point of application at t=0 s was (50

<sup>2</sup> Applied forces were exaggerated for visualization purposes in this figure; these results are not representative of those described in this study

mm, 0, 0), where the origin was located at the specimen centre at  $t=0$  for all simulations. In this method, the loading plate and superior PMMA were assigned 6 dof.

The rotational constraint compressive force (b) was applied in the same manner as the point load, but with the addition of rotational motion constraints on the loading plate. Two dof were permitted: anterior-posterior shear translation and compressive-tensile translation. Thus, the compression force applied through the simulation was constant, but the displacement in x (superior-inferior axis) could vary during a run as necessary to ensure a constant compressive force.

Follower loads were applied as a line of sight force between two points – one on the inferior fixed plate and one on the loading plate. These points represent potential locations of what would be physical guides for the cable applying the compressive force. For the purposes of comparison to the other compression methods, the superior guide node was positioned 50 mm from the specimen centre, and the inferior guide node was positioned 50 mm from the specimen centre for these simulations (Figure 3-4). These dimensions will be referred to as L1 (superior guide position) and L2 (inferior guide position) values respectively.

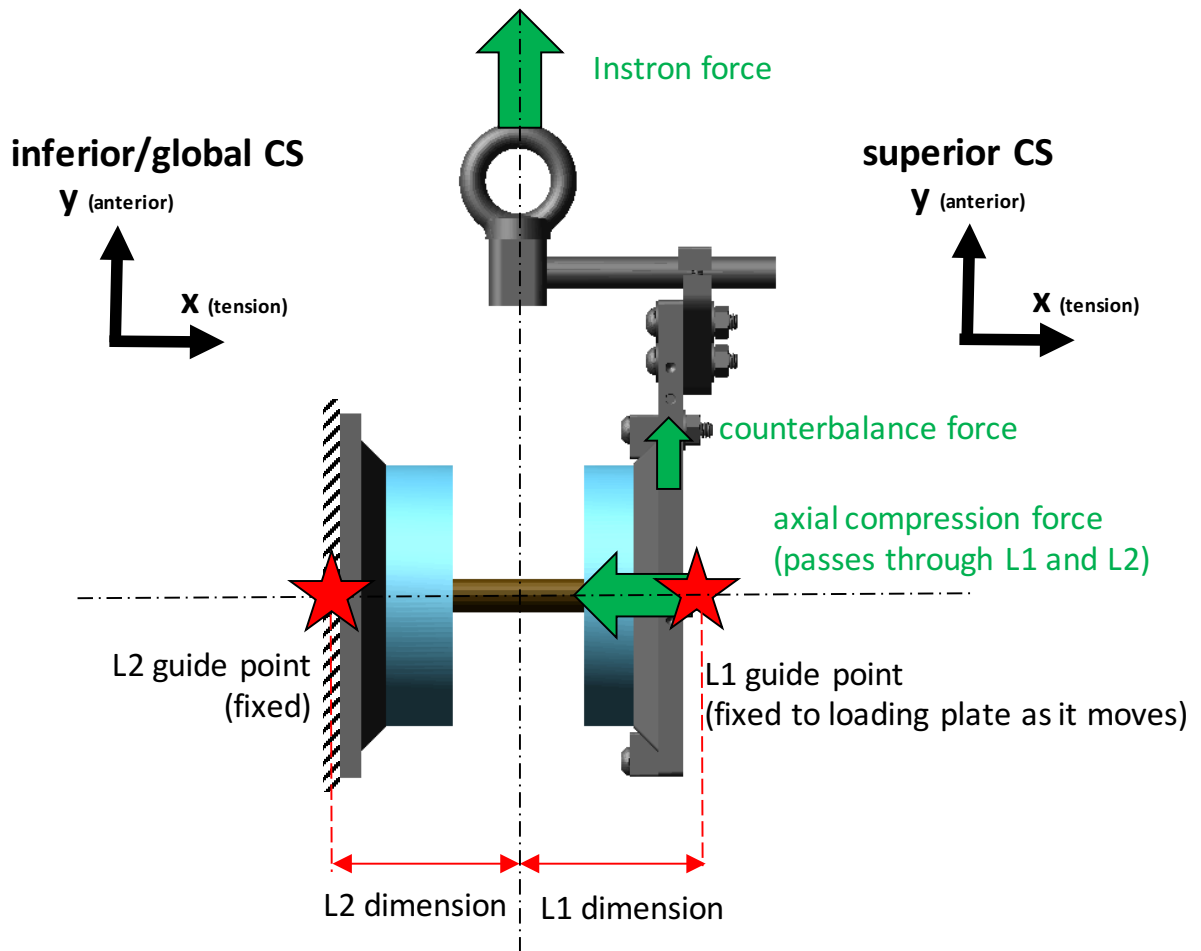


**Figure 3-4: Measurement of L1 and L2 in the follower load method at 0mm shear displacement (L1=50 mm, L2=50 mm shown)**

In each axial compression method an artefact moment is applied to the specimen as anterior shear displacement of the loading plate creates some eccentricity relative to the specimen centre. When rotation is not constrained (point load, follower load) a flexion moment is applied to the specimen during anterior shear, whereas an extension moment is applied when rotation is constrained. The extension moment arises from the enforcement of the rotational constraint. Because rotation is constrained, the axial compressive force acts as a distributed load on the loading plate, where the resultant reaction force acts somewhere posterior to the specimen balance point in order to maintain equilibrium (creating an extension moment). No artefact shearing force is imparted during the point load and rotational constraint methods as the

compressive force has no component in the superior (shearing) coordinate system y-direction (anterior-posterior shear). Further detail on how the different axial compression methods and constraints influence the direction of the artefact load experienced by the specimen is provided in Appendix E.

In the follower load compression method, both an artefact moment and an artefact shearing force are imparted on the specimen. The artefact shearing force results because the line of action of the follower load force is not fixed to the superior specimen coordinate system. Depending on the specimen kinematics and location of the guides, the compressive force may have some non-zero y-component (anterior-posterior shear direction). In the case of application of an anterior shear force, this artefact force acts in the posterior direction, and reduces the actual shear force applied to the specimen. Thus, if anterior shear load is measured experimentally using an in-line Instron load cell, the measured load will not necessarily be the same as what is applied to the specimen.

For the purposes of comparing the three different axial compression methods, only their influence on specimen artefact moments and flexion-extension rotation was considered. Four levels of axial compression were simulated for each axial compression method: 0, 300, 500, and 800 N. Simulations were run for each axial compression method (point load, uniform displacement, follower load) using the rubber specimen model, and both the low and mean stiffness FSU models (total of 36 simulations).

Specimen moments were measured at each time instant at the geometric centre of the specimen. In the rubber specimen, the moment was measured in ADAMS at each time point at the inferior anchor node of the rubber beam (-50 mm, 0, 0) and transformed to (0, 0, 0), which corresponded to the initial position of the geometric centre of the specimen at  $t = 0$  s. In the cadaver specimen model, which was modeled as a bushing-like joint, the moment was measured in ADAMS about the inferior joint node (0, 0, 0). Moments reported herein represent

the reaction moment at the inferior joint node, where the net moment (that which causes rotation at the superior node) is reported separately by ADAMS. All specimen moments, forces and displacements are reported in the superior (loading plate) coordinate system, in accordance with previous work by Cripton *et al* (2000). Specimen rotations are reported as the rotation of the superior (loading plate) coordinate system relative to the inferior (fixed plate, global) coordinate system. The Instron force and axial compression forces are reported as magnitudes. Further detail on the algorithm used by ADAMS to determine moments, as well as diagrammatic visualizations are provided in Appendix E.

### 3.3.2 Simulation Results

#### *Rubber Specimen Simulations*

The rubber specimen responded to the different axial compression methods in a manner consistent with what would be intuitively expected, based on knowledge of the theoretical differences between the loading scenarios in each method described previously. Because the rubber specimen was modeled using linear material properties, it was relatively inflexible in flexion-extension (as compared to a cervical FSU), and thus did not experience the large flexion-extension rotation angles that were observed during previous cadaveric experiments. All flexion rotation angles were  $<0.5^\circ$  at the peak anterior shear displacement (10 mm), which always coincided with the peak flexion-extension moment. Sample simulation outputs for each compression method for the 300 N level of compression are listed in Table 3-4.

**Table 3-4: Sample simulation outputs for rubber specimen at 10 mm anterior shear with a 300 N compressive force**

	$F_{\text{instron}}$ [N]	Inferior displ [mm]	Anterior displ [mm]	Flexion rotation [°]	Axial compr [N]	Artefact post. shear [N]
<b>Point load</b>	1660	0.86	10.1	0.10	300	0
<b>Rotationally constrained</b>	1660	0.85	10.1	0	300	0
<b>Follower load</b>	1680	0.84	10.0	0.12	299	29.8

With respect to specimen flexion-extension moments, a linear relationship was observed with increasing amounts of applied axial compression. It was found that the rotationally constrained compression method (b) resulted in the largest flexion-extension artefact moments, while the follower load (c) resulted in the least amount of artefact moment. This was found to be true for all magnitudes of axial compression assessed. In simulations where the axial compressive force was equal to 0 N (no axial compression), the artefact moment was predicted to be near-zero. These results are illustrated in Figure 3-5.

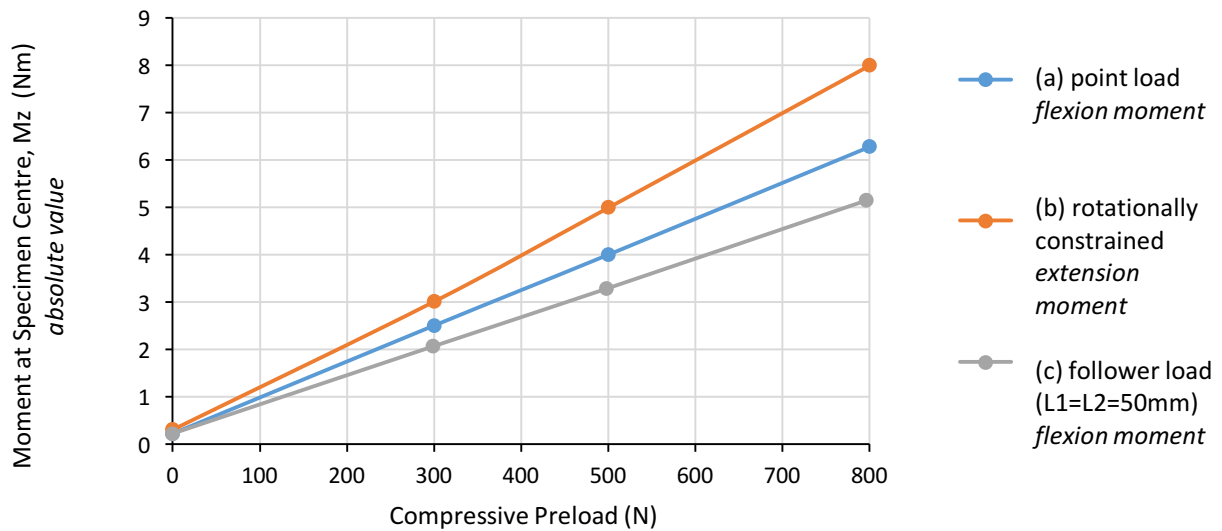


**Figure 3-5: Simulated effect of different compressive force application methods on flexion-extension moment at 10 mm anterior shear in a rubber specimen model**

### *Cadaver Specimen Results*

The trend with respect to the effect of the different axial compression methods was found to be the same for the cadaver specimen models; the follower load produced the least amount of artefact moment, while the rotationally constrained method resulted in the greatest amount of artefact moment. Between the mean stiffness and low stiffness variations of the cadaver model, some differences in response were observed.

Results from the mean stiffness cadaver specimen model were generally quite similar to those of the rubber specimen model, in terms of kinematics (Table 3-5) and the linearity of response to the various compressive methods and compressive magnitudes (Figure 3-6). The mean stiffness model exhibited more flexion rotation at peak anterior shear displacement in the point load method (Figure 3-7) as compared to the rubber model, but these angles were still relatively small (<2 °).

**Table 3-5: Sample simulation outputs for cadaveric specimen (mean, low stiffness) at 10 mm anterior shear with a 300 N compressive force**

	<b>F<sub>instron</sub></b> <b>[N]</b>	<b>Inferior</b> <b>displ</b> <b>[mm]</b>	<b>Anterior</b> <b>displ</b> <b>[mm]</b>	<b>Flexion</b> <b>rotation</b> <b>[°]</b>	<b>Axial</b> <b>compr</b> <b>[N]</b>	<b>Artefact</b> <b>post.</b> <b>shear [N]</b>
<b>Point</b> <b>load</b>	1370	0.33	10.5	0.63	300	0
	298	0.99	10.9	4.1	300	0
<b>Rotationally</b> <b>constrained</b>	1380	0.23	10.5	0	300	0
	305	0.23	10.5	0	300	0
<b>Follower</b> <b>load</b>	1400	0.27	10.5	0.26	298	32.1
	334	0.49	10.6	1.5	297	35.4

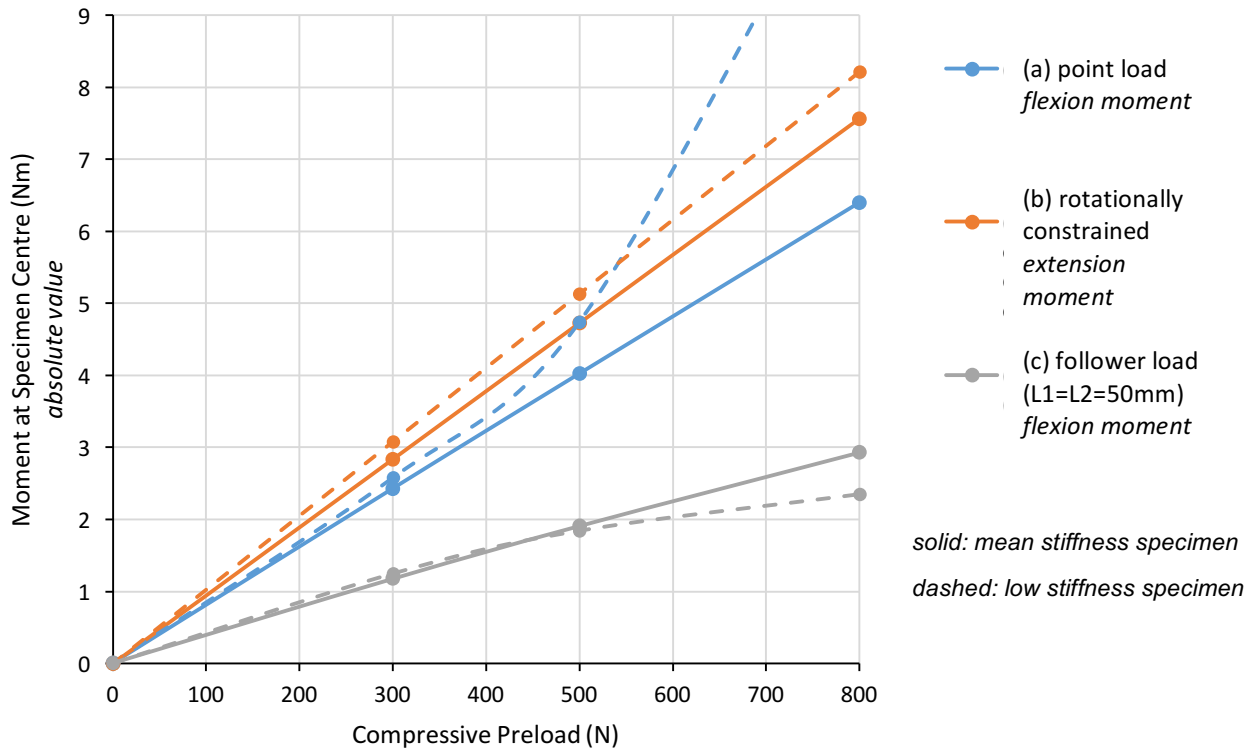


**Figure 3-6: Simulated effect of different compressive force application methods on flexion-extension moment at 10 mm anterior shear in a cadaveric specimen**

In the low stiffness specimen model, some interesting results were observed. Most notably, large flexion-extension rotations were observed when rotation was not constrained, to the extent that the model became unstable when the point load method was used in conjunction with an 800 N axial compressive force (Figure 3-7). The instability in this particular simulation manifested as the two potting plates interacting with each other, and the ADAMS solver was unable to enforce both the 0.5 mm/s loading rate and axial compressive force. This instability did not occur in any other simulations.

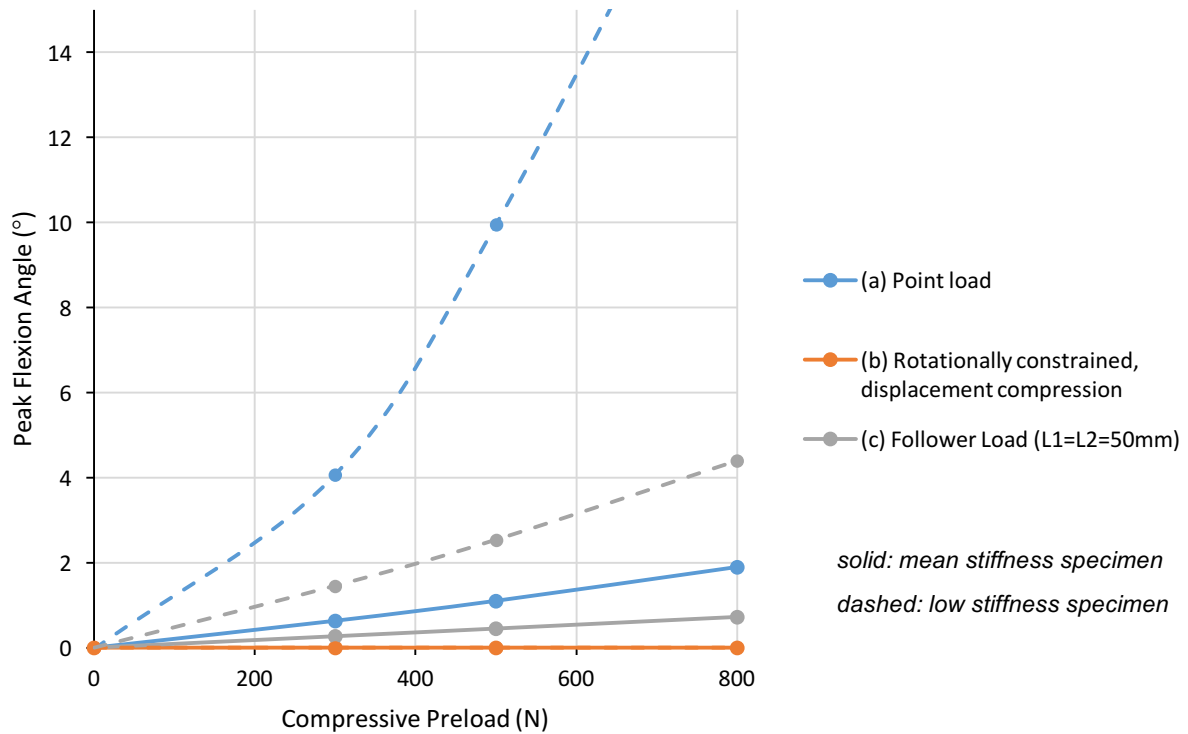


**Figure 3-7: Simulated effect of different compressive force application methods on peak flexion-extension rotation at 10mm anterior shear in a cadaveric specimen**

Additionally, in the point load and rotationally constrained methods, increased flexion-extension moments were observed, relative to the equivalent simulation run with mean stiffness properties (Figure 3-6). In the follower load method, flexion-extension moments were found to be similar in both cadaver specimen models, except at a compressive load of 800 N, where a slight decrease of 0.6 N was observed in the low stiffness specimen. In both the point load and follower load method, the response of flexion-extension moment became non-linear above 500 N of axial compression. This non-linear behaviour was more apparent in the point load method.

### 3.3.3 Discussion

Inevitably, applying an axial compression load (using any method) during shear testing will impart some flexion-extension moment on a specimen, where greater compressive loads

result in greater flexion-extension moments. This was demonstrated in both the rubber specimen model and cadaveric specimen model simulations. Because flexion-extension moments may cause altered kinematics or affect failure mode in a cadaveric specimen, there is a trade-off between assessing the “pure” shear characteristics and assessing the shear characteristics in a manner that is relevant to an *in vivo* scenario (ie. including realistic amounts of axial compression). Which of these considerations is more important may depend on the event application.

If the objective is to minimize flexion-extension moments experienced by the specimen and having some rotation is acceptable, the simulation results suggest that selecting a follower load would provide the greatest reduction in flexion-extension moment. That said, if larger (>500 N) axial compression pre-loads are used, even the follower load method may not reduce flexion-extension moments sufficiently. This method may also be desirable as the effect of specimen stiffness had minimal influence on flexion-extension moments, meaning that specimens that are more flexible could be tested more reliably. This is an important consideration if results are to be used to determine injury tolerance thresholds, as the sample population should ideally be as representative of the general population as possible. If low stiffness, flexible specimens are excluded due to experimental issues, injury tolerance thresholds might not be sufficiently protective.

Conversely, if the objective is to ensure that displacement only occurs in the shearing direction and potentially large flexion-extension moments are not as much of a concern, then a rotationally constrained method may be appropriate. The effect of the boundary conditions should however, be considered, particularly if experimental results are to be translated to FE modeling.

Although the point load method offers an intermediate flexion-extension moment for a given axial compression load, based on the simulation results it is a less desirable choice unless

compressive loads are to be very small (below 300 N) or if a simple design is a priority. Since the point load method allows flexion-extension rotation, the larger flexion-extension moments caused by this method compared to the follower load method will likely result in more rotation for a given amount of axial rotation. This is undesirable as large flexion-extension angles mean that the shear properties of the specimen are no longer being assessed.

With regard to flexion-extension rotations in the different specimen models, it was found that the rubber specimen model and the mean stiffness specimen model did not undergo large flexion-extension angles, even when large flexion-extension moments were applied. Only when low stiffness values were assigned to the cadaver specimen model did larger flexion-extension rotations occur in the point load method. This is consistent with observations made during previous experimental attempts to use the point load method (325 N axial compression) during anterior-posterior shear testing. During these experiments, some cadaveric specimens tolerated the point load method without substantial flexion-extension rotations, while others did not. In the specimens that experienced large flexion-extension angles, flexion of up to 12 ° were observed. It should be noted that due to the design of the test apparatus, flexion angles greater than this are not possible due to direct contact of the apparatus parts, and so larger flexion angles might have occurred without this restriction. Though such large flexion angles were not predicted in the ~300 N range, it is possible that internal geometric features (eg. endplate curvature, inclination of the facet joints) of the FSU might contribute to the increased flexion angles observed experimentally. The bushing-like joint with linear stiffness values used in the ADAMS model did not account for these features, and so the flexion-extension rotations described in Figure 3-7 might be considered as low-end estimates of rotation behaviour.

In this question, only artefact moments were considered. As discussed in further detail in the following section, using a follower load method to apply a compressive force results in both an artefact moment and an artefact shear load. In the point load and rotationally constrained

methods, no artefact shear load exists because the line of action of the compressive force is always parallel to superior-inferior axis of the shearing vertebra.

Another interesting finding was that in the follower load method, the low stiffness specimen experienced lower artefact flexion moments than the mean stiffness specimen at higher axial compression levels (500, 800 N). Intuitively, one might expect that the low stiffness specimen would experience slightly larger artefact moments at the same axial compression magnitude, as observed in the other two axial compression methods. This result would be expected as the low stiffness specimen has a greater tendency to rotate in flexion-extension, which contributes to the creation of artefact moments for a given amount of axial compression, as per the mathematical model.

In the follower load method, this phenomenon did not occur at higher axial compressive loads. When applying anterior shear forces with axial compression, a small extension artefact moment is created by the anterior shear force in accordance with the superior-inferior deformation of the specimen during axial compression (ie. Instron force not perfectly aligned to the specimen centre after application of an axial compressive force). This artefact moment would tend to be slightly larger in the low stiffness specimen, as this specimen will deform to a greater extent under combined axial compression forces and anterior shear forces. In the point load and rotationally constrained methods, this small extension moment was overwhelmed by the much larger artefact moments created by the eccentricity of the axial compressive force. Because in the follower load method the artefact flexion moment and flexion rotation increases less dramatically at higher axial compression levels, the effect of this small extension moment was more apparent. Thus, this finding is primarily a result of the compliance of the low stiffness specimen.

## 3.4 Question 2: Effect of follower load guide position

### 3.4.1 Specific Model Development

Follower loads were modeled as described previously, as a line-of-sight force between two nodes anchored to the superior (L1) and inferior plates (L2). The L1 and L2 positions are defined as the superior-inferior (x) distance from the centre of the specimen, and are fixed to this relative location. To assess the effect of different guide positions, the x-position of the two nodes, representing the guides were varied for different test runs to achieve different absolute positions and different ratios.

In a previous work by Cripton *et al* (2000), a mathematical model of the follower load method was developed. In this model, a single FSU was subjected to static axial compressive loads at different flexion-extension rotation angles. The theoretical forces at the specimen centre resulting from each loading scenario were described mathematically using a free body diagram model, and compared with experimental results from a cadaveric lumbar FSU model.

This model describes three variables that influence artefact loading in the FSU for a given amount of axial compression: the absolute positions of the guides from the specimen centre (L1 and L2 measurements), the ratio of the guide positions (L1/L2 ratio) and the specimen flexion-extension angle. These free body diagram-derived equations for predicted artefact moments and artefact shear forces are shown in equation 1 and equation 2. A visualization of the free body diagram upon which these equations are based may be found in Figure 3-8.

$$M_{\text{artefact flexion}} = F_{\text{compression}} \times \text{moment arm} = F_{\text{compression}} \times \frac{L_1 L_2 \sin(180 - \theta_{\text{flexion}})}{\sqrt{L_1 + L_2 - 2L_1 L_2 \cos(180 - \theta_{\text{flexion}})}} \quad (1)$$

$$F_{\text{artefact posterior shear}} = F_{\text{compression}} \times \frac{L_1 \sin(180 - \theta_{\text{flexion}})}{\sqrt{L_1 + L_2 - 2L_1 L_2 \cos(180 - \theta_{\text{flexion}})}} = \frac{M_{\text{artefact flexion}}}{L_2} \quad (2)$$

(Cripton et al, 2000)

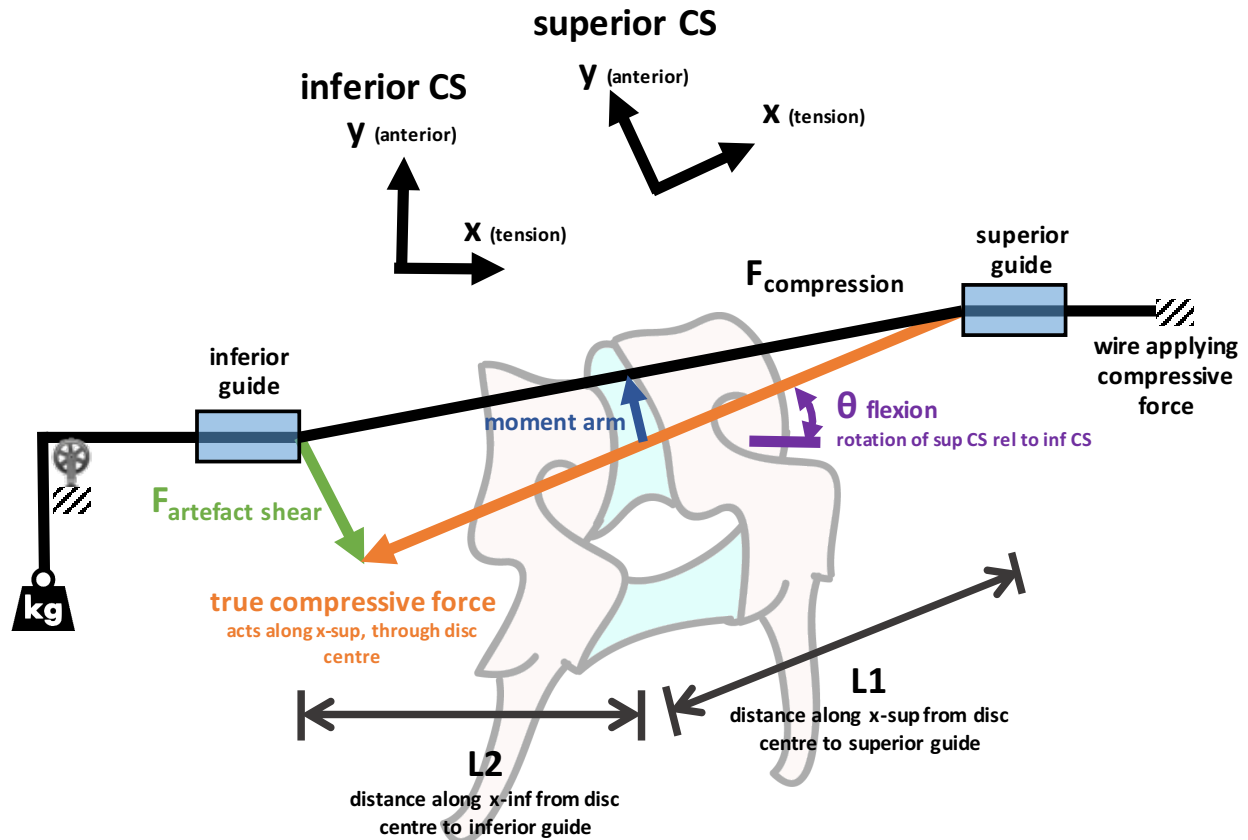


**Figure 3-8: Annotated diagram of artefact loading imparted during use of follower load method in a FSU, after some anterior shear displacement and flexion**

From this model, for a given  $L_1/L_2$  ratio, the absolute size of the dimensions  $L_1$  and  $L_2$  affect the size of the moment arm. For a given  $L_1$  value, the  $L_1/L_2$  ratio influences the line of action of the compressive force, which affects the amount of artefact shear force that is imparted on the specimen. Finally, for a given  $L_1/L_2$  ratio and size of  $L_1$ , the flexion angle  $\theta$  changes both the line of action of the compressive force and the moment arm.

Because the mathematical model does not consider the effect that both flexion-extension rotation and shear loading might have on artefact loading, this model may not be entirely applicable to the present work. As such, a multibody dynamics model of the follower load method (Figure 3-9) using different absolute dimensions of L1 and L2 as well as different ratios of L1 and L2 was assessed, and compared with the predictions made for these parameters in the mathematical model. The cases considered for analysis in both models are listed in Table 3-6. Because the point load method is in a sense, a special case of the follower load method (where the guide position L2 is located at infinity), this case was also considered to represent the extreme end of the spectrum of possible L1/L2 ratios (ie.  $L1/L2 \rightarrow 0$ ).

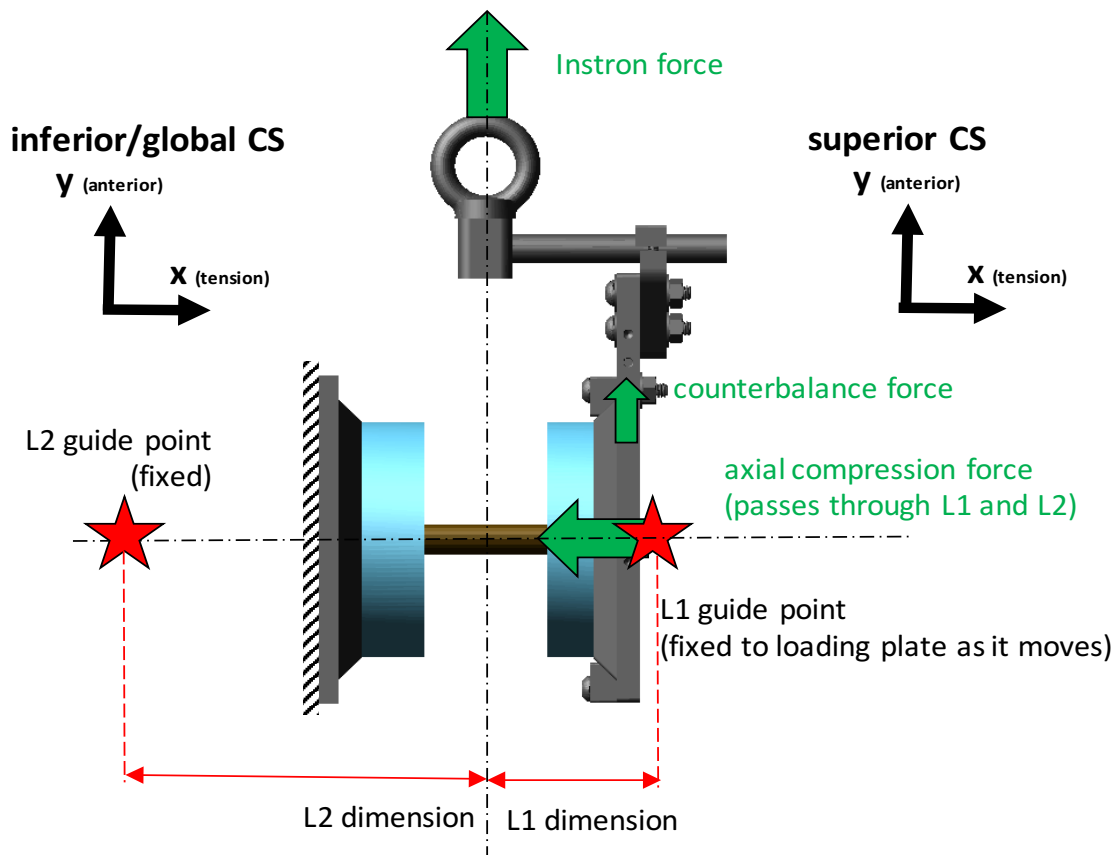


**Figure 3-9: Measurement of L1 and L2 in the follower load method at 0mm shear displacement (L1=50 mm, L2=85 mm shown)**

**Table 3-6: L1 and L2 dimension cases assessed in multibody dynamics model and mathematical model**

<b>Follower Load Cases Assessed</b>	<b>L1 (mm from specimen centre)</b>	<b>L2 (mm from specimen centre)</b>	<b>L1/L2 ratio</b>
Point load	50	$\infty$	0
Variants of L1=30	30	9	3.33
	30	30	1.00
	30	51	0.59
Variants of L1=40	40	12	3.33
	40	40	1.00
	40	68	0.59
Variants of L1=50	50	15	3.33
	50	50	1.00
	50	85	0.59

It should be noted that in the mathematical model, one of the variables affecting the artefact loading is the flexion-extension angle  $\theta$ . In the multibody dynamics model, prescription of this angle was not necessary, as the ADAMS software computes deformations of the specimen resulting from the input loads at each time step. In the mathematical model, some flexion-extension angle  $\theta$  must be assumed; for the purposes of analysis herein, artefact loads were calculated for each case listed in Table 3-6, at a flexion angles  $\theta$  of 6 ° and 12 °. These angles were selected as they represent larger, but still reasonable amounts of flexion that could occur during a failure test of a cervical FSU based on results from a literature review (Section 1.2.5).

The different combinations of L1 and L2 values listed were selected on the basis of what might constitute practical design choices. From an experimental perspective, there is some risk of having the L1 and L2 guides interfere with each other if they are positioned too closely together (ie. very small L1 and L2 values). A secondary consideration in choosing the selected L1 and L2 dimensions was to ensure that a variety of dimensions fitting the same L1/L2 ratios were tested in order to assess the effects of absolute dimension and dimension ratio independently.

### 3.4.2 Simulation Results

#### Mathematical Model Results

In the mathematical model, there exists an inverse relationship between the amount of artefact shear and the amount of artefact moment for a given set of L1 and L2 guide positions; minimizing both parameters simultaneously is not possible. This relationship is demonstrated in Figure 3-10, which shows paired artefact moment (blue and green) and artefact shear force (red and orange) curves for a given L1 dimension, where L2 is varied to achieve different L1/L2 ratios for each curve. For example, for an L1=30 mm, the darkest blue curve and the darkest orange curve represent the artefact moments and artefact shear forces that occur at different L1/L2 ratios, assuming a flexion angle of 12 °.

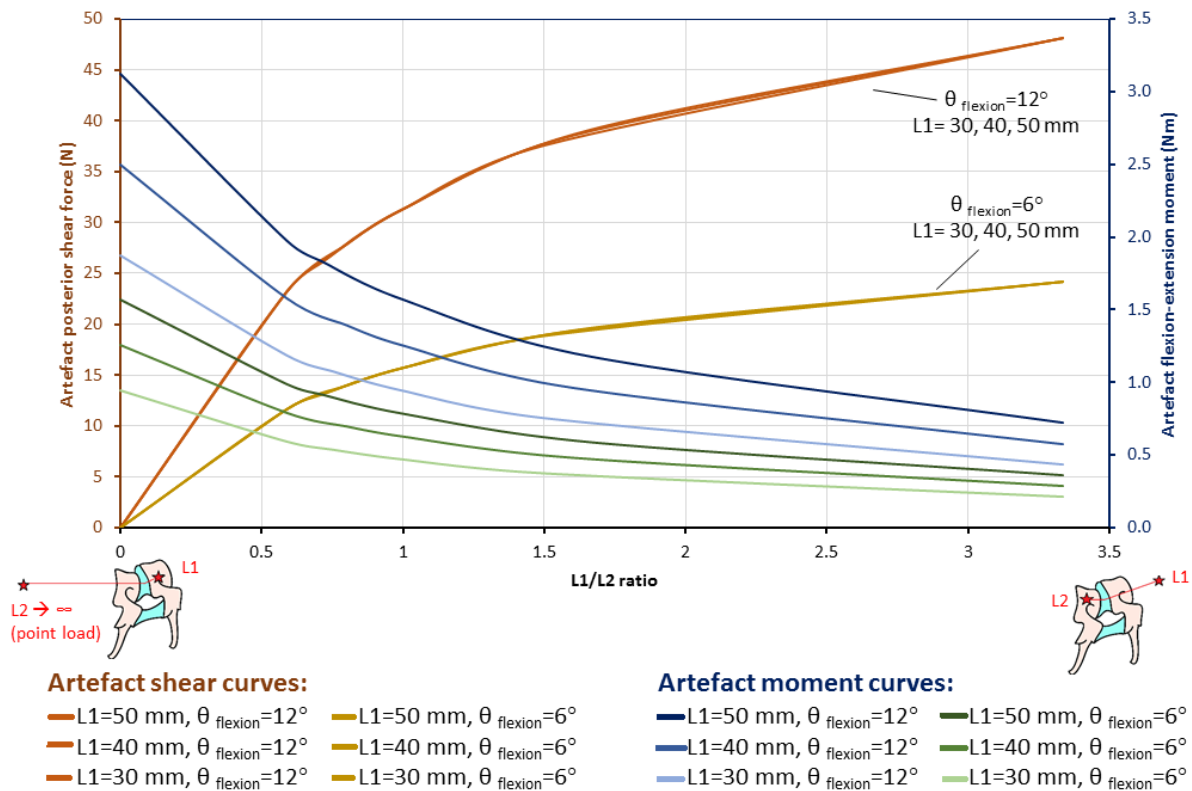


**Figure 3-10: Mathematical model predictions of the effect of different follower load guide positions on specimen artefact loading**

From this plot, it can be seen that in general, larger L1/L2 ratios reduced artefact moments and increased artefact shearing forces. For a particular L1/L2 ratio, smaller L1 measurements reduced artefact moments, but had no effect on the artefact shearing force. Increasing flexion angles shifted both the artefact moment and shear curves upwards. The absolute reducing effect of having a larger L1/L2 ratio was also more pronounced with a larger flexion angle (reduction from 3.1 Nm to 0.7 Nm for 12 ° versus a reduction from 1.6 Nm to 0.4 Nm for 6 ° for an L1=50 mm).

Of the dimensions input into the mathematical model, L1/L2=30/9 resulted in the least amount of artefact moment, whereas the point load case L1/L2=50/∞ resulted in the most artefact moment. The opposite is true of artefact shearing loads for these cases.

#### *Rubber Specimen Results*

In the ADAMS simulation of the same follower load guide position cases, there was agreement in the overall trend of reduced artefact moments resulting in increased artefact shearing loads (and vice versa) for all specimen definitions. Curve shapes were similar between the mathematical model and the ADAMS model for all specimen definitions, where the effect of L1/L2 ratio on artefact loading was most pronounced below unity.

Similarity between the mathematical and ADAMS models can be seen in Figure 3-11, which illustrates the artefact moments (blue curves) and artefact shearing forces (orange curves) resulting from varying L1/L2 ratios, where each curve represents a different L1 dimension. As in Figure 3-10, curves are paired such that each L1 dimension is represented by a blue and an orange curve. Because rotations resulting from the various forces applied to the specimen during the anterior shear test simulation were determined by ADAMS, the effect of rotation is imbedded in the present results. In the case of the rubber specimen, rotations were negligible (<0.5 °) in all configurations tested.

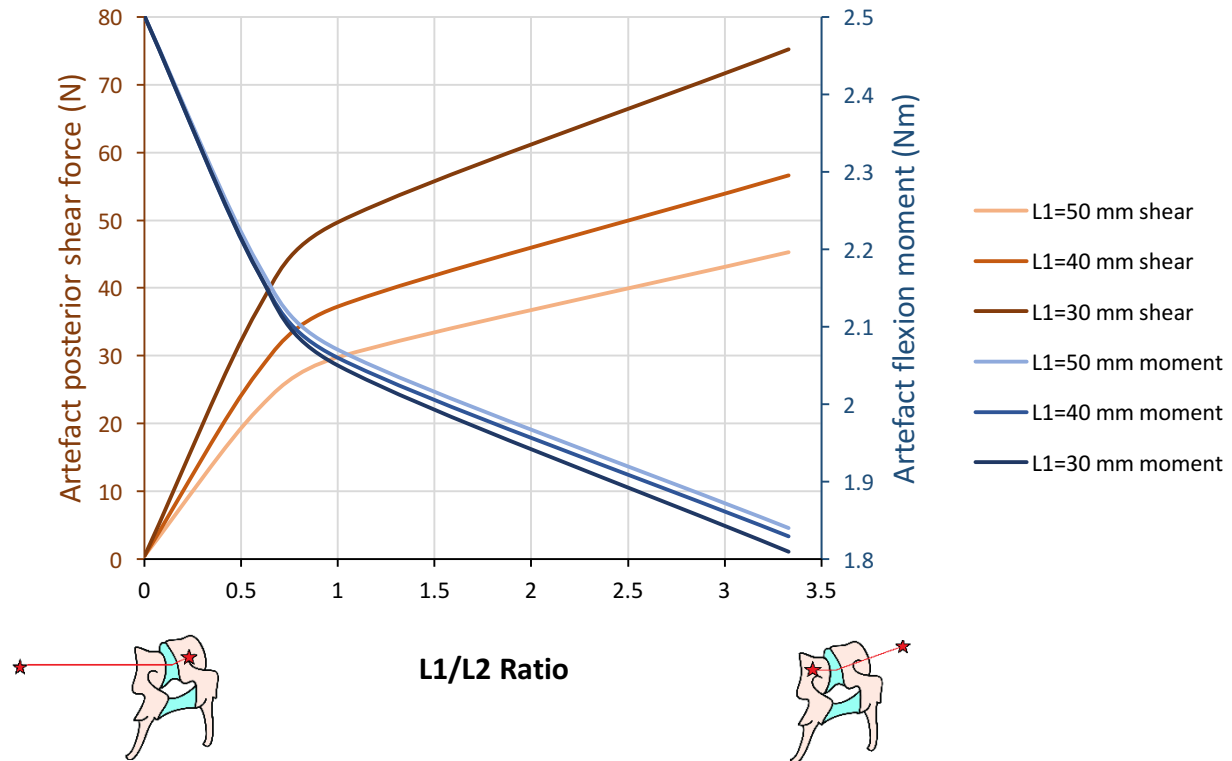


**Figure 3-11: ADAMS simulation predictions of the effect of different follower load guide positions on specimen artefact moments (blue) and artefact shear loading (orange) in a rubber specimen model**

Similar to the mathematical model, the ADAMS simulation showed that having a small L1 value in conjunction with a large L1/L2 ratio resulted in the least amount of artefact moment. However, the difference between the different L1 dimension curves was however, much smaller in the rubber simulations (maximum difference equal to 0.04 Nm) than in the mathematical model. Although not identical, the order of magnitudes between the artefact loads determined by the mathematical model and rubber simulations were similar.

The ADAMS rubber simulations predicted that differing L1 dimensions for a particular L1/L2 ratio would have an effect on the artefact shearing forces. It was found that larger L1 dimensions best reduced the artefact shearing load for a given L1/L2 ratio. In the mathematical model, only flexion-extension rotations were predicted to influence artefact shearing forces.

Thus, from the rubber simulations predictions, the L1/L2=30/9 resulted in the greatest reduction of artefact moments, while the L1 =50 mm resulted in the greatest reduction of artefact shearing forces across all L1/L2 ratios.

#### *Cadaver Specimen Results*

In the cadaveric specimen simulations, in which literature stiffness values for a cervical FSU were implemented to create a low and mean stiffness FSU, it was found that the specific definition of the specimen had some influence both artefact loading and kinematics during anterior shear loading (Figure 3-12, Figure 3-13). These figures show the effect of varying the L1/L2 ratio for various L1 dimensions on artefact loading in the mean stiffness FSU (top) and low stiffness FSU (bottom).

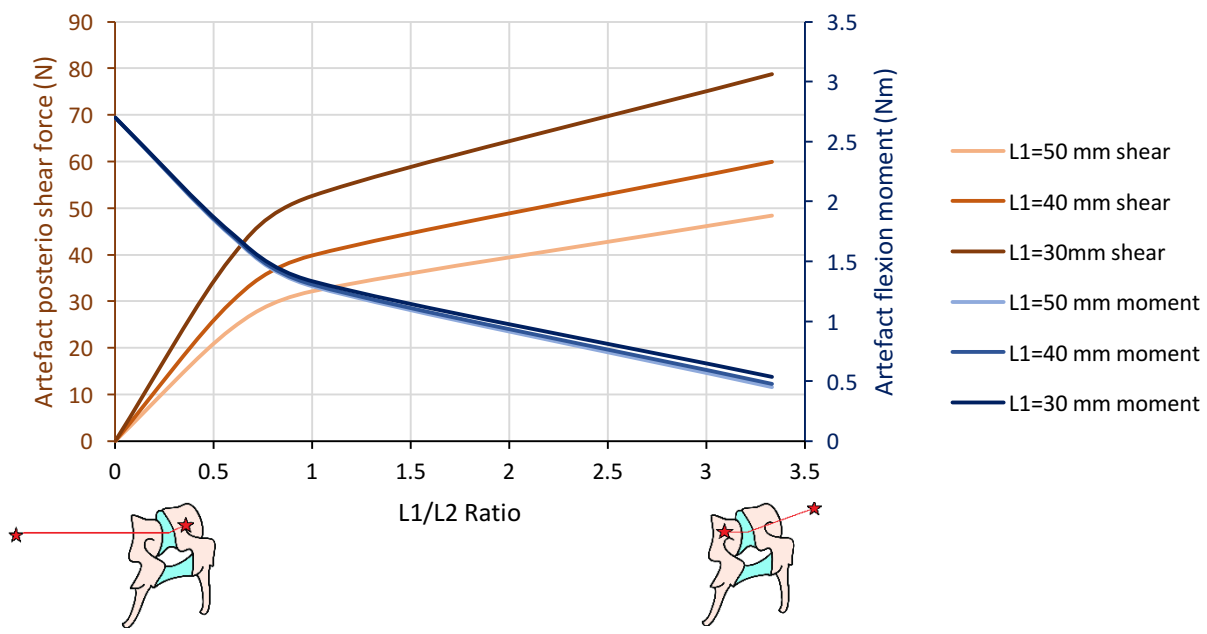


**Figure 3-12: ADAMS simulation predictions of the effect of different follower load guide positions on specimen artefact moments (blue) and artefact shear loading (orange) in a mean stiffness FSU**

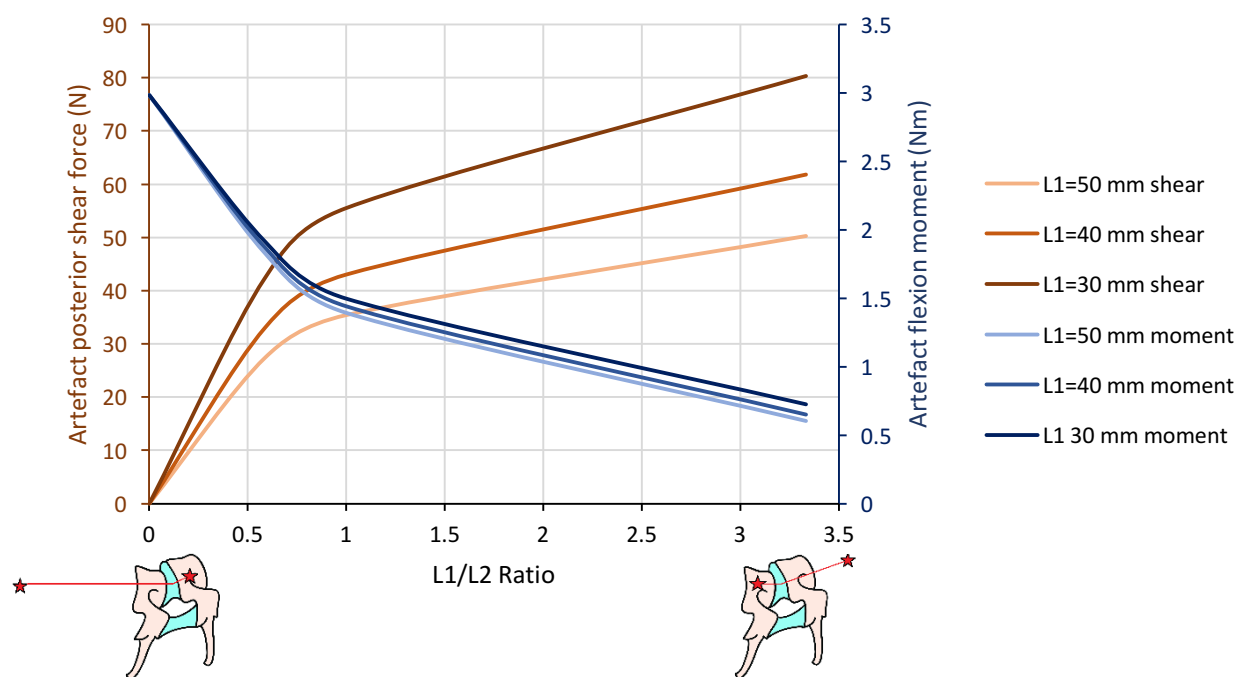


**Figure 3-13: ADAMS simulation predictions of the effect of different follower load guide positions specimen artefact moments (blue) and artefact shear loading (orange) in a low stiffness FSU**

Although the curves generated from the low and mean stiffness FSUs were quite similar in terms of best outcomes, there were some minor differences of note. In the low stiffness specimen, there was a slight upwards shift in the artefact moment and artefact shear curves. The effects of varying the L1/L2 ratio and the absolute value of L1 were similar in both cadaver specimen models.

The most apparent difference between results in the low and mean stiffness FSU models was the difference in flexion-extension rotations predicted. In the mean stiffness model, like the rubber specimen model, little flexion-extension rotation occurred during the shear test simulations ( $<0.6^\circ$ ) at 300 N axial compression. In the low stiffness specimen model, some rotation was noted (Figure 3-14). A larger L1/L2 ratio was found to result in less flexion-extension. Though the effect was very small, a smaller L1 value was found to result in lower flexion-extension angles at a particular L1/L2 ratio.

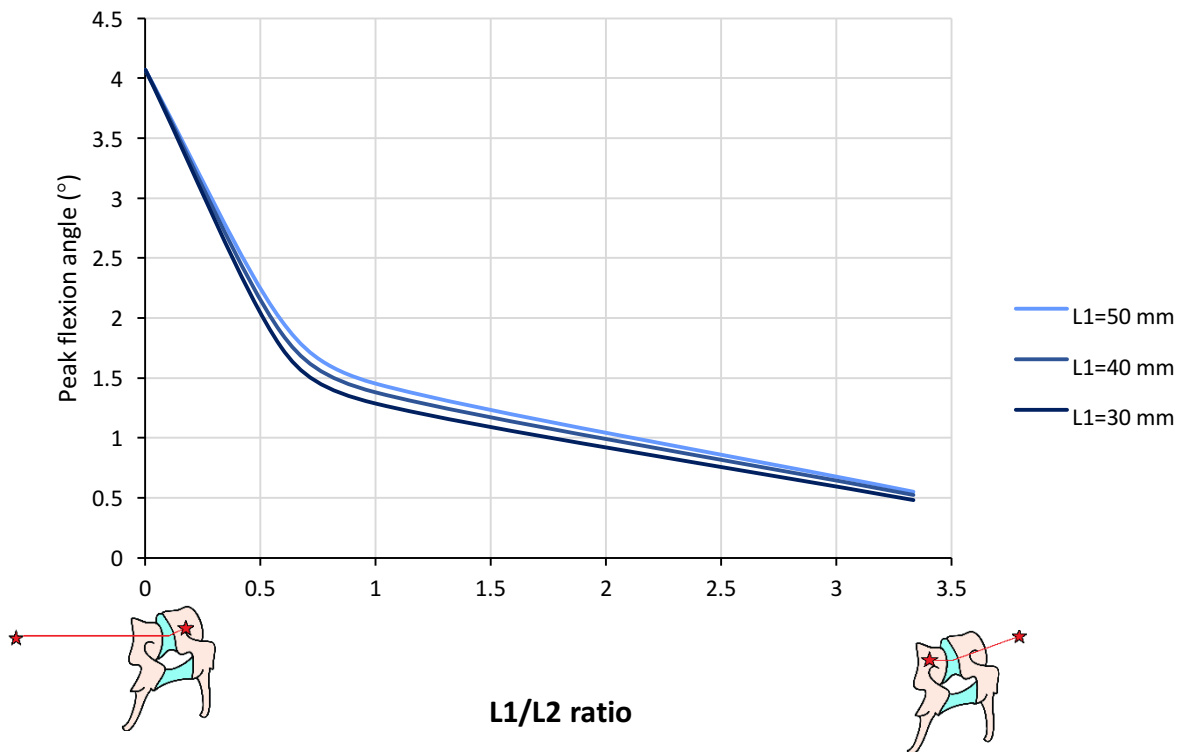


**Figure 3-14: Simulated effect of follower load guide position on flexion-extension rotation in a low stiffness FSU model**

As in the rubber specimen model, the best design choice for reducing artefact moments was the L1/L2=30/9 case, while the L1/L2=50/15 best reduced artefact shear forces. Similar to the rubber specimen model results, the effects of varying L1/L2 were most pronounced below unity.

### **3.4.3 Discussion**

In the case of the follower load axial compression method, it was found that implementing an anterior shear test specific model resulted in some findings that were not predicted by the mathematical model, which was based on flexion-extension rotation only. While the main take-away from both models is that one cannot simultaneously reduce both artefact moments and artefact shearing forces, some of the specific findings from the anterior shear specific ADAMS model have implications for design decision-making with respect to follower load guide positions.

Though both the mathematical model and the ADAMS simulations predicted that a smaller L1 dimension will reduce the artefact moment for a given L1/L2 ratio, this effect is much less pronounced in the ADAMS model. This suggests that assuming a reasonably small (<50 mm) L1 guide position is selected, that the more important design factor is the L1/L2 ratio. While it is possible that the effect of L1 position may become more pronounced in magnitudes that were not simulated herein, extending the L1 guide position beyond 50 mm from the specimen centre would be an impractical choice as this would add bulk to the superior loading plate. Thus, when considering guide positions, the simulation results suggest that the design focus should be on selecting an L1/L2 ratio that optimally balances the competing interests of artefact moment and artefact shear force.

Another difference with some design implications was that in the ADAMS simulations, the size of L1 was found to have an effect on the artefact shearing force for a particular L1/L2

ratio. In the mathematical model, artefact shearing forces were constant for a given L1/L2 ratio and flexion angle, regardless of the L1 dimension selected. This difference in outcome is a result of the differences in the model definitions. Because the mathematical model only considers the effect of flexion rotation, and assumes no anterior shearing occurs, the line of action (which influences the amount of artefact shear force) will not change as long as the flexion angle and L1/L2 ratio are the same. In the ADAMS model, where both flexion rotation and anterior shear may occur, this is not necessarily true. Figure 3-15 demonstrates how the line of action of the compressive force is influenced by how specimen rotation and translation are defined. In this figure, the same L1/L2 ratio is depicted with two different L1 dimension sizes. In the scenario on the left, only translation occurs and thus the smaller L1 (red) results in a line of action with greater artefact shear (y-component). In the scenario on the right, in which only rotation occurs, both the small L1 (red) and large L1 (blue) result in a compressive force with the same line of action and thus artefact shear force. In the ADAMS model, some rotation is permitted in the follower load case, but motion is primarily translational. This gives the result that the ADAMS simulation predicts that the magnitude of L1 has an effect on artefact shearing forces, whereas the mathematical model does not.

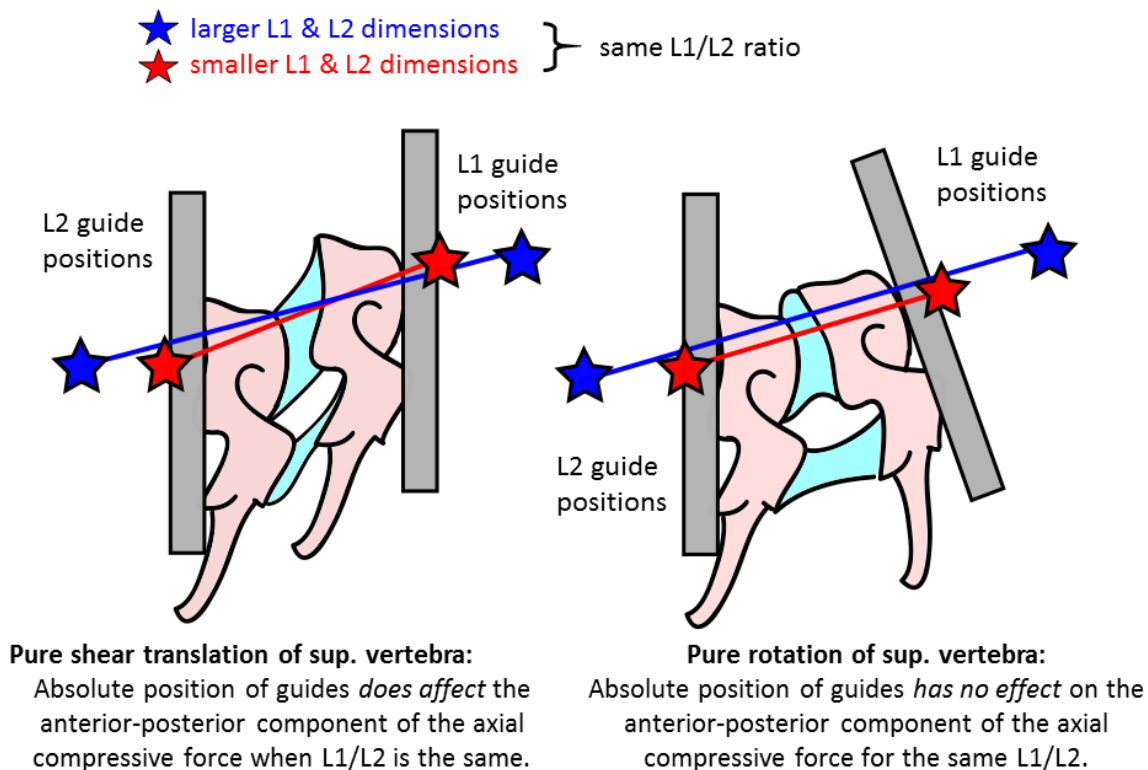


**Figure 3-15: Effect of type of specimen movement and L1, L2 guide positions on artefact shear forces**

This difference between the mathematical and ADAMS models implies that for an anterior shear test scenario, some consideration of the L1 dimension's effect on artefact shear forces could be necessary. In the ADAMS model, it was predicted that larger L1 dimensions within the range simulated resulted in the least amount of artefact shearing forces for a given L1/L2 ratio. Given that this model also predicted that the effect of L1 on artefact moments in the range simulated was small, one might choose to optimize L1 for the reduction of artefact shearing forces (ie. L1=50 mm). Based on the results from the mathematical model, the opposite conclusion would be drawn, suggesting that considering the specific effect of performing anterior shear testing is justified.

While the results from the ADAMS simulations suggest that the selection of the L1 dimension should be optimized towards reducing artefact shearing forces (larger L1), selection of an ideal L1/L2 ratio is not so clearly indicated as a similarly divergent effect on artefact loading is noted in both models. Thus, some judgment as to what an acceptable amount of artefact moment and artefact shearing force might be is necessary in order to select an appropriate L1/L2 ratio. For the purposes of an anterior shear test with axial compression, artefact moments are likely a more critical concern as these artefact loads change the specimen kinematics and load-displacement characteristics. Artefact shearing forces, by contrast, only act to result in a discrepancy between the load that would be measured by a materials testing device load cell and the force that is actually applied to the specimen. Though not ideal, the effect of artefact shearing forces could be managed by incorporating a more advanced materials testing machine actuator control system configuration or by adjusting the materials testing machine load cell measurements in post-processing. Thus, the existence of artefact shearing forces may be less of a concern, especially if relatively small compared to the overall shear load applied to the specimen.

In the context of the present study, a worst-case shear artefact force of 80 N was predicted at the largest L1/L2 ratio simulated at a displacement of 10 mm anterior shear. This artefact represents 5.8% of the applied shear load for the mean stiffness FSU and 24% of the applied shear load for the low stiffness FSU. This might indicate that the selection of a larger (>1.0) L1/L2 ratio is the best practice for an anterior shear test apparatus in the case that a follower load axial compression method is selected. Selecting an  $L1/L2 > 1.0$  acts to reduce the artefact moment at the cost of increasing the artefact shear forces.

With respect to the differences between the results for the various specimens (rubber, mean stiffness FSU, low stiffness FSU), they were less pronounced in the follower load method than in the other axial compression design methods at a compression level of 300 N. Notably,

differences in the amount of artefact load for a given guide configuration were minimal between these three specimens. This is a positive result, as it suggests that the follower load method may be less sensitive to specimen variability in addition to providing reduced artefact moments relative to the other axial compression design methods. Considering that problems encountered in pilot experiments where a point load method was used seemed to occur because of inter-subject variability (ie. mostly affected specimens that were less stiff to a greater extent), selecting an axial compression method that is less sensitive to this might allow for fewer unintended specimen failures.

Some difference was observed in the low stiffness FSU model with respect to flexion-extension rotation. In the low stiffness FSU, some flexion was predicted to occur ( $0.5 - 4^\circ$ ), whereas minimal flexion was predicted in the rubber and mean stiffness FSU models. This amount of flexion rotation would not be expected to cause failure, and would constitute an amount of flexion that would be considered acceptable from an experimental perspective during an anterior shear test.

### 3.5 Summary of Simulation Findings

Using a multibody dynamics model (ADAMS), several different design aspects were investigated in order to determine their effect on artefact loading during anterior shear testing.

Based on these results, key findings were as follows:

1. The follower load method best reduces artefact moments during application of axial compression during anterior shear loading;
2. If a follower load method is used:
  - a larger L1/L2 ratio ( $>1.0$ ) reduces artefact moments and flexion rotations during anterior shear loading;
  - the absolute value of L1 within the ranges tested (30-50 mm) did not have a pronounced effect on artefact moments;
  - it may not be necessary to be concerned with artefact shearing loads at levels predicted herein; thus there is less need to optimize design to reduce them;
3. The point load method may result in large flexion rotation angles and/or instability when larger ( $>300$  N) compressive loads are used in conjunction with more flexible specimens;
4. The rotationally constrained method effectively reduces rotation, but imparts potentially large extension moments on the specimen;
5. To some extent, large flexion-extension moments are inevitable if larger ( $>300$  N) axial compression magnitudes are used.

A more detailed set of recommendations will be provided in Chapter 4, where both the results of the ADAMS simulations and the experimental tests will be considered.

## **4 *Ex-vivo* Validation of Design Analysis**

### **4.1 Purpose**

While the ADAMS model developed in Chapter 3 (Analysis of Shear Test Apparatus Design) is able to provide some useful insights into how test apparatus design decisions influence specimen artefact loading, a number of simplifications and assumptions were made in its development. Considering the definition of the test apparatus in the model, it was, for example, assumed that all parts and forces were perfectly symmetrical about the sagittal plane, and that the compressive force and anterior shearing force were perfectly aligned to the balance point of the specimen. While experimental procedures sought to reduce error in these parameters, achieving the same degree of perfection in alignment in a real specimen is not trivial; the variable geometry tissue properties make locating the precise balance point of a given FSU a challenge. In a real test, this might give the effect that small artefact loads are introduced due to non-ideal alignment of the specimen and loads applied to the specimen. Aspects such as friction in the counterbalance pulley/bearing system and the cable applying the axial compressive force were also neglected in the model.

Another, more substantial assumption that was made in the model was the definition of the specimen itself. In the model, the specimen was defined as a bushing-like joint with 6-directional constant, linear stiffness assignments taken from literature. This definition simplifies the geometry of the specimen to a single point, whereas in a real specimen, there exists more complex interactions between the superior and inferior endplates and the posterior elements. Additionally, because of the variability between specimens and because stiffness in an FSU is likely load-dependent (Chapter 2), using a single constant value may not accurately capture the specimen behaviour during shear loading and compression. Some attempt to check the sensitivity to this parameter was done by simulating a “mean stiffness” and “low stiffness” specimen, however, it is essential that this simplification be verified through physical testing.

Due to various simplifications and assumptions, it is necessary to compare the ADAMS model results to real-world tests. Through verifying certain key simulations with equivalent real-world tests, one could assess to what degree insights provided by the simulation results might be reliable. Based on the original research questions that motivated the test apparatus design analysis, important metrics for the ADAMS simulation model include its ability to predict the relative amount of artefact loading between the different axial compression methods, as well as the numerical accuracy of these predictions. Thus, the purpose of the study presented in this chapter is to verify seven key simulations, using the equivalent test apparatus set-up with the model predictions and comparing them with the results obtained for *ex vivo* porcine FSUs.

Within this, there are two questions of interest:

1. Does the simulation model predict the overall artefact moment trends observed between the axial compression methods in the experimental testing?
2. Are the simulation model predictions for the artefact loads accurate when compared to those measured experimentally for a given axial compression method?

For the purposes of the experimental verification, the focus was narrowed to the effect of axial compression method on artefact flexion-extension moments and rotations, and the effect of 3 different L1/L2 follower load guide ratios on these parameters. These specific outcomes were selected because the simulation predictions suggested that these parameters would have the greatest influence (and thus, potential for improvement) on specimen loading and kinematics.

## 4.2 Methods

Four fresh-frozen porcine FSUs (C7-T1, T2-T3; C4-C5, C6-C7) were dissected from two Yucatan pigs. The posterior elements were removed as the morphology of the facet joints in the pig are not readily comparable to those in a human. The specimens were prepared in a manner identical to that described in Chapter 2, excepting the removal of the posterior elements.

Seven key simulations from the larger array of ADAMS simulations were selected for comparison against experimental tests. All seven tests were performed on each specimen, where the order in which tests were performed was alternated for each specimen. These tests were as follows:

1. Unconstrained (6 dof) shear, no axial compression
2. Unconstrained point load (6 dof), with axial compression
3. Rotationally constrained (2 dof), no axial compression
4. Rotationally constrained (2 dof), with axial compression
5. Follower load (6 dof), with axial compression
  - a. L1/L2=50/85 mm
  - b. L1/L2=50/50 mm
  - c. L1/L2= 50/15 mm

. A compressive load of 300 N was used for all trials for Pig 1 (C7-T1, T2-T3) and the rotationally constrained trials for Pig 2 (C4-C5, C6-C7). A compressive load of 150 N was used for the unconstrained trials (2, 5a-c) for both Pig 2 specimens. This was done because some difficulty was encountered in achieving stable initial alignment of the 300 N axial compressive force in the C4-C5 specimen when rotation was not constrained. For consistency, the same protocol was used on the C6-C7 specimen from this same porcine donor, though this specimen did not demonstrate the same level of instability.

Test apparatus set-up was similar to that described in Chapter 2. The existing shear test apparatus was modified slightly to allow for the measurement of 6-axis loading at the fixed (inferior) vertebra, and to enable the three different axial compression methods.

An MCA-6-500 6-axis load cell (AMTI, Watertown, MA, USA) was installed between the inferior loading plate of the specimen and a rigidly secured mounting frame (Figure 4-1). It was mounted such that the true axes of the load cell were collinear to those of the specimen, and such that the z-axis (compression) of the load cell was aligned with the superior-inferior axis of the specimen. Photographs of the experimental set-up may be found in Appendix I.

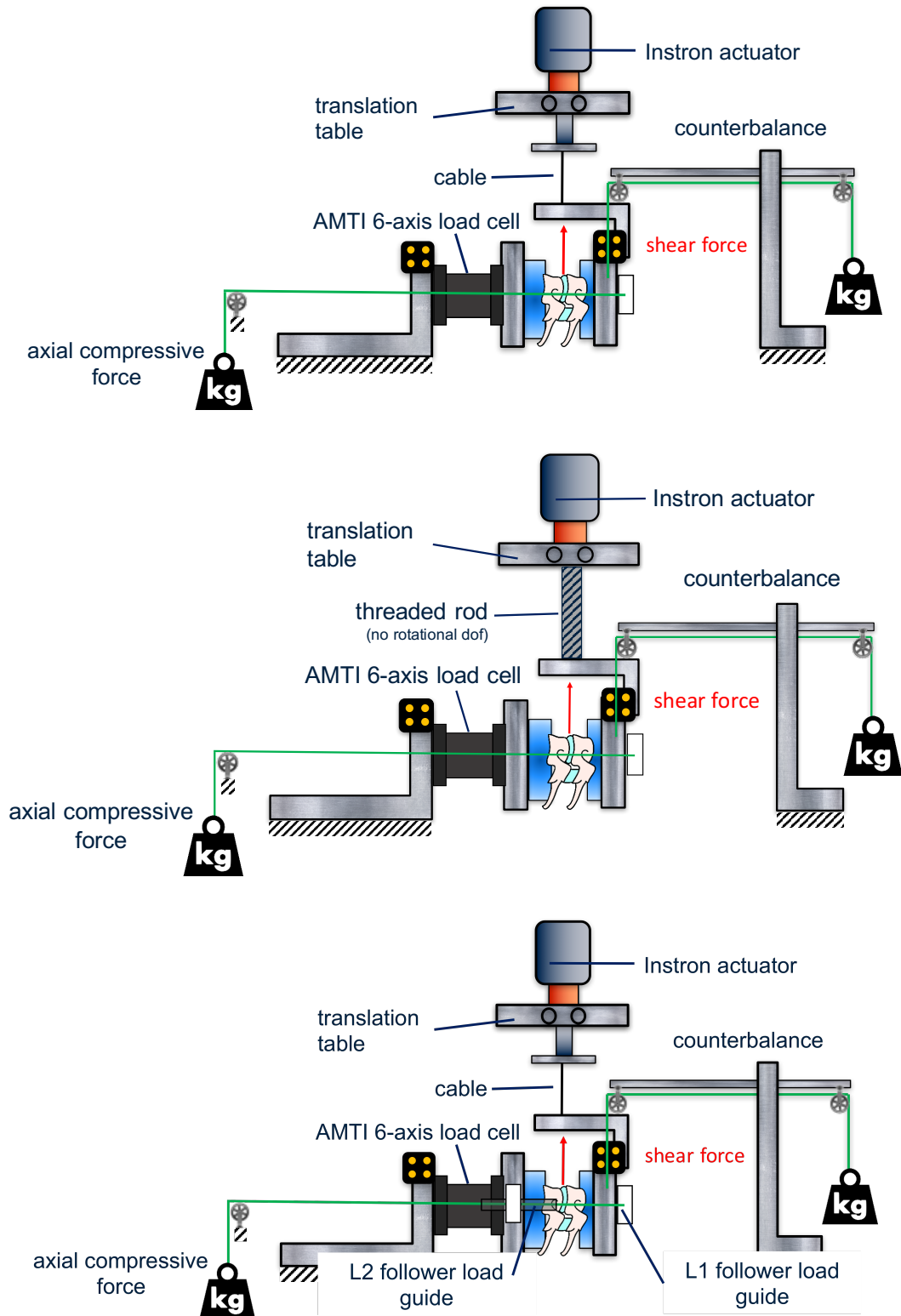


**Figure 4-1: Test Apparatus set-up for verification tests – point load (top), rotationally constrained (middle), follower load (bottom)**

For the point load compression method, the existing deadweight/pulley system was used to apply the axial compressive force. For the follower load method, the same deadweight/pulley system was used, but with the addition of two laterally paired adjustable guides at the inferior vertebra (Figure 4-1, “L2 follower load guides”). These enabled the adjustment of the L2 parameter in the inferior-superior direction, and the anterior-posterior direction (to align the guide at the “balance point” causing no flexion-extension rotation). These guides were only used for the follower load tests, and were otherwise removed from the mounting frame. The existing mounts on the superior loading plate were used as the L1 follower load guide. Additional mounting points were added along the inferior-superior axis of the loading plate to allow for adjustment of the L1 parameter. Because all verification experiments involved an L1=50 mm, adjustment was only necessary due to deviations in specimen size. A single L1 was chosen as the ADAMS model predicted that effect of varying L1 on specimen artefact moments was minimal (ie. unlikely to measurable experimentally).

For the rotationally constrained method, the cable was replaced with a threaded rod, which limited all rotational degrees of freedom. Shaft clamps were used on the translation table to limit translation. Axial compression was applied using the deadweight/pulley system, as in all other tests. Superior-inferior translation of the translation table was allowed during tests with axial compression, as in the ADAMS simulations, to ensure a constant axial compressive force.

Each trial involved 5 cycles of anterior shear loading corresponding to 3.0 mm at a loading rate of 0.5 mm/s. A displacement control protocol was chosen for both the simulations and experimental verification tests to facilitate a more straightforward comparison between the ADAMS simulations and the experimental test. Kinematics and load cell data were analyzed from the third cycle of each test, at an anterior shear displacement of 1.5 mm and 3.0 mm, as measured by the Instron LVDT. The protocol of analyzing the 3<sup>rd</sup> of 5 cycles was developed as described in Chapter 2, where it was found that the load-displacement behaviour during cyclic

loading became reproducible after the 2<sup>nd</sup> cycle. Though the simulations involved loading to 10 mm, a maximum shear displacement of 3.0 mm was chosen for the experimental tests to ensure that no specimen failure occurred, enabling each specimen to be tested in all axial compression method configurations.

Because of differences in laxity between the unconstrained (cable) and constrained (threaded rod) test apparatus set-ups, the LVDT anterior shear displacement was not necessarily equal to the local specimen anterior shear displacement. The LVDT measurement was used only to ensure that the points being analyzed for each test were from the same time in the loading cycle (ie. 50% and 100% anterior shear cycle).

Local, specimen 3D kinematics at the time of the specified LVDT readings were obtained from the two Optotrak rigid body markers mounted on the fixed (inferior) and shearing (superior) vertebra. The method used to define the anatomical coordinate system was as described in Chapter 2. The coordinate system was defined as anterior - +y, superior - +x, left - +z, in accordance with the coordinate system used in ADAMS. Load cell measurements from both the Instron load cell (uniaxial) and the six-axis load cell were considered at this same time instant.

The Instron load cell data and Optotrak data were collected at 125 Hz, and synchronized using an ODAU (Optotrak Data Acquisition Unit). The six-axis load cell data was collected at 1.25 kHz using a NI DAQ-9172 (National Instruments, Austin, TX, USA), which was subsequently down-sampled to 125 Hz for analysis purposes. Data collection from the two DAQs was synchronized using the leading edge of a 5 V DC open circuit analogue trigger, initiated in the first 5 seconds of each test. Agreement between the signals was verified by comparing the shear force signals from the Instron load cell (ODAU) and the six-axis load cell (NI DAQ).

Raw voltage data from the six-axis load cell was transformed into N and Nm using the 6x6 calibration matrix specified by the manufacturer (Appendix F). During data analysis, all channels

were set to zero at time 0 to remove the effect of any transient loading that existed prior to the beginning of the loading cycles (eg. mass of specimen and plates supported by the 6-axis load cell). The calibration matrix was verified by applying a 70 N compressive load (load cell z-axis), and was found to be accurate within <1 N. For the purposes of comparison to the ADAMS simulations and mathematical model, loads measured by the 6-axis load cell were transformed to that of the superior (loading) vertebra. In the experimental set-up, the 6-axis load cell was aligned to the inferior (fixed) vertebra's coordinate system. Because the rotations of the two vertebral coordinate systems relative to each other were small (<2.6°) during all experimental tests, the differences between the measured and reported (transformed) loads were negligible (<0.01 N or Nm).

All data analysis was performed in Matlab. A zero-lag 4<sup>th</sup> order low pass Butterworth filter with a cut-off frequency of 5 Hz was applied to the raw 6 axis load cell data, Instron load cell data and Optotrak position data in Matlab. The manufacturer calibrations for each load cell were verified using known masses in the load cell z-direction. The Instron load cell was accurate within <3.2 N for a 23.9 N mass, while the 6-axis load cell was accurate within <1.0 N for a 35.0 N mass. Linear regression analysis (regression coefficients, standard error,  $R^2$ ) was performed in Matlab using the linear regression function "fitlm".

In the present results, two outlier test runs were excluded: the follower load L1/L2=50/85 and the follower load L1/L2=50/50 trials for specimen Pig 2 C4-C5. In these tests, the specimen moved into a position of 5-10 ° extension in the first cycle, and remained in that position regardless of Instron loading. In all other tests that preceded and followed these two trials, axial compression was applied without causing large rotations. This specimen was noted subjectively to be quite flexible. No loading cycle hysteresis (which might indicate damage) was noted in subsequent tests.

## 4.3 Results

### 4.3.1 Overall Loading and Kinematics

Experimental loading and kinematics measurements were found to be the most comparable to the ADAMS simulations predictions made using the low stiffness FSU model. As such, all comparisons presented herein will be to the simulation predictions from this specimen model. As described in Section 4.2 (Methods), laxity in tests involving the cable connection (point load, follower load) resulted in some difference between the prescribed 3.0 mm peak anterior displacement and the local specimen peak anterior shear displacement, as demonstrated by the results from Fig 1, C7-T1 (Table 4-1). This effect was not apparent in the rotationally constrained tests, and so results at 50% (1.5 mm) and 100% (3.0 mm) of the anterior shear cycle are not directly comparable between different tests.

**Table 4-1: Sample comparison of low stiffness simulation outputs to experimental results at peak applied anterior shear displacement (3.0 mm) for Fig 1, C7-T1**

	Instron force [N]	Axial compr. [N]	Artefact posterior shear [N]	Inferior displ. [mm]	Anterior displ. [mm]	Flexion(+) Ext. (-) rot. [°]
<b><i>Point load</i></b>						
Simulation	89	300	0	0.34	3.0	2.3
Experimental	62	271	18	0.31	1.8	0.6
<b><i>Rotationally constrained</i></b>						
Simulation	87	300	0	0.23	3.0	0
Experimental	86	271	23	0.42	2.6	-0.2
<b><i>Follower load (L1=L2=50 mm)</i></b>						
Simulation	93	252	11	0.26	3.0	1.3
Experimental	58	271	16	0.37	1.8	0.4

This anterior shear displacement discrepancy occurred due to laxity in the test apparatus, and mostly affected tests where the cable connection was used (point load and follower load tests). This laxity resulted in a discrepancy between the total displacement of the

specimen and the Instron LVDT reading of 0.0-0.4 mm for the rotationally constrained tests (solid beam connection) and 0.4-2.0 mm for the point load and follower load tests (cable connection). For this reason, the ADAMS model overestimates the shearing force applied by the Instron in the point load and follower load tests relative to experimental results. In the rotationally constrained tests, where the local anterior shear displacement was closer to 3 mm, better agreement between the simulated and experimental results is seen (1.4 N difference).

There were some differences in the experimentally measured axial compressive load magnitude and component breakdown and what was predicted by the ADAMS model. In the experimental results, an axial compressive load of 270-272 N was measured along the compressive axis of the 6-axis load cell, instead of the expected ~300 N load. It would be expected that the compressive force measured at the 6-axis load cell be near 300 N as a deadweight was used to apply the axial compressive force.

A difference of ~10-20 N between the anterior shear loads measured at the 6-axis load cell and the Instron load cell was also noted in all tests, with greater discrepancies occurring in the point load and rotationally constrained tests. In theory, this might indicate the presence of artefact shearing forces. In Table 4-1, it is assumed that these differences between the anterior shear force measurements at the two load cells are a result of artefact shearing forces created by the axial compression force. In the ADAMS simulations, no artefact shearing forces are predicted except when a follower load is used.

#### **4.3.2 Artefact Flexion-Extension Moments during Different Axial Compression Methods**

Flexion-extension moments measured experimentally with the 6-axis load cell were found in most cases to have good numerical similarity to those predicted in the low stiffness FSU model for a given axial compression method (Figure 4-2, Table 4-2).

Figure 4-2 shows linear regressions of the artefact moments measured for each axial compression method, using the flexion-extension moments measured at an Instron LVDT displacement of 0, 1.5 and 3.0 mm for all trials (n=12 data points for each method, excepting follower load L1/L2 50/50 and 50/85 where n=9 ). In this figure, the anterior shear displacements plotted along the x-axis reflect the local specimen kinematics at the previously specified LVDT displacements, as measured by Optotrak. The corresponding continuous ADAMS simulation results for each axial compression method are represented in this figure (dashed lines).

As demonstrated by the  $R^2$  values and standard errors associated with each linear regression (Table 4-2), the experimental data showed good linearity in most cases. In those tests where lower flexion-extension moments were measured (ie. no axial compression tests, larger L1/L2 value follower load tests), more variability in the experimental data was observed.

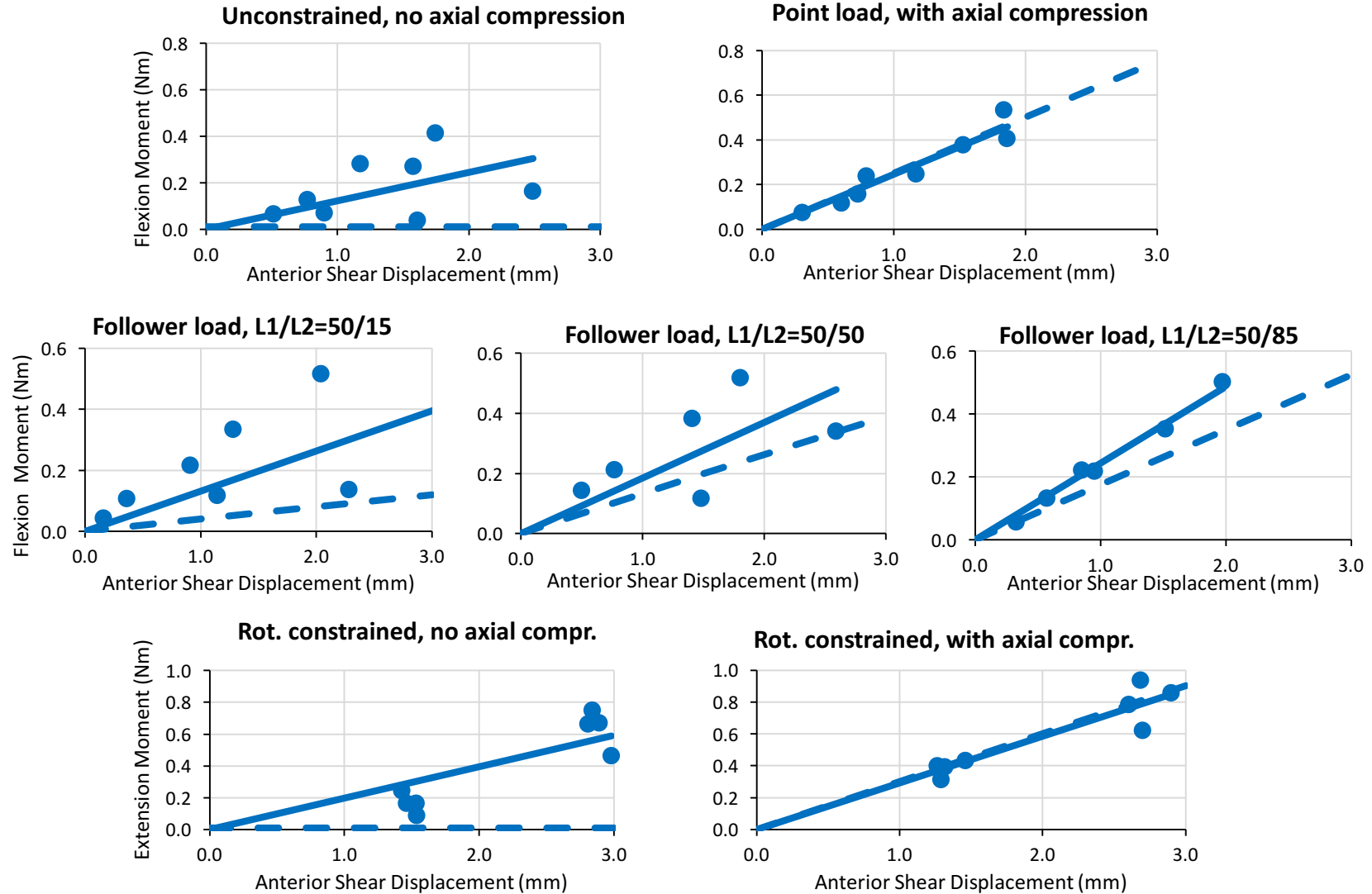


**Figure 4-2: Comparison of experimental data (dots) with linear fit (solid line) and simulation (dashed line) artefact flexion-extension moments during anterior shear testing**

**Table 4-2: Regression coefficients, Standard Error and R<sup>2</sup> for linear fit of experimental artefact moment measurements**

<b>Compression method</b>	<b>Regression coefficient* (Nm/mm)</b>	<b>Standard Error (Nm)</b>	<b>R<sup>2</sup></b>
<i>Rotationally constrained</i>	0.29	0.01	0.85
<i>Point load</i>	0.25	0.01	0.91
<i>Follower load, L1/L2=50/85</i>	0.24	0.007	0.98
<i>Follower load, L1/L2=50/50</i>	0.16	0.03	0.57
<i>Follower load, L1/L2=50/15</i>	0.13	0.03	0.55
<i>Unconstrained, C=0</i>	0.12	0.03	0.28
<i>Rotationally constrained, C=0</i>	0.20	0.02	0.50

\*linear regressions determined using a y-intercept of 0 Nm

Considering the values of the linear regression coefficients (Table 4-2), the simulation predictions for the relative amount of artefact moment caused by each axial compression method were quite similar to those measured experimentally. The simulation predicted the rotationally constrained method would create the most artefact moment compared with the other axial compression methods, which was the same as was measured experimentally. The simulation predicted follower load method would create the least artefact moment, with the largest L1/L2 ratio (L1/L2=50/15) providing the greatest reduction. This was the order demonstrated experimentally, though the difference between the smallest L1/L2 ratio (L1/L2=50/85) and the point load were nearly indistinguishable.

The numerical outputs from the simulations for artefact moments agreed well (<10% error) for the point load method and the rotationally constrained method. In the follower load method, experimentally measured artefact moments were larger than those predicted by the model simulations.

In tests where no compression was applied (unconstrained and rotationally constrained), measured artefact moments were found to be non-zero experimentally. In the simulations, no artefact moments were predicted in absence of an applied axial compressive force. In the case of the unconstrained, no compression tests, these measured artefact moments were the lowest of any axial compression method used in the test apparatus. In the case of the rotationally

constrained, no compression tests, artefact moments were measured to an extent that was similar to those measured in the follower load L1/L2=50/50 case.

### **4.3.3 Flexion-Extension Rotations**

Flexion-extension rotation angles measured experimentally did not correspond well with the simulation predictions in the tests without rotational constraint (Figure 4-3). Experimentally, flexion-extension angles were found to be relatively constant with respect to both increasing anterior shear displacement and with respect to the different axial compression methods. This is evidenced by the weak  $R^2$  values for the linear fits of this data across all axial compression methods, excepting the point load method (Figure 4-3). In general, experimental flexion-extension rotations were small ( $<2.6^\circ$ ). In the rotationally constrained tests, minimal rotation was observed ( $\pm 0.5^\circ$  max).

In the ADAMS simulations, the amount of flexion-extension rotation predicted for the unconstrained tests (point load, follower load) was in accordance with the predicted trends for flexion-extension moments (ie. larger flexion-extension moments were correlated with larger flexion-extension rotations). This was not observed experimentally.

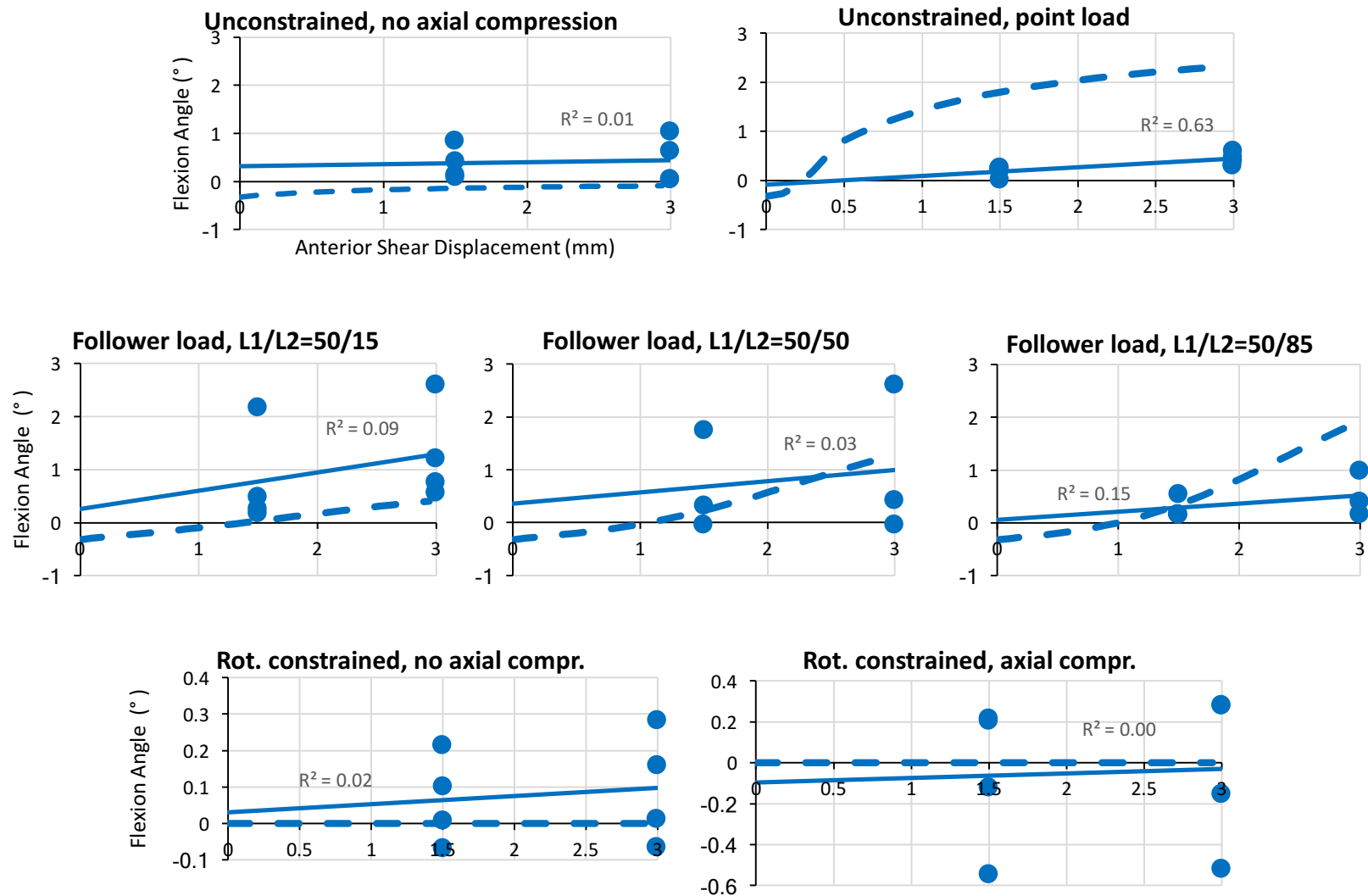


Figure 4-3: Comparison of experimental data (dots) with linear fit (solid line) and simulation (dashed line) flexion-extension rotation during anterior shear testing

In terms of numerical similarity with the simulation predictions, some differences were noted. While the range of flexion-extension rotations found between the experimental measurements and simulation predictions were similar (0-2.6 ° for the unconstrained simulations at 3.0 mm anterior shear with 300 N compression), the rotational response to increasing anterior shear between the two models was somewhat different. In the unconstrained simulation tests with the low stiffness FSU specimen definition, flexion-extension response to increasing anterior shear displacement was found to be non-linear for the point load method (similar to a square-root function). In the other specimen types (rubber, mean stiffness FSU) a linear response was noted. In the experimental measurements, the response to increasing anterior shear is relatively constant to weakly linear up to 3.0 mm. Thus, while the numerical predictions from the model appear similar to the experimental results at 3.0 mm, the model did not predict flexion-extension rotation behaviours accurately throughout the entire test.

However, the experimental results did demonstrate that the test apparatus configuration for the rotationally constrained tests was able to limit specimen flexion-extension.

#### **4.4 Discussion**

The main finding from the *ex vivo* experimental verification was that the previously developed ADAMS model was able to estimate the effect of the different axial compression methods to a degree sufficient to provide insight for design purposes. The two metrics for assessing the usefulness of the ADAMS model were its ability to predict the relative differences (or relative performance) of each of the selected axial compression methods, and the numerical accuracy of its outputs. Acknowledging that the simulations involved a number of assumptions and idealized force and part definitions, a higher priority was placed on the model's ability to predict the relative trends that existed between the axial compression methods. In this regard, the ADAMS model was quite successful, particularly in the area of predicting trends within the different axial compression methods (Table 4-3).

**Table 4-3: Comparison of findings from shear test simulations and experimental results**

<b>Agreement between simulations and experimental results</b>	<b>Disagreement between simulations and experimental results</b>
<ul style="list-style-type: none"> <li>• Relative differences between each of the compression methods</li> <li>• Follower load L1/L2=50/15 results in the least artefact moment</li> <li>• Magnitude of artefact moments in point load and rotationally constrained tests</li> <li>• Magnitude of flexion-extension rotations during anterior shearing</li> </ul>	<ul style="list-style-type: none"> <li>• In “baseline” tests without axial compression, some artefact moments were measured</li> <li>• Model underestimation of artefact moments in follower load tests</li> <li>• Experimentally, negligible difference between point load and L1/L2=50/85 follower load</li> <li>• Relative amount of flexion-extension rotations between the different axial compression methods</li> <li>• Experimentally, artefact shearing forces were measured in all tests</li> </ul>

Another major finding was that the model was able to predict the relative amount of artefact shear caused by the use each axial compressive method and had reasonable agreement in terms of order of magnitude of these loads. This would suggest that the presently developed ADAMS model is an appropriate tool for estimating the effects of different axial compression methods on artefact moments experienced by cadaveric FSUs during shear loading. Some caution would be recommended when extrapolating larger axial compression forces and shear displacements nearer the failure threshold, as these magnitudes of loads and displacements were not verified experimentally. It might be expected that the model predictions become less reliable at these larger magnitude loads and displacements due to simplifications inherent in the definition of the model definition of the cadaveric FSU, namely the use of linear stiffness properties. Though ideally, non-linear, load-dependent shear stiffness properties would have been implemented for the cadaveric FSU specimen models, no such published experimental data exists for the cervical spine.

Though there were some differences between what was predicted by the model simulations (Table 4-3), the differences observed can largely be explained by some of the assumptions and idealizations that were inherent in the model. These differences are important, as they provide some insight into aspects of the apparatus design or methodology that may require some additional consideration in order to be implemented more ideally in a practical scenario.

Although the simulations correctly predicted the relative order in amount of artefact moments caused by each axial compression method, it did not predict any artefact moments in absence of an axial compressive force. Experimentally, some artefact moments were measured in the unconstrained and rotationally constrained tests without compression. This might be explained by the morphology of the cadaveric FSU, where the geometry of the endplate is somewhat curved in the sagittal plane. During anterior shearing, some contact between the two curved endplates might occur, potentially resulting in the generation of a flexion-extension moment. This effect would likely be more pronounced when rotation is constrained. In the simulations, the FSU was modeled as a bushing-like joint, which did not consider the effect the internal geometry of a specimen might have on kinematics and loading.

Similarly, the artefact moments were underestimated by the model relative to experimental results in all but one results set (rotationally constrained, with compression). Considering the small difference between the unconstrained test artefact moments (baseline) and the follower load test artefact moments, it might be concluded that this discrepancy may be related to specimen geometry, or small misalignments that were consistently present during testing. Despite the measured moments being larger than predicted by the model, moments measured during the follower load tests still provided a relative reduction in artefact moments as compared to the other axial compression methods. An additional consideration in this regard is that due to the low magnitude of loads expected for some tests that some noise would be expected experimentally, given the capacity of the load cell used (56 Nm).

Interestingly, it was found that the point load method and the smaller L1/L2 ratio follower load method (50/85) resulted in nearly identical artefact moment linear regression curves. Theoretically, one can consider the point load method to be a special case of the follower load method, where the L2 guide position is at infinity. Experimentally it is impossible to have a guide positioned at infinity and so the test apparatus uses a pulley at some sufficiently large distance from the specimen. In the present experimental set-up, this pulley is located ~1 m from the specimen centre. This result suggests that in a practical scenario (in which a pulley positioned at  $\infty$  is not possible), that an L2 follower load guide position closer than 85 mm should be used in order to obtain substantial reduction in artefact moment from the point load method.

Despite good agreement between the magnitude and relative amount of artefact moments measured experimentally and simulation predictions, differences were noted in the measured flexion-extension rotations. It was expected from the simulations that a similar trend to that which occurred with artefact moments would occur in the unconstrained tests for flexion-extension. The opposite trend was measured experimentally; the follower load method trials resulted in the largest flexion-extension rotations. This result is interesting as this trend occurred in spite of the follower load method resulting in reduced measured artefact flexion-extension moments.

This result may reflect some of the serendipity involved in aligning the axial compressive force and follower load guides in the superior-inferior axis in specimens. Because the follower load method requires one to correctly align four guides to the superior-inferior centre of the specimen, there is more opportunity for slight errors in positioning to accumulate. Additionally, when the guides are closer to the specimen (ie. L1/L2=50/15), small angular errors in superior-inferior alignment are magnified to a greater extent. While minor (<0.5 mm) differences in alignment of the superior and inferior guide positions may not have a substantial effect on

measured moments, more flexible or unstable specimens may be sensitive to these differences and thus rotate more.

This is supported by observations from tests involving P2 C4-C5 (the smallest specimen, qualitatively unstable), in which extreme difficulty in aligning the axial compressive force prior to the beginning of the loading cycles was noted. Despite positioning all four guides in the same superior-inferior locations during all follower tests, two trials (L1/L2=50/85, 50/50) were discarded due to the specimen moving into, and becoming stuck in extension shortly after the beginning of the first cycle (Figure 4-4). All other unconstrained trials proceeded successfully (ie. small rotations, motion primarily occurring in the anterior shear direction) with this same positioning, and problems of this nature were not experienced outside of this particular specimen. This may indicate that some additional consideration in either methodology or precision of guide design may be necessary to ensure repeatable results in less stable, smaller specimens.

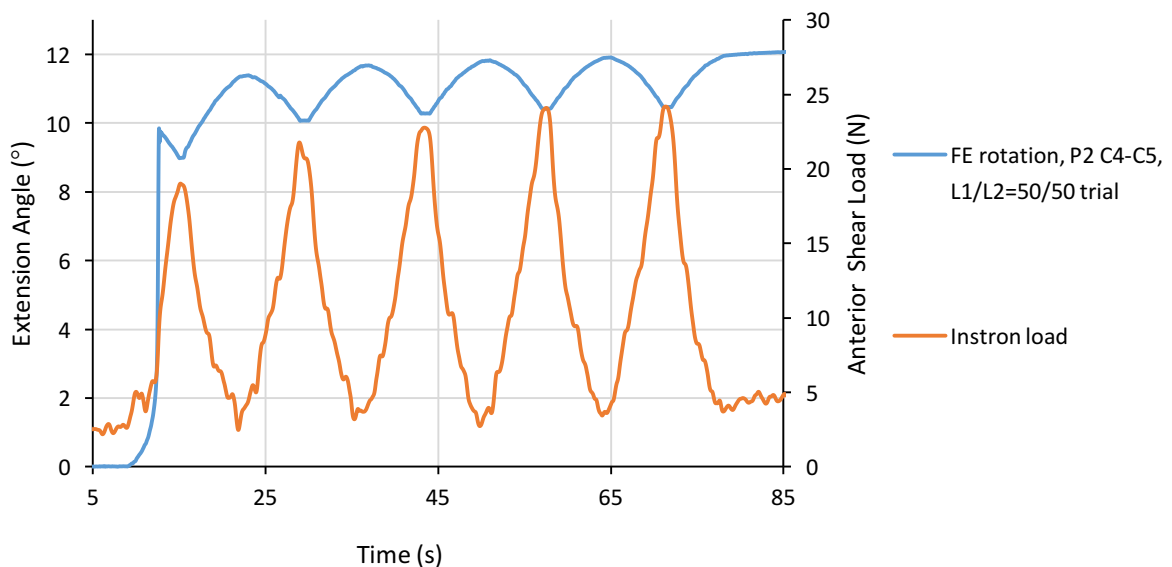


**Figure 4-4: Flexion-extension rotation during application of anterior shear load in omitted trial**

Finally, as noted in Table 4-3, artefact posterior shear loads were measured during all tests. In the simulations and mathematical models for the various axial compression methods, no artefact shearing loads were predicted unless a follower load was used. This is because in theory, in the point load method and the rotationally constrained method, the line of action of the axial compressive force is body-fixed to the specimen. This means that the line of action of the axial compressive force should only exist along the superior-inferior axis of the specimen and have no anterior-posterior component. In the experimental results, a consistent ~10-20 N discrepancy between the anterior shear loads measured by the Instron load cell and 6-axis load cell were noted that could not be fully explained by inaccuracy in load cell calibration. These discrepancies may indicate that there is an issue with the alignment of the cable relative to the specimen inferior-superior axis that was common to all the axial compression methods. In the current test apparatus configuration, the most likely cause of this would be the position of the pulley in the deadweight system, which was employed in all axial compression configurations. The inferior-superior position of the pulley was not adjusted specifically for each test, and so small angular deviations from the true specimen inferior-superior axis could have contributed to the existence of small artefact shearing forces in all tests. In the future, fine-tuned adjustment of this pulley position should be considered.

It was also noted that there was some discrepancy between the applied deadweight mass (300 N) and the magnitude of the measured axial compressive force (~270-272 N). This discrepancy may have been caused by friction in the pulley-deadweight system. In the present design, the cable applying the axial compressive force has several points of contact with the superior guides (all compression methods), the inferior guides (follower load method) and the frame of the test apparatus (all compression methods). Though this overall effect was consistent between all tests, it would be desirable to have the compression load be as close as possible to what was prescribed. This could be addressed through the implementation of more low-friction

contact points (ie. linear bearings, pulleys) in the guides or on the frame of the test apparatus at points of contact.

Though these limitations in the experimental set-up likely contributed to the discrepancies observed between the experimental results and simulations, the influence of the discrepancies between the results on the conclusions one might draw from each results set is small (provided in Section 4.5, to follow). Based on the relative amount of flexion-extension artefact loading caused by each axial compression method/configuration, the same conclusion might be drawn from both the simulations and experimental work with regard to best practices.

That said, these discrepancies between the idealized simulation set-up and the experimental results highlight areas that could be improved in the experiment set-up or testing methodology. Idealized features of the simulation such as the perfect alignment of forces, no friction etc. represent the configuration that results in the lowest possible amount of artefact moment and artefact shear, and so this configuration should be emulated as closely as possible in an experimental set-up. Considering the discrepancies noted, the following changes in apparatus design or test methodology are recommended:

- Fine-tuned superior-inferior adjustment of distal pulley in axial compression system (use laser level to ensure wire is horizontal before each test)
- Reduced friction between axial compression wire and test apparatus at all contact points
- Modification to Instron loading protocol for shear tests involving cable connection (ensure that local specimen shear displacement can be prescribed predictably)

## 4.5 Design Recommendations

Based on the results from the ADAMS model simulations and the subsequent experimental verification results presented herein, a number of design recommendations for the implementation of axial compression in a shear test apparatus for cadaveric FSUs can be formulated. These recommendations aim to address experimental problems that were previously encountered in some cadaveric specimens when applying such loading during anterior-posterior shear testing, where large, undesirable flexion-extension rotations were noted during testing.

- If an unconstrained configuration is desired, a follower load axial compression method should be selected to minimize both flexion-extension moments and rotations
- If a follower load method is selected, a large (>1.0) L1/L2 superior: inferior guide ratio should be selected to minimize artefact moments; minimizing artefact shearing forces is less critical
- Using a rotationally constrained axial compression method may be a viable solution for reducing flexion-extension rotation, but will result in relatively large artefact extension moments during anterior shear loading
- Regardless of axial compression method chosen, large artefact flexion-extension are inevitable if either large compressive forces or large shear displacements are prescribed
- Any design should incorporate features to minimize friction within the axial compression cable system and ensure precise alignment of the cable relative to the specimen inferior-superior axis

It should be noted that when considering these recommendations, acknowledgement of the experimental application should be taken into account. The specific application or research

objective of any shear testing in the cervical spine may dictate to some extent which test apparatus design criteria (eg. allowance of rotation, amount of axial compression, importance of reducing artefact moments etc.) should be prioritized.

## 5 Conclusion

In this thesis, two primary research objectives were proposed in order to address gaps that were identified in the current understanding of the biomechanics of the cervical spine:

1. What is the load-displacement behaviour of the human cervical FSU during pure shear loading?
  - a. What is the effect of progressive removal of the posterior elements on the shear biomechanics?
  - b. What are the load-displacement characteristics in each shearing direction?
2. What is the effect of axial compression on specimen artefact loading, and how can design features be used to reduce them during shear testing while still applying physiologically relevant loads?
  - a. What are the effects of different design methods on artefact moments and coupled rotations over a range of physiological axial compression methods?
  - b. If guides are implemented to position the axial compressive force, what effect does their positioning have on artefact loading and coupled rotations?

These two research objectives were addressed successfully through an *ex vivo* human cadaveric study (Chapter 2, objective 1) and the development of a multibody dynamics model (Chapter 3, objective 2), with experimental validation using a porcine model (Chapter 4, objective 2). With regard to objective 1a, it was found that the bony posterior elements contribute significantly to the shear stiffness of the cervical FSU in anterior-posterior direction, but not in the lateral direction. This finding may have implications for the definition and validation of FSUs in a modeling context, as well as for applications such as implant design. Similarly, for objective 1b, the finding that stiffness was to some extent displacement-dependent even at lower loading ranges (ie. distinct between 0-20 N and 20-100 N), and that the shear stiffness

responses varied depending shearing direction might justify using more complex modeling definitions of the shear properties of the cervical spine. With regard to objective 2, it was found that (using both computational and experimental methods) that using a follower load axial compression design with a smaller L1/L2 ratio provided the best compromise of reducing artefact moments and artefact shearing loads during testing. This may suggest that further pursuit of this less common design method might be justified in experimental work, allowing for more biofidelic shear testing experimental work to be carried out. In successfully addressing each of these specific research objectives, the overall research objective of improving the understanding of the behaviour of the cervical spine during shear loading for the purposes of improved injury modeling was met.

Key contributions from this work include the determination of the shear stiffness and kinematics of the cervical FSU at higher shear loading magnitudes, as well as an analysis of how different axial compression method design parameters might be optimized for the specific application of shear testing of the cervical spine.

These contributions may be of use for subsequent mechanical testing of the cervical spine, where findings from this thesis may facilitate the methodology and test apparatus design of future studies involving shearing loads. In order to have a better understanding of the role of cervical shearing loads in traumatic SCI, future studies will need to investigate parameters such as failure thresholds, the influence of more realistic (dynamic) loading rates, as well as the effect of combined loading (eg. axial compression and shear loading) in both the FSU and multi-segment models. The findings presented herein may provide experimenters undertaking this work with guidelines upon which to establish experimental methodology and design, as well as a reference point for the basic shear properties of cervical FSU.

The contributions from this work may also be of use to experimenters developing mechanical surrogate models and computational models of the cervical spine. Such models require both parameters to define the model (such as stiffness, failure threshold etc.) as well as

detailed datasets (input and output data) for model validation. The work presented in Chapter 2 may be of use for both purposes, while the work presented in Chapter 3 may provide some additional context to existing and future experimental work (ie. consideration of effect of different boundary conditions imposed in experiments during validation).

Although work in this thesis provides a much-needed basic understanding of certain aspects of cervical biomechanics testing, there were some experimental limitations. Small sample sizes in Chapters 2 meant that it was not possible to account for inter-specimen variability (eg. spine level) or subject-specific intrinsic parameters (eg. age, body mass, sex, BMD, disc or facet degeneration). These factors may be important to consider, especially for the development of injury criteria that aim to establish risk for diverse populations. Because these factors were not accounted for, and because of the small sample size, the findings presented may not be entirely representative of the general population.

For the analysis of shear test apparatus design (Chapters 3 & 4), the limitations included the simplistic specimen definition in the simulations, where the specimen was defined by average cervical FSU stiffness values. This gave the result that there was good agreement for the general, relative effect of different design choices on artefact loads between the simulations and experimental results, but disagreement on the kinematics (eg. flexion rotation) as a result of these loads. This means that for the purposes of informing design decisions, using *only* the kinematics outputs from the simulations (as defined herein) may not be prudent, as the real-world variability between specimens makes this output less predictable experimentally. A second limitation of this aspect of this thesis was the difficulty in replicating the idealized simulation set-up experimentally (eg. perfect alignment of specimen relative to applied loads, laxity in cable applying shear load). Though this limitation likely had a minimal influence on the design recommendations inferred from the results, it does highlight the importance of considering these aspects very carefully during protocol development and apparatus design.

Overall, the strength of the work in this thesis is the provision of a basic understanding of the biomechanics of the spine in an area that has not received much attention historically, but that is emerging as an area that might be important to the interest of reducing traumatic SCI. It is hoped that the work presented herein will provide some foundation for continued studies on the shear biomechanics in the cervical spine, and contribute to the development of more advanced injury models of the spine. With this, prevention of a greater number of SCI events might be possible through an improved ability to use modeling to assist in the design of safety devices or protective equipment.

## References

- Barker, J., Cronin, D., & Nightingale, R. (2017). Lower cervical spine motion segment computational model validation: kinematic and kinetic response for quasi-static and dynamic loading. *J Biomech Eng*, 139(6), 061009.
- Begeman, P., Visarius, H., Nolte, L., & Prasad, P. (1994). Viscoelastic shear responses of the cadaver and Hybrid III lumbar spine. *SAE Technical Paper 942205*.
- Berkson, M., Nachemson, A., & Schultz, A. (1979). Mechanical properties of human lumbar spine motion segments - part II: responses in compression and shear; influence of gross morphology. *J Biomech Eng*, 101(1), 53-57.
- Brault, J., Siegmund, G., & Wheeler, J. (2000). Cervical muscle response during whiplash: evidence of a lengthening muscle contraction. *Clin Biomech*, 15(6), 426-435.
- Buckwalter, J. (1995). Aging and degeneration of the human intervertebral disc. *Spine*, 20(11), 1307-1314.
- Crandall, J., Bose, D., Forman, J., Untaroiu, C., Arregui-Dalmases, C., Shaw, C., & Kerrigan, J. (2011). Human surrogates for injury biomechanics research. *Clin Anat*, 24, 362-371.
- Cripton, P., Bruehlmann, S., Orr, T., Oxland, T., & Nolte, L. (2000). In vitro axial preload application during spine flexibility testing: towards reduced apparatus-related artefacts. *J Biomech*, 33, 1559-1569.
- DeWit, J., & Cronin, D. (2012). Cervical spine segment finite element model for traumatic injury prediction. *J Mech Behav Biomed Mater*, 10, 138-150.
- Doodkorte, R., Melnyk, A., Dowling-Medley, J., Groenen, K., Cripton, P., Oxland, T., & Verdonschot, N. (2016). *Quasi-static shear biomechanics of the lower cervical spine (MSc thesis)*. Radboud University Medical Centre, Orthopaedic Research Laboratory, Nijmegen, the Netherlands.
- Drake, R., Vogl, W., & Mitchell, A. (2012). *Gray's Basic Anatomy*. Philadelphia, PA: Elsevier Churchill Livingstone.
- Eppinger, R., Sun, E., Kuppa, S., & Saul, R. (2000). *Supplement: Development of Improved Injury Criteria for the Assessment of Advanced Automotive Restraint Systems - II*. Washington, DC: National Highway Traffic Safety Administration (NHTSA).
- Gallagher, K., Howarth, S., & Callaghan, J. (2010). Effects of anterior shear displacement rate on the structural properties of the porcine cervical spine. *J Biomech Eng*, 132(9), 091004.
- Gayzik, F., Moreno, D., Vavalle, N., Rhyne, A., & Stitzel, J. (2011). Development of the Global Human Body Models Consortium mid-sized male full body model. *Injury Biomechanics Research*, 39-12.
- Giles, J., Ferreira, L., Athwal, G., & Johnson, J. (2014). Development and performance evaluation of a multi-PID muscle loading driven in vitro active-motion shoulder simulator and application to assessing reverse total shoulder arthroplasty. *J Biomech Eng*, 136(12), 121007 1-10.

- Goertzen, D., Lane, C., & Oxland, T. (2004). Neutral zone and range of motion in the spine are greater with stepwise loading than with a continuous loading protocol. An in vitro porcine investigation. *J Biomech*, 37(2), 257-261.
- Greenspan, L., McLellan, B., & Greig, H. (1985). Abbreviated Injury Scale and Injury Severity Score: a scoring chart. *J Trauma*, 25(1), 60-64.
- Ivancic, P. (2012). Biomechanics of sports-induced axial-compression injuries of the neck. *J Athl Train*, 47(5), 489-497.
- Ivancic, P., Tominaga, A., Simpson, A., Yue, J., & Panjabi, M. (2008). Biomechanics of cervical facet dislocation. *Traff Inj Prev*, 9(6), 606-611.
- Johannessen, W., Vresilovic, E., Wright, A., & Elliott, D. (2004). Intervertebral disc mechanics are restored following loading and unloaded recovery. *Ann Biomed Eng*, 32(1), 70-76.
- Kleinberger, M., Sun, E., Eppinger, R., Kuppa, S., & Saul, R. (1998). *Development of Improved Injury Criteria for the Assessment of Advanced Automotive Restraint Systems*. Washington, DC: National Highway Traffic Safety Administration (NHTSA).
- Kruger, H., Noonan, V., Trenamen, L., Joshi, P., & Rivers, S. (2013). The economic burden of traumatic spinal cord injury in Canada. *Chronic Dis Inj Can*, 33(3).
- McElhaney, J., & Myers, B. (1993). Biomechanical Aspects of Cervical Trauma. In N. Yoganandan, A. Nahum, & J. Melvin, *Accidental Injury* (pp. 311-361). New York, NY: Springer Science.
- McIntosh, A., & McCrory, P. (2005). Preventing head and neck injury. *Br J Sports Med*, 39, 314-318.
- Melnyk, A., Chak, A., Singh, V., Kelly, A., Cripton, P., Fisher, C., . . . Oxland, T. (2015). Characterization of the behavior of a novel low-stiffness posterior spinal implant under anterior shear loading on a degenerative spine model. *Eur Spine J*, 24, 775-782.
- Melnyk, A., Kelly, A., Chak, J., Wen, T., Cripton, P., Dvorak, M., & Oxland, T. (2015). The effect of disc degeneration on anterior shear translation in the lumbar spine. *J Orth Res*, 33(4), 450-457.
- Mercer, S., & Bogduk, N. (1999). The ligaments and anulus fibrosus of human adult cervical intervertebral discs. *Spine*, 24, 619-626.
- Mertz, H., & Patrick, L. (1971). Strength and response of the human neck. *SAE Technical Paper 710855*.
- Mertz, H., Hodgson, V., & Thomas, L. N. (1978). An assessment of compressive neck loads under injury-producing conditions. *Phys Sportsmed*, 6(11), 95-106.
- Middleditch, A., & Oliver, J. (2005). *Functional Anatomy of the Spine* (2 ed.). London, UK: Elsevier Butterworth Heinemann.
- Miura, T., Panjabi, M., & Cripton, P. (2002). A method to simulate in vivo cervical spine kinematics using in vitro compressive preload. *Spine*, 27(1), 43-48.
- Moroney, S., Schultz, A., Miller, J., & Andersson, G. (1988). Load-displacement properties of lower cervical spine motion segments. *J Biomech*, 21(9), 769-779.

- Myers, B., & Winkelstein, B. (1995). Epidemiology, classification, mechanics and tolerance of human cervical spine injuries. *Crit Rev Biomed Eng*, 23(5-6), 307-409.
- National Spinal Cord Injury Statistical Centre. (2016). *National Spinal Cord Injury Database*. Birmingham, AL: University of Alabama Birmingham.
- NHTSA. (2013). *Timeline of FMVSS by Year and Notable Technologies*. US Department of Transportation, Washington, DC.
- Nightingale, R., Camacho, D., Armstrong, A., Robinette, J., & Myers, B. (2000). Inertial properties and loading rates affect buckling modes and injury mechanisms in the cervical spine. *J Biomech*, 33(2), 191-197.
- Nightingale, R., Richardson, W., & Myers, B. (1997). The effects of padded surfaces on the risk for cervical spine injury. *Spine*, 22(20), 2380-2387.
- Nightingale, R., Winkelstein, B., Knaub, K., Richardson, W., Luck, J., & Myers, B. (2002). Comparative strengths and structural properties of the upper and lower cervical spine in flexion and extension. *J Biomech*, 35(6), 725-732.
- Ombregt, L., Bisschop, P., HJ, t. V., & Van de Velde, T. (2013). *A System of Orthopaedic Medicine* (3 ed.). London, UK: Churchill Livingstone Elsevier.
- Ono, K., Kaneoka, K., Hattori, S., Ujihashi, S., Takhounts, E., Haffner, M., & Eppinger, R. (2003). Cervical vertebral motions and biomechanical responses to direct loading of human head. *Traffic Inj Prev*, 4(2), 141-152.
- Ono, K., Kaneoka, K., Wittek, A., & Kajzer, J. (1997). Cervical injury mechanism based on the analysis of human cervical vertebral motion and head-neck-torso kinematics during low speed rear impacts. *SAE Technical Paper*, 973340.
- Panjabi, M. (1992). The stabilizing system of the spine. Part II. Neutral zone and instability hypothesis. *J Spinal Disord*, 5(4), 390-397.
- Panjabi, M., & White, A. (1980). Basic biomechanics of the spine. *Neurosurgery*, 7(1), 76-93.
- Panjabi, M., Krag, M., Summers, D., & T, V. (1985). Biomechanical time-tolerance of fresh cadaveric human spine specimens. *J Orth Res*, 3(3), 292-300.
- Panjabi, M., Krag, M., White, A., & Southwick, W. (1977). Effects of preload on load displacement curves of the lumbar spine. *Orthop Clin North Am*, 8(1), 181.
- Panjabi, M., Summers, D., Pelker, R. V., Friedlander, G., & Southwick, W. (1986). Three-dimensional load-displacement curves due to forces on the cervical spine. *J Orthop Res*, 4(2), 152-161.
- Parr, J., Miller, M., Pellettiere, J., & Erich, R. (2013). Neck injury criteria formulation and injury risk curves for the ejection environment: a pilot study. *Aviat Space Envir Md*, 84(1240-1248).
- Patwardhan, A., Havey, R., Ghanayem, A., Diener, H., Meade, K., Dunlap, B., & Hodges, S. (2000). Load-carrying capacity of the human cervical spine in compression is increased under a follower load. *Spine*, 25(12), 1548-1554.

- Prasad, P., & Daniel, R. (1984). *A biomechanical analysis of head, neck, and torso injuries to child surrogates due to sudden torso acceleration*. SAE Technical Paper 841656.
- Saari, A., Itshayek, E., & Cripton, P. (2011). Cervical spinal cord deformation during simulated head-first impact injuries. *J Biomech*, *44*(14), 2565-2571.
- Schmitt, K.-U., Niederer, P., Cronin, D., Muser, M., & Walz, F. (2014). *Trauma Biomechanics* (4 ed.). Heidelberg: Springer-Verlag.
- Sekhon, L., & Fehlings, M. (2001). Epidemiology, demographics, and pathophysiology of acute spinal cord injury. *Spine*, *26*(24S), S2-S12.
- Shateri, H., & Cronin, D. (2015). Out-of-position rear impact tissue-level investigation using detailed finite element neck model. *Traff Inj Prev*, *16*(7), 698-708.
- Shea, M., Edwards, W., White, A., & Hayes, W. (1991). Variations of stiffness and strength along the human cervical spine. *J Biomech*, *24*(2), 95-107.
- Skrzypiec, D., Klein, A., Bishop, N., Stahmer, F., Puschel, K., Seidel, H., . . . Huber, G. (2012). Shear strength of the human lumbar spine. *Clin Biomech*, *27*(7), 646-651.
- Wilson, J., Vccaro, A., Harrop, J., Aarabi, B., Shaffrey, C., Dvorak, M., . . . Fehlings, M. (2013). The impact of facet dislocation on clinical outcomes after cervical spinal cord injury: results of a multicenter North American prospective cohort study. *Spine*, *38*(2), 97-103.
- Yingling, V., & McGill, S. (1999). Anterior shear of spinal motion segments: kinematics, kinetics, and resultant injuries observed in a porcine model. *Spine*, *24*(18), 1882-1889.

## Appendices

### Appendix A: $N_{ij}$ Formula

$$N_{ij} = \frac{F_{\text{compression-tension}}}{F_{\text{critical}}} + \frac{M_{\text{flexion-extension}}}{M_{\text{critical}}}$$

(Kleinberger *et al*, 1998)

$F_{\text{compression-tension}}$  and  $M_{\text{flexion-extension}}$  are input in N and Nm for each time instant during a frontal crash test for a particular ATD.  $F_{\text{critical}}$  and  $M_{\text{critical}}$  are constant values that refer to the critical force and moment values for the particular size, age and sex of the ATD being considered. If the  $N_{ij}$  meets or exceeds 1.0 at any time instant during the test for any ATD, then a failing result is recorded.

**Critical Force and Moment Values for  $N_{ij}$  Calculation for Various ATDs**

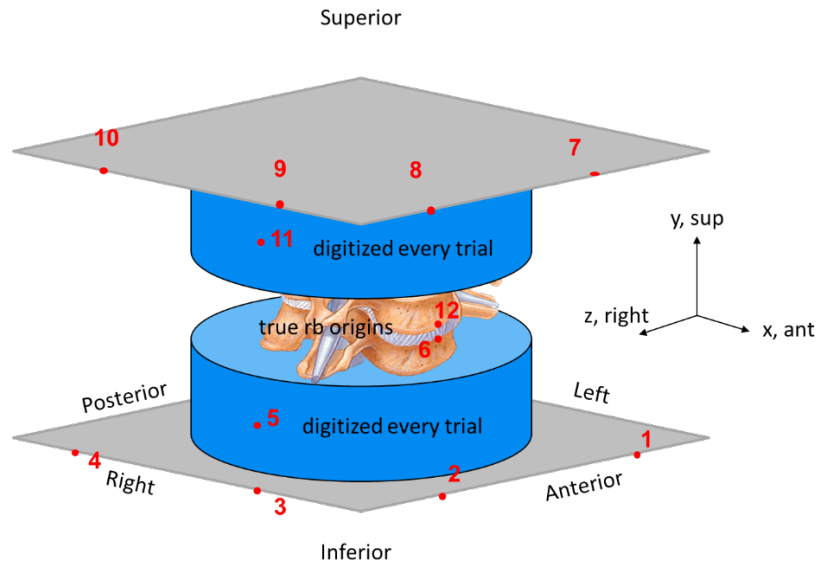
ATD	Tension (N)	Compression (N)	Flexion (Nm)	Extension (Nm)
CRABI 12 month old	2200	2200	85	25
H-III 3 year old	2500	2500	100	30
H-III 6 year old	2900	2900	125	40
H-III 5 <sup>th</sup> percentile female	3200	3200	210	60
H-III 50 <sup>th</sup> percentile male	3600	3600	410	125

(Kleinberger *et al*, 1998)

## Appendix B: Kinematics algorithm

All calculations performed in Matlab R2016b. Built-in functions used as described herein. In Chapter 2, the coordinate system was as described here. In Chapter 4, The coordinate system was rotated such that anterior was +z, superior was +y and right lateral was +x. The general algorithm used was however, the same.

**Determine position of rigid body origins (points 6 & 12) relative to points 5 & 11 (points that were digitized prior to each trial) in anatomical CS. Obtain transformation matrix to transform point 5 → 6 , point 11 → 12 for each trial.**



Adapted from Doodkorte, 2016

$$\hat{z}_{inferior} = \frac{digi_2 - digi_1}{norm(digi_2 - digi_1)} ; \hat{z}_{superior} = \frac{digi_8 - digi_7}{norm(digi_8 - digi_7)}$$

$$\hat{x}_{inferior} = \frac{digi_3 - digi_4}{norm(digi_3 - digi_4)} ; \hat{x}_{superior} = \frac{digi_9 - digi_{10}}{norm(digi_9 - digi_{10})}$$

$$\hat{y}_{inferior} = \frac{\hat{z}_{inferior} \times \hat{x}_{inferior}}{norm(\hat{z}_{inferior} \times \hat{x}_{inferior})} ; \hat{y}_{superior} = \frac{\hat{z}_{superior} \times \hat{x}_{superior}}{norm(\hat{z}_{superior} \times \hat{x}_{superior})}$$

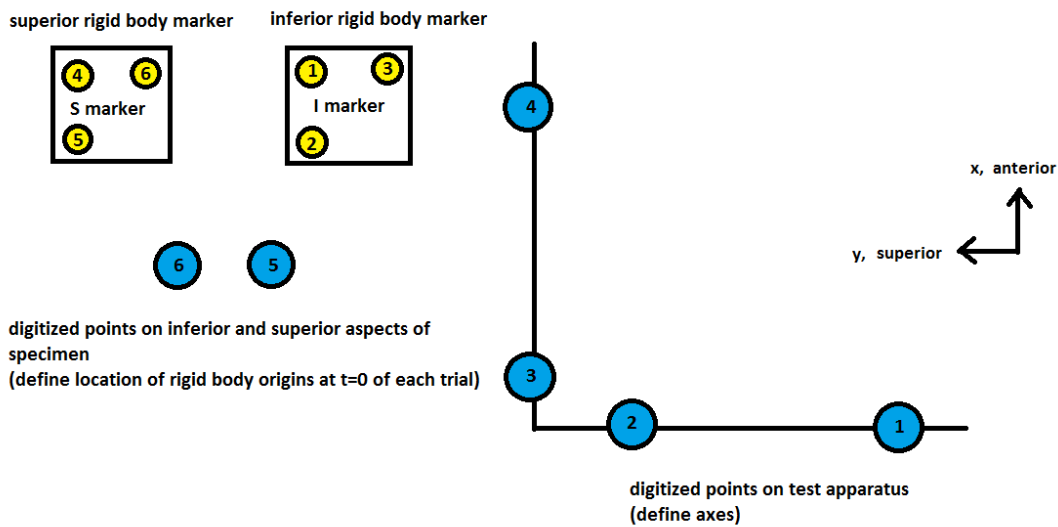
$$T_{inferior, initial} = \begin{bmatrix} 1 & 0 & 0 & 0 \\ digi_{5x} Opto & \hat{x}_i & \hat{y}_i & \hat{z}_i \\ digi_{5y} Opto & \hat{x}_j & \hat{y}_j & \hat{z}_j \\ digi_{5z} Opto & \hat{x}_k & \hat{y}_k & \hat{z}_k \end{bmatrix} ; T_{superior, initial} = \begin{bmatrix} 1 & 0 & 0 & 0 \\ digi_{11x} Opto & \hat{x}_i & \hat{y}_i & \hat{z}_i \\ digi_{11y} Opto & \hat{x}_j & \hat{y}_j & \hat{z}_j \\ digi_{11z} Opto & \hat{x}_k & \hat{y}_k & \hat{z}_k \end{bmatrix}$$

$$T_{inferior,trial} = \begin{bmatrix} 1 & 0 & 0 & 0 \\ digi_{5x\ Opto} & \hat{x}_i & \hat{y}_i & \hat{z}_i \\ digi_{5y\ Opto} & \hat{x}_j & \hat{y}_j & \hat{z}_j \\ digi_{5z\ Opto} & \hat{x}_k & \hat{y}_k & \hat{z}_k \end{bmatrix}; T_{superior,trial} = \begin{bmatrix} 1 & 0 & 0 & 0 \\ digi_{11x\ Opto} & \hat{x}_i & \hat{y}_i & \hat{z}_i \\ digi_{11y\ Opto} & \hat{x}_j & \hat{y}_j & \hat{z}_j \\ digi_{11z\ Opto} & \hat{x}_k & \hat{y}_k & \hat{z}_k \end{bmatrix}$$

$$Inf\ Origin_{trial} = [T_{inf,trial}] * [T_{inf,initial}]^{-1} * \begin{bmatrix} 1 \\ digi_{6x\ Opto} \\ digi_{6y\ Opto} \\ digi_{6z\ Opto} \end{bmatrix}; Sup\ Origin_{trial} = [T_{sup,trial}] * [T_{sup,initial}]^{-1} * \begin{bmatrix} 1 \\ digi_{12x\ Opto} \\ digi_{12y\ Opto} \\ digi_{12z\ Opto} \end{bmatrix}$$

Result: the 1x3 vector in column 1 represents the xyz coordinates of the rigid body origins in the anatomical CS.

### Transformation of Optotrak rigid body marker data to anatomical coordinate system



$$\hat{y}_{anatomical} = \frac{digi_2 - digi_1}{norm(digi_2 - digi_1)}$$

$$\hat{x}_{anatomical} = \frac{digi_4 - digi_3}{norm(digi_4 - digi_3)}$$

$$\hat{z}_{anatomical} = \frac{\hat{x}_{anatomical} \times \hat{y}_{anatomical}}{norm(\hat{x}_{anatomical} \times \hat{y}_{anatomical})}$$

### Initial, reference position transformation from marker CS to anatomical CS:

$$\begin{aligned}\hat{x}_{inferior,t=0} &= \frac{marker_1 - marker_2}{norm(marker_1 - marker_2)} ; x_{superior,t=0} = \frac{marker_4 - marker_5}{norm(marker_4 - marker_5)} \\ \hat{y}_{inferior,t=0} &= \frac{marker_1 - marker_3}{norm(marker_1 - marker_3)} ; y_{superior,t=0} = \frac{marker_4 - marker_6}{norm(marker_4 - marker_6)} \\ \hat{z}_{inf,t=0} &= \frac{\hat{x}_{inferior,t=0} \times \hat{y}_{inferior,t=0}}{norm(\hat{x}_{inferior,t=0} \times \hat{y}_{inferior,t=0})} ; \hat{z}_{sup,t=0} = \frac{\hat{x}_{superior,t=0} \times \hat{y}_{superior,t=0}}{norm(\hat{x}_{superior,t=0} \times \hat{y}_{superior,t=0})} \\ T_{a_{inf,t=0}} &= \begin{bmatrix} 1 & 0 & 0 & 0 \\ digi_{5x\ Opto} & \hat{x}_{anat,i} & \hat{y}_{anat,i} & \hat{z}_{anat,i} \\ digi_{5y\ Opto} & \hat{x}_{anat,j} & \hat{y}_{anat,j} & \hat{z}_{anat,j} \\ digi_{5z\ Opto} & \hat{x}_{anat,k} & \hat{y}_{anat,k} & \hat{z}_{anat,k} \end{bmatrix} ; T_{a_{sup,t=0}} = \begin{bmatrix} 1 & 0 & 0 & 0 \\ digi_{6x\ Opto} & \hat{x}_{anat,i} & \hat{y}_{anat,i} & \hat{z}_{anat,i} \\ digi_{6y\ Opto} & \hat{x}_{anat,j} & \hat{y}_{anat,j} & \hat{z}_{anat,j} \\ digi_{6z\ Opto} & \hat{x}_{anat,k} & \hat{y}_{anat,k} & \hat{z}_{anat,k} \end{bmatrix} \\ T_{m_{inf,t=0}} &= \begin{bmatrix} 1 & 0 & 0 & 0 \\ marker_{1x} & \hat{x}_{inf,i} & \hat{y}_{inf,i} & \hat{z}_{inf,i} \\ marker_{1y} & \hat{x}_{inf,j} & \hat{y}_{inf,j} & \hat{z}_{inf,j} \\ marker_{1z} & \hat{x}_{inf,k} & \hat{y}_{inf,k} & \hat{z}_{inf,k} \end{bmatrix} ; T_{m_{sup,t=0}} = \begin{bmatrix} 1 & 0 & 0 & 0 \\ marker_{4x} & \hat{x}_{sup,i} & \hat{y}_{sup,i} & \hat{z}_{sup,i} \\ marker_{4y} & \hat{x}_{sup,j} & \hat{y}_{sup,j} & \hat{z}_{sup,j} \\ marker_{4z} & \hat{x}_{sup,k} & \hat{y}_{sup,k} & \hat{z}_{sup,k} \end{bmatrix} \\ Tm \rightarrow a_{inf,t=0} &= [T_{m_{inf,t=0}}]^{-1} * [T_{a_{inf,t=0}}] ; Tm \rightarrow a_{sup,t=0} = [T_{m_{sup,t=0}}]^{-1} * [T_{a_{sup,t=0}}]\end{aligned}$$

Result: Tm->a matrices represent transformation of marker data (Optotrak CS) to the anatomical CS at time=0.

### Transformation from marker to anatomical CS at time=i

$$\begin{aligned}\hat{x}_{inferior,t=i} &= \frac{marker_1 - marker_2}{norm(marker_1 - marker_2)} ; \hat{x}_{superior,t=i} = \frac{marker_4 - marker_5}{norm(marker_4 - marker_5)} \\ \hat{y}_{inferior,t=i} &= \frac{marker_1 - marker_3}{norm(marker_1 - marker_3)} ; \hat{y}_{superior,t=i} = \frac{marker_4 - marker_6}{norm(marker_4 - marker_6)} \\ \hat{z}_{inf,t=i} &= \frac{\hat{x}_{inferior,t=0} \times \hat{y}_{inferior,t=0}}{norm(\hat{x}_{inferior,t=0} \times \hat{y}_{inferior,t=0})} ; \hat{z}_{sup,t=i} = \frac{\hat{x}_{superior,t=0} \times \hat{y}_{superior,t=0}}{norm(\hat{x}_{superior,t=0} \times \hat{y}_{superior,t=0})} \\ T_{m_{inf,t=i}} &= \begin{bmatrix} 1 & 0 & 0 & 0 \\ marker_{1x} & \hat{x}_{inf,i} & \hat{y}_{inf,i} & \hat{z}_{inf,i} \\ marker_{1y} & \hat{x}_{inf,j} & \hat{y}_{inf,j} & \hat{z}_{inf,j} \\ marker_{1z} & \hat{x}_{inf,k} & \hat{y}_{inf,k} & \hat{z}_{inf,k} \end{bmatrix} ; T_{m_{sup,t=i}} = \begin{bmatrix} 1 & 0 & 0 & 0 \\ marker_{4x} & \hat{x}_{inf,i} & \hat{y}_{inf,i} & \hat{z}_{inf,i} \\ marker_{4y} & \hat{x}_{inf,j} & \hat{y}_{inf,j} & \hat{z}_{inf,j} \\ marker_{4z} & \hat{x}_{inf,k} & \hat{y}_{inf,k} & \hat{z}_{inf,k} \end{bmatrix} \\ Tm \rightarrow a_{inf,t=i} &= [T_{m_{inf,t=i}}] * [Tm \rightarrow a_{inf,t=0}] ; Tm \rightarrow a_{sup,t=i} = [T_{m_{sup,t=i}}] * [Tm \rightarrow a_{sup,t=0}]\end{aligned}$$

Result: these Tm->a matrices represent the transformation from the initial position of the markers (anatomical CS) to their position for all time=i (anatomical CS). The 1x3 vector located in column 1 represents the position (anatomical CS) of the inferior and superior markers for each time i.

$$Pa_{inf,t=i} = Tm \rightarrow a_{inf,t=i}, r2: 4, c1 ; Pa_{sup,t=i}, r2: 4, c1$$

$$Displacement_{sup \rightarrow inf,t=i} = \begin{bmatrix} \hat{x}_{global,i} & \hat{y}_{global,i} & \hat{z}_{global,i} \\ \hat{x}_{global,j} & \hat{y}_{global,j} & \hat{z}_{global,j} \\ \hat{x}_{global,k} & \hat{y}_{global,k} & \hat{z}_{global,k} \end{bmatrix}^{-1} * [Pa_{sup,t=i} - Pa_{inf,t=i}]^T$$

$$Euler\ angles_{sup \rightarrow inf, t=i} = rotm2eul \left( [Ta_{sup, t=i}, r2: 4, c2: 4]^{-1} * [Ta_{inf, t=i}, r2: 4, c2: 4] \right)$$

Thus, displacement is represented as the difference between the time=i position of the superior (non-fixed) marker, and its initial position at time=0, relative to the initial position of the inferior (fixed) marker at time=0. This defines the initial position of the specimen at the beginning of the loading cycle being analyzed to be 0mm displacement.

The rotation angles are represented as the Euler angle of the instantaneous anatomical coordinate system relative to the fixed anatomical coordinate system (defined by the test apparatus digitization). Thus, the Euler angles at time=0 may be non-zero.

## Appendix C: Full Results for Chapter 2

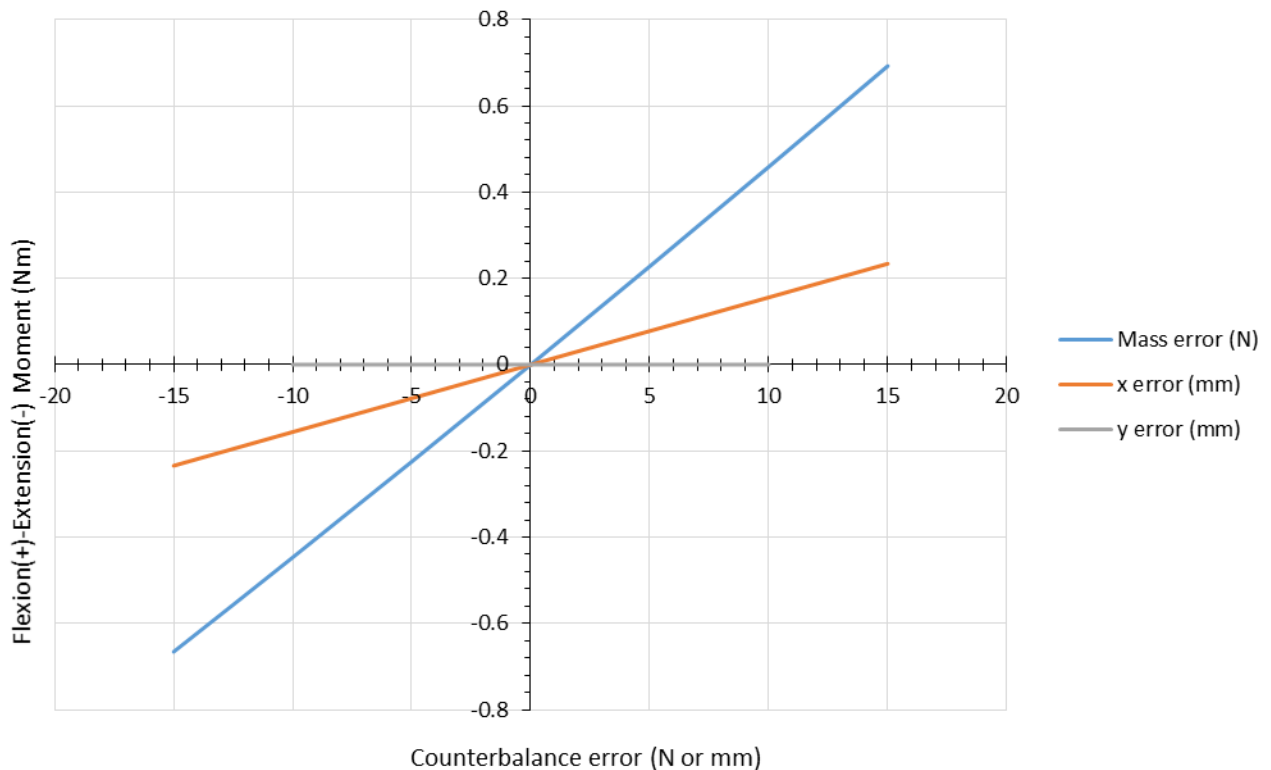
### Stiffness Results for Each Individual Specimen in Each Shearing Direction

<b>Anterior</b>						
	<b>Intact</b>		<b>Lig cut</b>		<b>Disc</b>	
<b>Specimen</b>	<b>0-20</b>	<b>20-100</b>	<b>0-20</b>	<b>20-100</b>	<b>0-20</b>	<b>20-100</b>
<b>1_1424</b>	93.9	101.4	64.2	148.5	32.2	77.7
<b>2_1418</b>	205.8	326.2	79.5	122.7	119.4	131.8
<b>5_1419</b>	32.7	97.2	42.9	154.7	22.8	87.0
<b>6_1410</b>	137.1	240.1	40.5	239.7	21.2	141.5
<b>7_1415</b>	32.3	162.8		158.1		87.1
<b>8_1423</b>	169.6	516.7	233.4	599.9	63.1	607.5
<b>Posterior</b>						
	<b>Intact</b>		<b>Lig cut</b>		<b>Disc</b>	
<b>Specimen</b>	<b>0-20</b>	<b>20-100</b>	<b>0-20</b>	<b>20-100</b>	<b>0-20</b>	<b>20-100</b>
<b>1_1424</b>	71.1	105.3	44.9	155.9	47.8	91.7
<b>2_1418</b>	137.0	179.3	40.3	195.3	101.3	148.1
<b>5_1419</b>	21.8	112.2	24.2	104.5	11.7	89.7
<b>6_1410</b>	47.6	182.2	75.4	196.5	55.4	180.9
<b>7_1415</b>	29.7	92				82.5
<b>8_1423</b>	107	569.5	174.8	509.1	48.8	509.4
<b>Lateral</b>						
	<b>Intact</b>	<b>Lig cut</b>	<b>Disc</b>			
<b>Specimen</b>	<b>20-100</b>	<b>20-100</b>	<b>20-100</b>			
<b>1_1424</b>	172.8	117.5	139.7			
<b>2 - 1418</b>	407.4	306.0	295.8			
<b>5_1419</b>	202.1	198.4	206.4			
<b>6_1410</b>	258.5	272.4	283.6			
<b>7_1415</b>	123.7	114.0	115.6			
<b>8_1423</b>	723.0	-	267.1			

## Appendix D: Counterbalance System Error Analysis

A brief investigation into the potential effect of counterbalance system errors was completed. Deviations in the location of the counterbalance force point of application were prescribed in the x and y directions, independently. Deviation in the magnitude of the counterbalance force (ie. mass) was also assessed independently. The effects of combined errors (ie. position error and mass error) were found to be approximately additive (not shown). Simulations were run as 5 second static trials, as anterior shearing was found to have a corrective effect on the predicted artefact moments.

Because of the high magnitude of error required to cause noteworthy artefact loading, design solutions to this source of error were not pursued further. Though artefact moments may result from errors in the counterbalance, careful methodological determination of the centre of mass and mass of the superior loading plate and superior half of the specimen should be possible. For context, in the simulations the ideal counterbalance mass was 15 N.



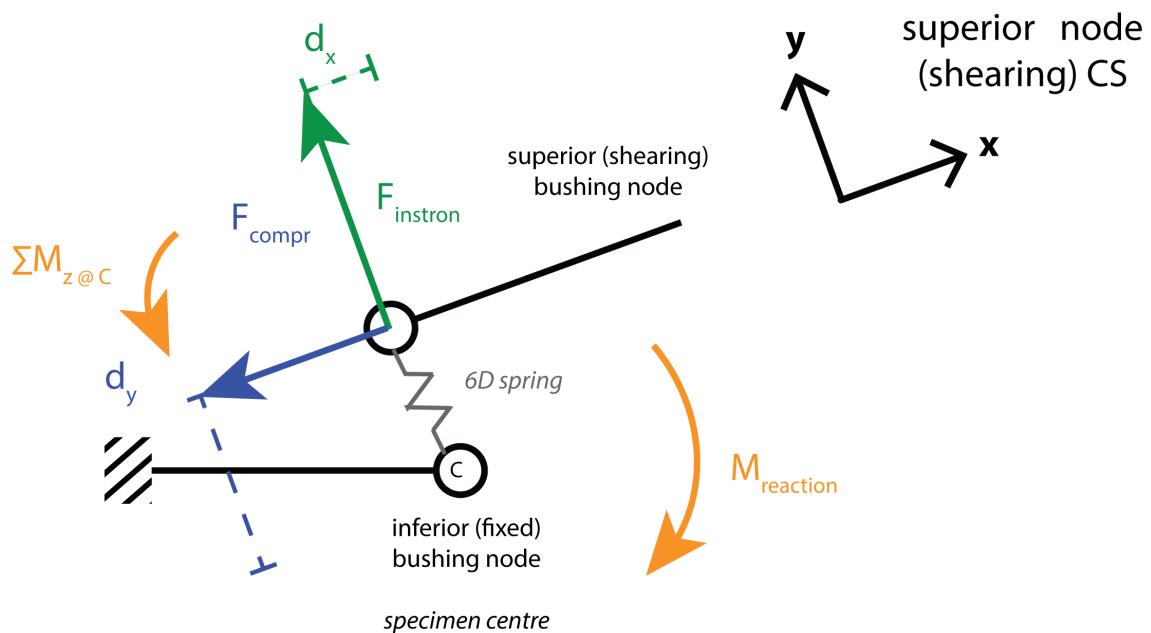
**Simulated effect of errors in counterbalance position (x, y) or mass magnitude on artefact flexion-extension moments**

## Appendix E: ADAMS moment computation algorithm

These formulae and free body diagrams illustrate how the reported specimen flexion-extension moments were computed by ADAMS MSC in the cadaver-based specimen simulations, where a bushing-like joint was used to model the specimen. ADAMS reports both the net moment between the two rigid bodies joined by the bushing-like joint, and the reaction moment at the fixed node for a given time instant. These moment calculations are based on the current magnitude and position of applied forces relative to the fixed node in the superior node coordinate system. The stiffness values assigned to the bushing-like joint (6D) are used to determine instantaneous deformations caused by the moments and forces applied across the joint.

Moments for the cadaver-based simulations were reported as the reaction moment at the inferior node.

### ADAMS moment calculation algorithm: unconstrained, point load model

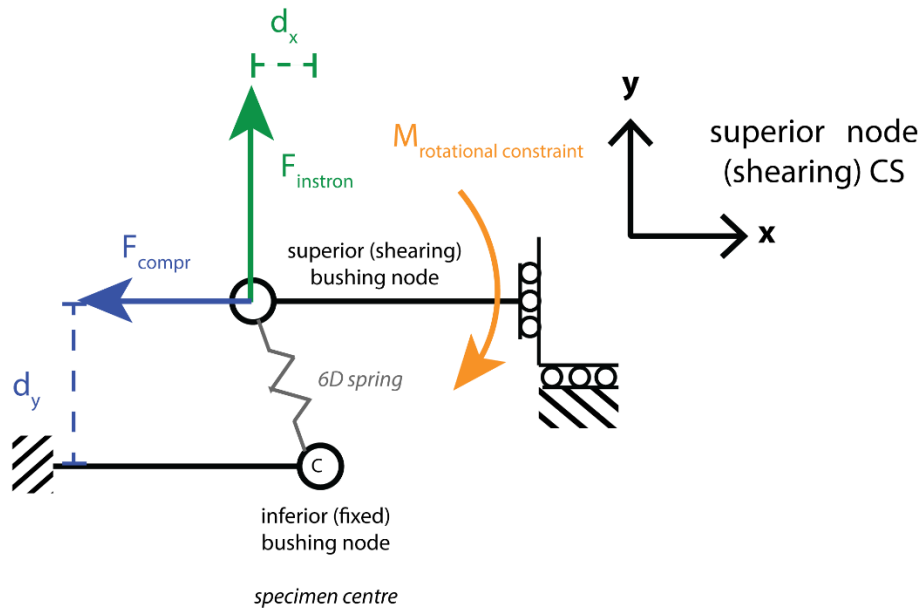


$$\Sigma M_{z@c} = F_{compr} d_y - F_{instron} d_x - M_r \neq 0$$

$$M_r = F_{compr} d_y - F_{instron} d_x - \Sigma M_{z@c}$$

computed separately by ADAMS at each time instant; specimen moment reported as sum of net moment ( $\Sigma M$ ) and  $M_r$

## ADAMS moment calculation algorithm: rotationally constrained model

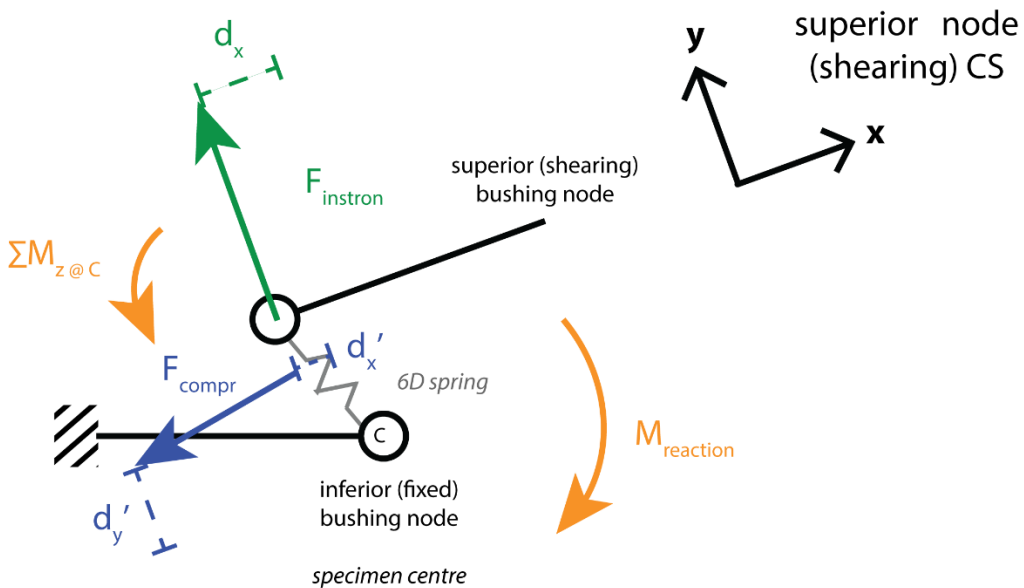


$$\Sigma M_{z@C} = F_{compr} d_y - F_{instron} d_x - M_{rc@C} = 0$$

$$M_{rc@C} = F_{compr} d_y - F_{instron} d_x$$

computed separately by ADAMS at each time instant; specimen moment reported as sum of net moment ( $\Sigma M$ ) and  $M_r$

## ADAMS moment calculation algorithm: follower load model



$$\Sigma M_{z@C} = F_{compr x} d'_y + F_{compr y} d'_x - F_{instron} d_x - M_r \neq 0$$

$$M_r = F_{compr x} d'_y + F_{compr y} d'_x - F_{instron} d_x - \Sigma M_{z@C}$$

computed separately by ADAMS at each time instant; specimen moment reported as sum of net moment ( $\Sigma M$ ) and  $M_r$

## Appendix F: AMTI MCA-6-500 Calibration Matrix

### ADVANCED USE (Sensitivity Matrix Analysis) M5379M

SI Units:                      SENSITIVITY MATRIX S(i, j)  
 Output of channel i (uV/Vex) is S(i,j) times the  
 mechanical input j (N, N-m)

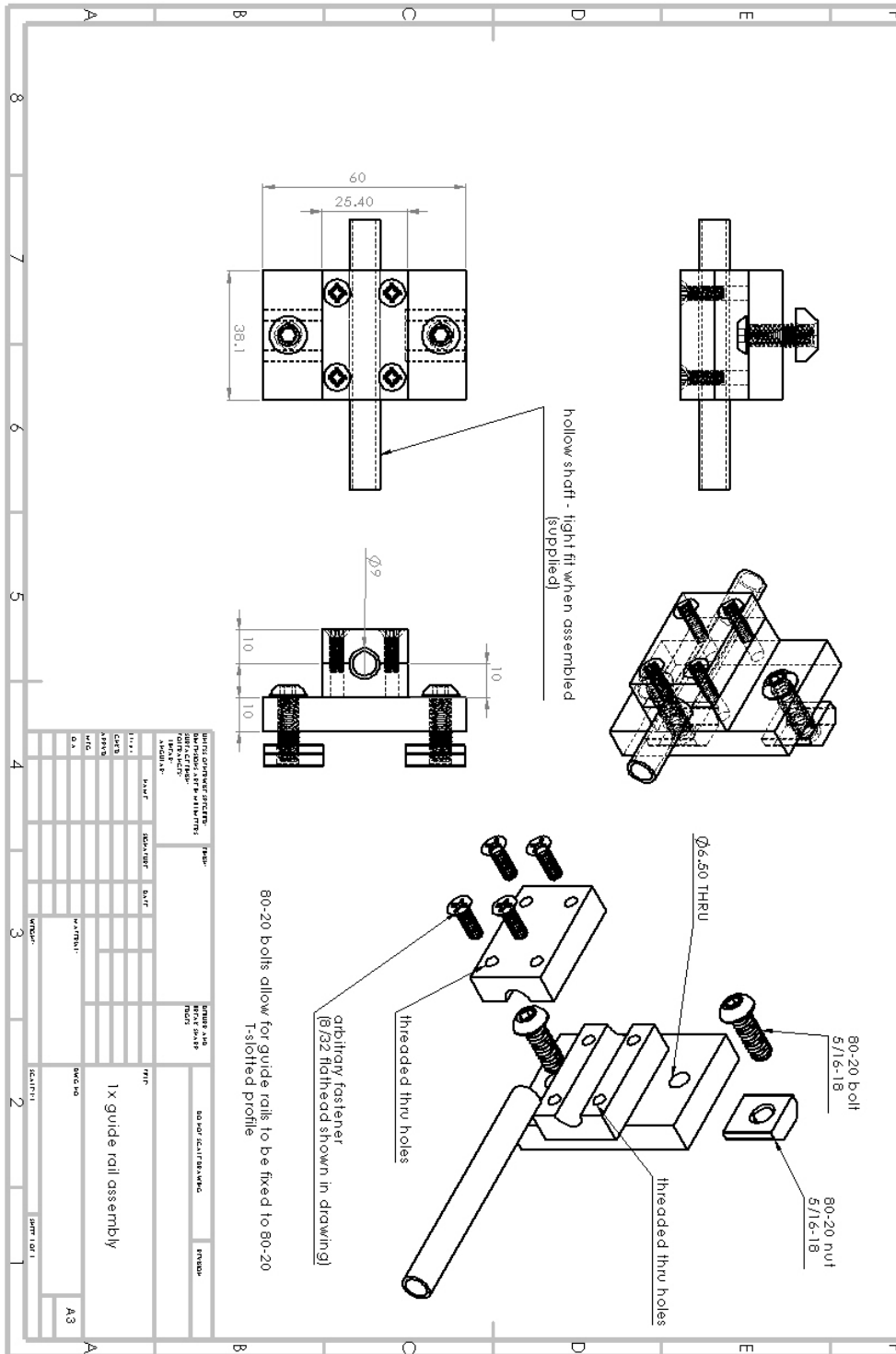
j i	Fx	Fy	Fz	Mx	My	Mz
Vfx	1.3471	-.0037	-.0058	-.1724	-.0363	.4841
Vfy	.0142	1.3504	.0019	.0515	.1534	-.2378
Vfz	-.0019	-.0088	.3437	-.0462	.3438	.2568
Vmx	.0031	.0091	-.0485	72.5343	-.1781	.2945
Vmy	.0091	-.0023	.0309	.9849	72.5087	-.5348
Vmz	.0388	.0125	-.0005	.4397	.1702	51.2015

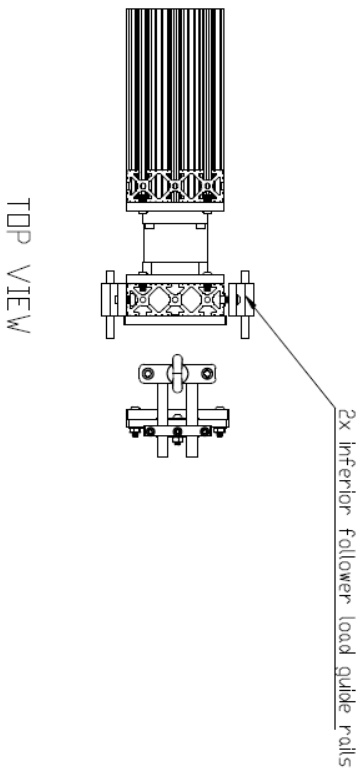
### Appendix G: Full Experimental Results for Each Axial Compression Method & Specimen, Cycle 3

File Name Trial Name	Instron disp (mm)	specimen shear (mm)	specimen FE (deg)	Instron shear (N)	AP shear (N)	RL shear (N)	CT (N)	LB (Nm)	AR (Nm)	FE (Nm)
P1_C7-T1_002 PL 0	1.4984 2.9954	0.8994 1.5749	0.1446 0.05129	11.9607 34.3286	5.2809 20.6823	0.1252 0.6089	0.0655 0.3913	0.0128 0.0500	-0.0030 -0.0057	-0.0690 -0.2683
P1_C7-T1_003 FI 5050	1.4959 2.9955	0.4958 1.4052	-0.0415 -0.0376	19.4141 46.4463	10.7519 29.2877	0.0746 0.7946	271.5537 271.8412	0.0267 0.0715	-0.0049 -0.0095	-0.1435 -0.3828
P1_C7-T1_004 FI 5015	1.4957 2.9952	0.3646 1.2806	0.1788 0.5717	16.4529 41.1258	8.1870 25.6315	0.3127 0.9371	271.5840 271.8437	0.0195 0.0614	-0.0020 -0.0073	-0.1064 -0.3332
P1_C7-T1_005 FL 5085	1.4953 2.9951	0.3290 0.9522	0.1614 0.4049	10.0994 28.0691	4.6816 17.2256	0.6223 1.4304	271.4923 271.3494	0.0111 0.0414	-0.0002 -0.0036	-0.0572 -0.2173
P1_C7-T1_006 PL 300	1.4967 2.9953	0.3052 1.1705	0.017 0.4107	13.5132 33.3611	5.7240 18.9209	0.3007 0.6869	271.5157 271.5412	0.0139 0.0456	-0.0022 -0.0069	-0.0743 -0.2470
P1_C7-T1_007 RC 0	1.4982 2.9951	1.5357 2.9797	-0.0685 -0.0654	12.3673 50.8686	6.9667 35.6204	0.1472 0.8383	-0.2523 -0.9269	0.0168 0.0862	-0.0039 -0.0148	-0.0893 -0.4622
P1_C7-T1_009 RC 300	1.4975 2.9953	1.2904 2.7020	-0.5459 -0.5207	33.1845 67.2006	24.9094 49.1872	1.2057 1.9973	271.2861 271.3983	0.0590 0.1169	-0.0053 -0.0150	-0.3126 -0.6205
P2_C6-C7_001 PL 0	1.4986 2.9952	0.5124 1.1736	0.0939 0.05344	13.4415 37.1064	4.7956 21.3942	-0.0184 0.6934	0.5993 0.2730	0.0114 0.0520	-0.0028 -0.0003	-0.0631 -0.2807
P2_C6-C7_002 FL 50/50	1.4965 2.9952	1.4805 2.5879	1.753 2.611	14.7967 39.6488	9.0976 26.1659	0.4866 1.0124	134.5696 134.8064	0.0220 0.0638	-0.0019 -0.0062	-0.1175 -0.3405
P2_C6-C7_003 FL 50/15	1.4981 2.9952	2.2849 3.6878	2.171 2.603	20.4762 46.1919	10.5048 28.8975	0.4928 1.4886	134.5541 134.2489	0.0256 0.0691	-0.0014 -0.0023	-0.1368 -0.3718
P2_C6-C7_004 FI 5085	1.4975 2.9951	0.5716 1.5178	0.1527 0.164	18.1371 43.6062	10.2882 27.5266	0.3880 1.1115	134.6614 134.1719	0.0247 0.0655	-0.0013 -0.0036	-0.1329 -0.3529
P2_C6-C7_005 PI 300	1.4953 2.9956	0.7283 1.8625	0.2009 0.3056	22.3840 50.8542	12.0575 31.4347	0.4853 1.1145	134.5265 134.2863	0.0291 0.0752	-0.0022 -0.0079	-0.1556 -0.4055
P2_C6-C7_006 RC 0	1.4980 2.9953	1.5333 2.8918	0.1016 0.1584	14.8849 69.2696	12.4535 50.8711	0.1006 0.8052	0.5124 -0.2926	0.0297 0.1225	-0.0038 -0.0093	-0.1639 -0.6685

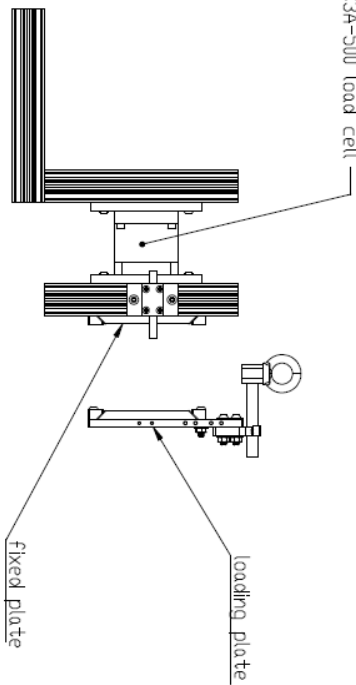
P2_C6-C7_007	1.4979	1.4597	0.216	37.1486	33.4403	0.3870	270.0755	0.0786	-0.0115	-0.4334
RC 300	2.9953	2.9009	0.2811	84.1088	66.4839	1.4353	269.7442	0.1571	-0.0166	-0.8573
P2_C4-C5_003	1.4952	1.4296	0.2149	24.1943	18.5215	0.2816	0.5597	0.0449	-0.0094	-0.2458
RC 0	2.9951	2.8390	0.2823	79.8452	56.6668	0.7245	-0.2936	0.1372	-0.0347	-0.7513
P2_C4-C5_002	1.4978	1.3185	0.2042	45.4947	30.5936	1.2223	121.2753	0.0725	-0.0066	-0.3927
RC 300	2.9954	2.6840	0.2775	103.8541	72.0396	1.6298	121.7357	0.1714	-0.0369	-0.9365
P2_C4-C5_005	1.4958	1.6110	0.8557	7.6167	2.8625	0.1460	0.8371	0.0070	-0.0013	-0.0371
PI 0	2.9958	2.4879	1.04	22.0408	12.2985	0.4806	0.6384	0.0303	-0.0036	-0.1623
P2_C4_C5_006	1.4972	3.6503	-6.321	19.7865	16.8247	1.0154	132.5620	0.0401	-0.0012	-0.2167
FL 5085	2.9952	3.6740	-5.052	44.0543	31.9807	1.8364	132.4537	0.0768	-0.0007	-0.4116
P2_C4-C5_007	1.4965	0.1608	0.262	8.4495	3.1122	0.0548	134.3629	0.0080	0.0024	-0.0427
FL 5015	2.9952	1.1456	1.208	17.7081	9.3113	1.4422	133.8071	0.0218	0.0049	-0.1164
P2_C4_C5_008	1.4987	5.6278	-11.1	11.3707	17.4065	1.4643	134.2976	0.0413	0.0013	-0.2107
FL 5050	2.9952	5.5783	-10.2	22.7596	24.4432	1.3153	133.7688	0.0586	0.0060	-0.2993
P2_C4-C5_010	1.4966	0.6042	0.2451	20.7727	8.6869	0.1505	283.4409	0.0211	0.0018	-0.1152
PL 300	2.9952	1.5285	0.4772	50.7695	28.6091	0.5776	283.6742	0.0691	-0.0031	-0.3770
P1_C5-C6_010	1.4977	0.7714	0.4222	17.9002	9.7521	0.2246	0.3595	0.0233	0.0025	-0.1261
PL 0	2.9955	1.7460	0.6391	47.8969	31.9004	1.1839	-0.0863	0.0775	0.0037	-0.4117
P1_C5-C6_011	1.4978	0.8493	0.5476	32.9724	17.7986	0.7569	270.2435	0.0411	0.0059	-0.2209
FL 5085	2.9950	1.9747	0.9829	64.3055	40.6319	1.90	269.1373	0.0940	0.0118	-0.5027
P1_C5-C6_012	1.4961	0.9106	0.4822	27.9814	16.9268	0.7854	270.8943	0.0403	0.0004	-0.2153
FL 5015	2.9951	2.0430	0.7590	59.7494	40.5976	1.6554	270.9247	0.0970	0.0036	-0.5161
P1_C5-C6_013	1.4977	0.7671	0.3187	26.0929	16.7986	0.7516	270.9566	0.0399	0.0037	-0.2129
FL 5050	2.9950	1.7996	0.4227	57.8719	40.6671	1.2853	271.2081	0.0977	0.0079	-0.5194
P1_C5-C6_014	1.4968	0.7931	0.2635	31.0075	18.6720	0.4107	270.4179	0.0448	0.0023	-0.2376
PL 300	2.9956	1.8392	0.6090	62.4348	42.2495	1.0249	269.9906	0.1008	0.0049	-0.5338
P1_C5-C6_003	1.4989	1.4628	0.0070	9.5366	12.5673	0.2722	1.1084	0.0302	0.0016	-0.1636
RC 0	2.9951	2.8073	0.0121	63.1626	51.4019	1.7555	0.3031	0.1248	0.0026	-0.6643
P1_C5-C6_001	1.4970	1.2650	-0.1228	43.2339	32.0637	1.2505	269.8279	0.0760	0.0095	-0.3980
RC 300	2.9953	2.6045	-0.1545	85.6309	63.1362	2.2791	268.9868	0.1492	0.0174	-0.7830

# Appendix H: Follower Load Guide Drawings

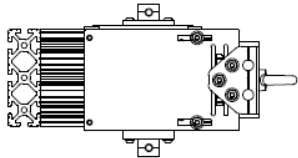
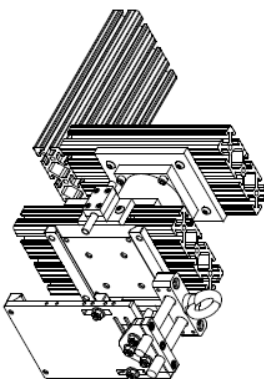




TOP VIEW



FRONT VIEW



DPVS Educational Product

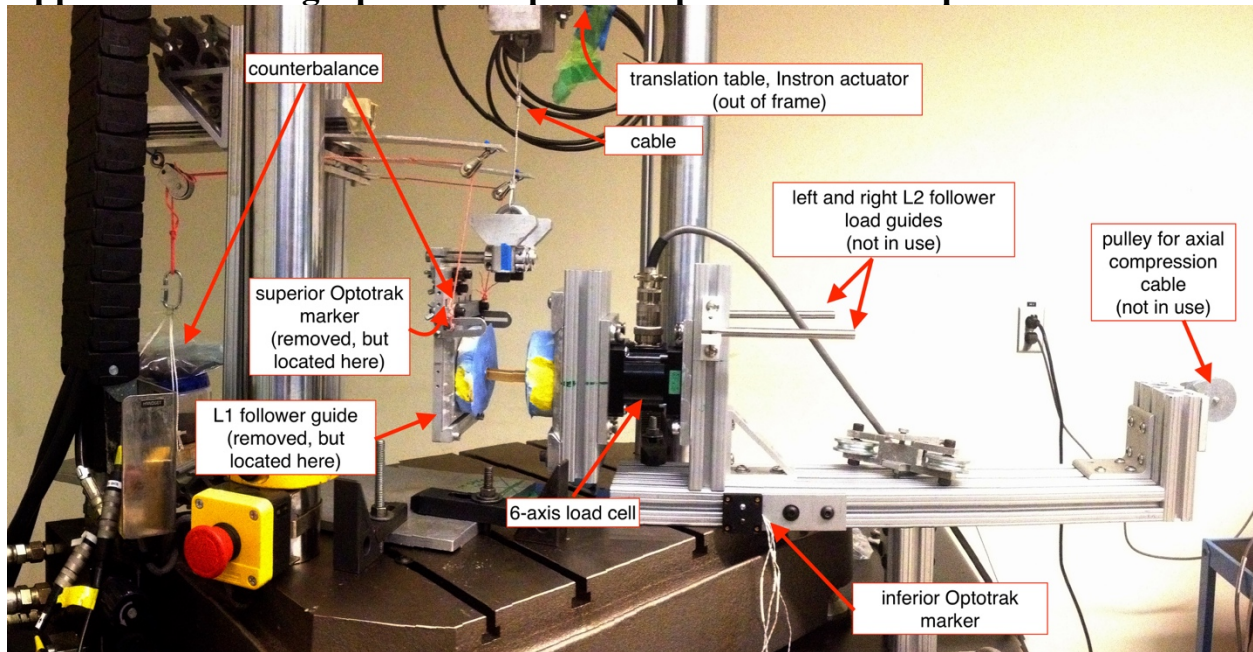
TEST MESSAGE SPECIFICATIONS		SECTION	
SPECIFIC FUNCTION		SECTION	
DESCRIPTIONS ARE IN MILLIMETERS		SECTION	
UNLESS OTHERWISE SPECIFIED		SECTION	
MATERIALS		SECTION	
NO.	NAME	QUANTITY	DATE
001			
002			
003			
004			
005			
006			
007			
008			
009			
010			
011			
012			
013			
014			
015			
016			
017			
018			
019			
020			
021			
022			
023			
024			
025			
026			
027			
028			
029			
030			
031			
032			
033			
034			
035			
036			
037			
038			
039			
040			
041			
042			
043			
044			
045			
046			
047			
048			
049			
050			
051			
052			
053			
054			
055			
056			
057			
058			
059			
060			
061			
062			
063			
064			
065			
066			
067			
068			
069			
070			
071			
072			
073			
074			
075			
076			
077			
078			
079			
080			
081			
082			
083			
084			
085			
086			
087			
088			
089			
090			
091			
092			
093			
094			
095			
096			
097			
098			
099			
100			
101			
102			
103			
104			
105			
106			
107			
108			
109			
110			
111			
112			
113			
114			
115			
116			
117			
118			
119			
120			
121			
122			
123			
124			
125			
126			
127			
128			
129			
130			
131			
132			
133			
134			
135			
136			
137			
138			
139			
140			
141			
142			
143			
144			
145			
146			
147			
148			
149			
150			
151			
152			
153			
154			
155			
156			
157			
158			
159			
160			
161			
162			
163			
164			
165			
166			
167			
168			
169			
170			
171			
172			
173			
174			
175			
176			
177			
178			
179			
180			
181			
182			
183			
184			
185			
186			
187			
188			
189			
190			
191			
192			
193			
194			
195			
196			
197			
198			
199			
200			

Complete guide and load cell assembly

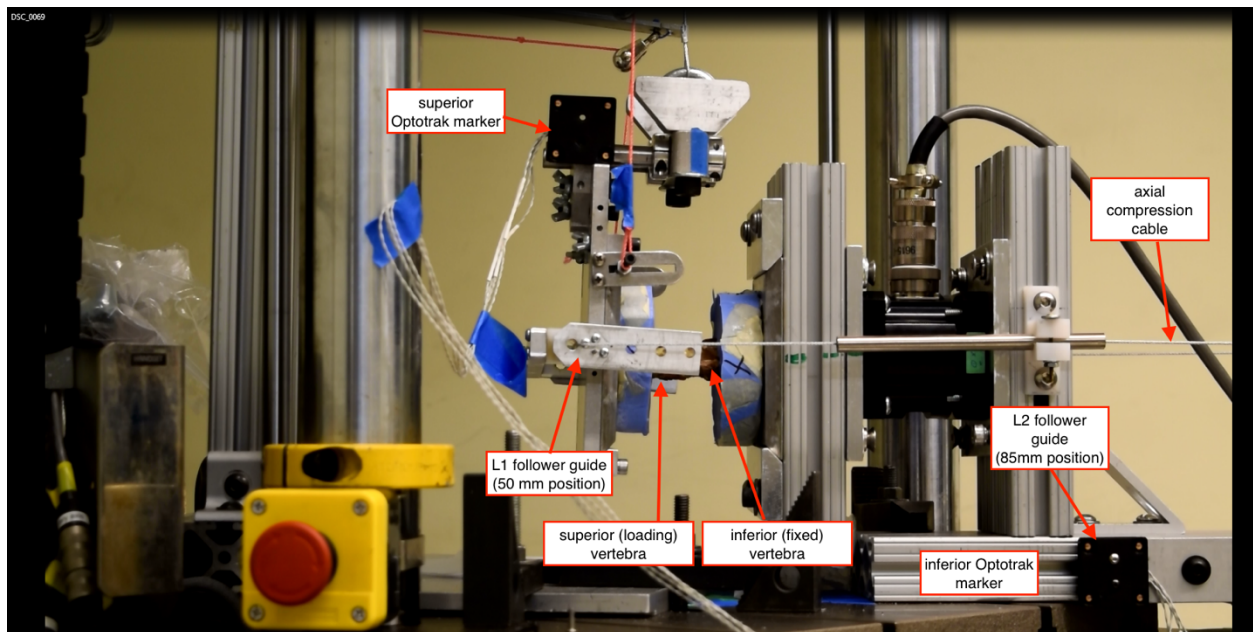
A3

SCALE: 1:1

## Appendix I: Photographs of Chapter 4 Experimental Set-up



**Shear test apparatus set-up for Chapter 4 (test without axial compression)**



**Video still of porcine test with application of axial compression using follower load method**